UNIVERSIDADE FEDERAL DE MINAS GERAIS

Instituto de Ciências Exatas

Programa de Pós-Graduação em Química

Yan Ferraz Ximenes Ladeira

ENHANCING BIOCATALYTIC PERFORMANCE OF THE ENZYME (*S*)-NORCOCLAURINE SYNTHASE

Adsorption Immobilization on Low-Cost Supports for Stereoselective Pictet-Spengler Reaction

Belo Horizonte

2025

UFMG/ICEX/DQ. 1.664
T. 758

Yan Ferraz Ximenes Ladeira

ENHANCING BIOCATALYTIC PERFORMANCE OF THE ENZYME (*S*)-NORCOCLAURINE SYNTHASE

Adsorption Immobilization on Low-Cost Supports for Stereoselective Pictet-Spengler Reaction

Tese apresentada ao Departamento de Química do Instituto de Ciências Exatas da Universidade Federal de Minas Gerais, como requisito parcial para a obtenção do grau de Doutor em Ciências - Química.

Orientador: Profº Adolfo Henrique de Moraes Silva

Belo Horizonte

2025

Ficha Catalográfica

L154e
2025
T

Ladeira, Yan Ferraz Ximenes.
Enhancing biocatalytic performance of the enzyme (S)-norcoclaurine synthase [manuscrito] : adsorption immobilization on low-cost supports for stereoselective Pictet-Spengler reaction transfer / Yan Ferraz Ximenes Ladeira. 2025.
142 f. : il., gráfs., tabs.

Orientador: Adolfo Henrique de Moraes Silva.

Tese (doutorado) – Universidade Federal de Minas Gerais – Departamento de Química.
Bibliografia: f. 91-99.
Apêndice: f. 100-142.

1. Química orgânica – Teses. 2. Catálise – Teses. 3. Proteínas – Síntese – Teses. 4. Compostos orgânicos – Teses. 5. Compostos heterocíclicos – Teses. 6. Biossíntese – Teses. 7. Enzimas imobilizadas – Teses. 8. Reação química – Condições e leis – Teses. 9. Monte Carlo, Método de – Teses. I. Silva, Adolfo Henrique de Moraes, Orientador. II. Título.

CDU 043

Elaborada por Márcia Cavalcanti Moreira – Bibliotecária – CRB6/3847.

UNIVERSIDADE FEDERAL DE MINAS GERAIS

UFMG
Programa de Pós-Graduação em Química
Departamento de Química - ICEx

química
pós-graduação-ufmg

"ENHANCING BIOCATALYTIC PERFORMANCE OF THE ENZYME (S)-NORCOCLAURINE SYNTHASE ((S)-NCS): ADSORPTION IMMOBILIZATION ON LOW-COST SUPPORTS FOR STEREOSELECTIVE PICTET-SPENGLER REACTION"

Yan Ferraz Ximenes Ladeira

Tese aprovada pela banca examinadora constituída pelos Professores:

Prof. Adolfo Henrique de Moraes Silva - Orientador
UFMG

Prof. Sebastião Antônio Mendanha Neto
UFG

Prof. Ivaldo Itabaiana Junior
UFRJ

Prof. Tiago Antônio da Silva Brandão
UFMG

Profa. Maria Helena de Araujo
UFMG

Belo Horizonte, 10 de julho de 2025.

Documento assinado eletronicamente por **Tiago Antonio da Silva Brandao**, **Professor do Magistério Superior**, em 10/07/2025, às 18:11, conforme horário oficial de Brasília, com fundamento no art. 5º do Decreto nº 10.543, de 13 de novembro de 2020.

Documento assinado eletronicamente por **Ivaldo Itabaiana Junior**, **Usuário Externo**, em 11/07/2025, às 09:19, conforme horário oficial de Brasília, com fundamento no art. 5º do Decreto nº 10.543, de 13 de novembro de 2020.

Documento assinado eletronicamente por **Maria Helena de Araujo**, **Professora do Magistério Superior**, em 11/07/2025, às 18:26, conforme horário oficial de Brasília, com fundamento no art. 5º do Decreto nº 10.543, de 13 de novembro de 2020.

Documento assinado eletronicamente por **Adolfo Henrique de Moraes Silva**, **Professor do Magistério Superior**, em 16/07/2025, às 16:22, conforme horário oficial de Brasília, com fundamento no art. 5º do Decreto nº 10.543, de 13 de novembro de 2020.

Documento assinado eletronicamente por **Sebastião Antônio Mendanha Neto**, **Usuário Externo**, em 22/07/2025, às 15:41, conforme horário oficial de Brasília, com fundamento no art. 5º do Decreto nº 10.543, de 13 de novembro de 2020.

A autenticidade deste documento pode ser conferida no site https://sei.ufmg.br/sei/controlador_externo.php?acao=documento_conferir&id_orgao_acesso_externo=0, informando o código verificador **4363983** e o código CRC **A49B163C**.

Referência: Processo nº 23072.242179/2025-99 SEI nº 4363983

AGRADECIMENTOS

Agradeço em primeiro lugar a Deus, O Criador de todas as coisas, que por sua infinita bondade me permitiu chegar até aqui. A Ele seja dada a honra e glória por meio de Jesus Cristo.

Também agradeço aos meus pais, Lilian e Geraldo Flávio, por toda a dedicação e apoio que me deram ao longo de toda minha vida. E a minha avó Osmira Mendes Barbosa (in memorian) que sempre se referia a mim, ainda quando criança, como Dr. Yan.

Agradeço a minha esposa, Rebeca, que além de ser a mulher da minha vida, me deu todo apoio nesses últimos anos.

Sou grato a todos os professores que me ajudaram a trilhar meus passos até aqui, em especial meu professor de Química do Ensino médio, David Abrão, aos meus professores do curso de graduação em Engenharia Química na PUC Minas, Guilherme Pereira, orientador de TCC, Lucilaine Valéria, orientadora de IC e Barbara Ricci, também orientadora de IC e que me indicou o programa de Pós-graduação em Química da UFMG, tornando-se assim uma peça-chave para a minha escolha.

Agradeço aos meus colegas de Laboratório: Diego Martins, Mozart Pereira, Philipe Fernandes, Ana Granja, Brunno Salvatti e Verônica Valadares, por toda a ajuda, em especial o Brunno e o Diego que ajudaram em muitas etapas desse projeto.

Sou grato a meu Orientador Dr. Adolfo Moraes por todo auxílio, dedicação e orientação na construção deste trabalho.

Agradeço os professores Dra. Amanda de Miranda, e Dr. Tiago Antônio da Silva Brandão que, juntamente com o Dr. Adolfo Moraes, coordenam o grupo de pesquisa MACROMOL.

Agradeço ao Laboratório de Ressonância Magnética de Alta Resolução – LAREMAR (UFMG), assim como ao Núcleo de Extensão do Departamento de Química da UFMG, pela infraestrutura utilizada para obtenção de todos os dados de RMN presentes nesse trabalho

Agradeço aos colaboradores e seus respectivos grupos de pesquisa: Prof. Dr. Rodrigo Verly e Dra. Carolina Ferreira do Laboratório de Síntese e Estrutura de Biomoléculas (LASEB)/UFVJM pelas análises de potencial zeta; Prof. Dra Maria Helena de Araújo e Dra. Ana Luiza Simões do Grupo de Tecnologias Ambientais - GruTAm/UFMG pelas análises de adsorção e dessorção de N_2; Prof. Dr. Sidney Jurado de Carvalho e Me. Ricardo Belarmino Junior da UNESP pelas simulações computacionais.

Agradeço ao Departamento de Química da UFMG, e seu respectivo Programa de Pós-graduação, e a própria UFMG, além dos órgãos de fomento: CAPES, CNPq, FINEP e FAPEMIG por fornecer toda infraestrutura e financiamento que possibilitaram a execução do presente trabalho, em especial a FAPEMIG que me forneceu a bolsa de doutorado.

Por fim, dedico este trabalho a Deus e a meus filhos Levy, Elisa e Efraim (in memoriam).

"As coisas encobertas pertencem ao Senhor, nosso Deus, mas as reveladas pertencem a nós e aos nossos filhos" (Dt 29:29).

RESUMO

A enzima (*S*)-norcoclaurina sintase ((*S*)-NCS) catalisa a reação de Pictet–Spengler de forma estereosseletiva entre dopamina e compostos carbonílicos, viabilizando a síntese sustentável de alcaloides tetraidroisoquinolínicos (THIQs) com relevância farmacêutica. No entanto, sua baixa estabilidade operacional e falta de reutilização limitam sua aplicação em escala industrial. Neste estudo, investigou-se a imobilização da (*S*)-NCS por adsorção em diferentes materiais, com ênfase nos suportes inorgânicos de baixo custo Caolin e Celite 545, como estratégia para aprimorar seu desempenho biocatalítico. A variante recombinante Δ19*Tf*NCS foi expressa heterologamente em *E. coli*, purificada e imobilizada via adsorção física. Inicialmente, diversos materiais foram triados para identificar os mais adequados à catálise da reação de Pictet–Spengler entre dopamina e hexanal. A imobilização de Δ19*Tf*NCS nos materiais selecionados (Caolin e Celite 545) foi aprofundada, resultando na definição de um protocolo definitivo de imobilização. Os biocatalisadores obtidos foram então avaliados quanto à atividade catalítica, estabilidade térmica, tolerância a co-solventes orgânicos e reutilização. Notavelmente, ambos os suportes melhoraram a estabilidade térmica e operacional da enzima, mas o Caolin apresentou desempenho superior. O material atingiu maiores rendimentos de imobilização, mantendo eficiência de adsorção acima de 85% mesmo em concentrações enzimáticas de até 7,5 mg/mL. Em contraste, o rendimento da Celite 545 caiu de $76 \pm 2\%$ para $60 \pm 3\%$ com o aumento da razão enzima/suporte. Essa capacidade de adsorção aprimorada é atribuída à maior área superficial específica do Caolin (11,063 m^2/g vs. 0,756 m^2/g) e ao potencial zeta mais negativo (−36,3 mV vs. −15,4 mV), que favorecem interações eletrostáticas mais fortes com a região N-terminal positivamente carregada da Δ19*Tf*NCS. Além disso, a enzima imobilizada em Caolin reteve maior atividade catalítica na presença de altas concentrações de DMSO, enquanto os catalisadores à base de Celite apresentaram perda significativa de atividade, destacando a maior capacidade do Caolin de proteger a enzima contra a desnaturação induzida por solventes.Simulações de Monte Carlo foram empregadas para fornecer informações em nível molecular sobre o processo de adsorção no Caolin, sugerindo orientações preferenciais da enzima e interações-chave entre aminoácidos e a superfície. As simulações indicaram o papel fundamental dos resíduos de histidina positivamente carregados na região N-terminal desestruturada da Δ19*Tf*NCS na forte afinidade eletrostática com a superfície do Caolin.

Palavras-chave: (*S*)-norcoclaurina sintase; biocatálise; imobilização enzimática; tetraidroisoquinolinas; reação de Pictet-Spengler.

ABSTRACT

The enzyme (*S*)-norcoclaurine synthase ((*S*)-NCS) catalyzes the stereoselective Pictet–Spengler reaction between dopamine and carbonyl compounds, enabling the sustainable synthesis of tetrahydroisoquinoline (THIQ) alkaloids with pharmaceutical relevance. However, its limited operational stability and lack of reusability hinder large-scale applications. In this study, the adsorption-based immobilization of (*S*)-NCS on different materials, with emphasis on the low-cost inorganic supports kaolin and Celite 545, was investigated as a strategy to enhance its biocatalytic performance. Recombinant (*S*)-NCS variant Δ19*Tf*NCS was heterologously expressed in *E. coli*, purified, and immobilized via physical adsorption. Initially, several materials were screened to identify the most suitable candidates for catalyzing the Pictet–Spengler reaction between dopamine and hexanal. Δ19*Tf*NCS immobilization in the selected materials, kaolin and celite 545, was investigated more deeply resulting in a definitive immobilization protocol. The resulting biocatalysts were then evaluated in terms of catalytic activity, thermal stability, tolerance to organic co-solvents, and reusability. Notably, while both supports improved the enzyme's thermal and operational stability, kaolin exhibited superior performance. It achieved higher immobilization yields, maintaining adsorption efficiency above 85% even at enzyme concentrations up to 7.5 mg/mL, compared to Celite 545, whose yield decreased from $76 \pm 2\%$ to $60 \pm 3\%$ with increasing enzyme-to-support ratios. This enhanced adsorption capacity is attributed to kaolin's larger specific surface area (11.063 m^2/g vs. 0.756 m^2/g) and more negative zeta potential (−36.3 mV vs. −15.4 mV), which promote stronger electrostatic interactions with the positively charged N-terminal region of Δ19*Tf*NCS. Furthermore, kaolin-immobilized enzyme retained higher catalytic activity under elevated DMSO concentrations, where Celite-based catalysts showed significant activity loss, highlighting kaolin's superior ability to protect the enzyme from solvent-induced denaturation.

Additionally, Monte Carlo simulations were employed to provide molecular-level insights into the adsorption process on kaolin, suggesting preferred enzyme orientations and key amino acid–surface interactions. These simulations suggested the important role of positively charged histidine residues within the unstructured N-terminal region of Δ19*Tf*NCS in mediating its strong electrostatic affinity for the kaolin surface.

Key Words: (*S*)-norcoclaurine synthase; biocatalysis; enzyme immobilization; tetrahydroisoquinolines; Pictet-Spengler reaction

LIST OF FIGURES

LIST OF ABBREVIATIONS

4-HPAA	4-hidroxyphenylacetaldehyde
(*S*)-NCS	(*S*)-norcoclaurine synthase
BIAs	Benzylisoquinoline alkaloids
CD	Circular dichroism
THIQ	Tetrahydroisoquinoline
BLAST	Basic Local Alignment Search Tool
THPB	Tetrahydroprotoberberine
DMSO	Dimetilsulfoxide
DFT	Density Functional Theory
QSAR	Quantitative Structure-Activity Relationship modeling
NMR	Nuclear Magnetic Resonance
HPLC	High Performance Liquid Chromatography
LC–MS	Liquid Chromatography Coupled to Mass Spectrometer
HEPES	4-(2-hydroxyethyl)-1-piperazineethanesulfonic acid
TAm	Transaminase
ic	isomeric content
dc	diastereoisomeric content
SDS-PAGE	Sodium Dodecyl Sulfate Polyacrylamide Gel Electrophoresis
IPTG	Isopropyl β-D-1-thiogalactopyranoside
OD600	Optical Density at 600 nm
LB	Luria Bertani
Ni-NTA	Nickel Nitrilotriacetic Acid
E. coli	*Escherichia coli*

Cα	Alpha carbon
RMSD	Root Mean Square Deviation
CLEAs	Cross-Linked Enzymes Aggregates
APTES	(3-Aminopropyl)-triethoxysilane
GDE	glycerol diglycidyl ether
DOE	Design of Experiments
RSM	Response Surface Methodology
zP or ζ-potential	Zeta potential (Potencial Zeta)
wt	Wild type
His-tag	Histidine tag
rpm	Rotations per minute
MWCO	Molecular Weight Cut-Off
KPi	Potassium Phosphate Buffer
RT	Room Temperature (Temperatura Ambiente)
BET	Brunauer-Emmett-Teller
BJH	Barrett-Joyner-Halenda
CG	Coarse-Grained
MD	Molecular Dynamics
PDB	Protein Data Bank

LIST OF TABLES

TABLE OF CONTENTS

1 INTRODUCTION AND LITERATURE REVIEW

1.1 Introduction - contextualization

Enzymes are highly selective biocatalysts that enable chemo-, regio-, and stereoselective reactions without requiring protection and deprotection steps, often simplifying synthetic routes compared to traditional methods (Britton; Majumdar; Weiss, 2018). They typically operate under mild conditions, such as aqueous media and physiological temperatures, and are renewable, biodegradable, and non-toxic, aligning with green chemistry and sustainable industrial practices (Rossino et al., 2022; Sheldon; Pereira, 2017). As such, enzymatic catalysis aligns closely with the principles of green chemistry and the goals of sustainable industrial practices (Fröhling; Hiete, 2020), and also with several United Nations Sustainable Development Goals (SDGs), particularly SDG 9 (Industry, Innovation and Infrastructure), SDG 12 (Responsible Consumption and Production) by fostering environmentally responsible and economically viable biotechnological solutions for industrial applications. However, their broader industrial use is limited by poor stability in non-natural environments, low tolerance to heat and solvents, and challenges related to storage, recovery, and reuse (Sheldon; Brady, 2018).

To overcome the limitations of natural enzymes in industrial applications, strategies like enzyme immobilization and protein engineering have become increasingly important. Protein engineering involves genetic modifications to enhance enzyme properties such as stability, activity, and substrate range. Two common approaches are: (1) rational design, which uses structural and mechanistic knowledge to make targeted changes—often via site-directed mutagenesis—and (2) directed evolution, which applies random mutagenesis followed by selection under specific conditions (Bernal; Rodríguez; Martínez, 2018; Liu; Xun; Feng, 2019). This groundbreaking approach was recognized with the 2018 Nobel Prize in Chemistry, awarded to Francis H. Arnold for her pioneering contributions to the field (“The Nobel Prize in Chemistry 2018”, *[S.d.]*).

Enzyme immobilization, on the other hand, transforms enzymes into heterogeneous biocatalysts by its association to a solid structure, facilitating their recovery in batch processes and enabling their implementation in continuous-flow systems. This approach can also enhance enzyme stability under harsh conditions - such as the presence of organic solvents or elevated temperatures - by mitigating denaturation and aggregation. While immobilization may lead to a reduction in catalytic activity, the resulting improvements in operational stability frequently

offset this drawback, rendering immobilized enzymes particularly advantageous for industrial applications (Júnior et al., 2021). In this context, the present work will focus exclusively on enzyme immobilization as the strategy of interest.

A particularly promising enzyme, (*S*)-norcoclaurine synthase ((*S*)-NCS), exhibits significant biocatalytic potential due to the importance of the reaction it catalyzes, an enantioselective Pictet–Spengler condensation between β-arylethylamines and carbonyl compounds (aldehydes and ketones), as well as the relevance of the resulting product class: tetrahydroisoquinolines (THIQs). Moreover, the enzyme displays broad substrate scope, adding to its versatility (Salvatti et al., 2024).

Several studies have reported different biocatalytic applications of this enzyme; however, to date, only two detailed investigations have explored the immobilization of (*S*)-NCS, demonstrating its feasibility in both purified and whole-cell formats for stereoselective BIA synthesis. While these studies employed diverse strategies and included continuous-flow systems, they did not address key parameters relevant to industrial application, such as thermal stability, solvent tolerance, or reusability (Arnold; Castiglione, 2023; Lechner et al., 2018).

In this context, the present thesis contributes to the field by proposing a low-cost and scalable immobilization strategy based on physical adsorption onto kaolin and Celite 545. The resulting immobilized biocatalysts were comprehensively evaluated in terms of thermal stability, DMSO tolerance, and operational reusability. Additionally, this is the first study to apply Monte Carlo simulations to investigate the interactions between Δ19*Tf*NCS and kaolin, revealing possible enzyme orientations and binding residues, thus supporting the rational design of immobilization systems. These findings enhance the robustness and practical applicability of (*S*)-NCS in biocatalysis and the biomanufacturing of BIA-related compounds.

1.2 (*S*)-Norcoclaurine synthase

The enzyme (*S*)-norcoclaurine synthase ((*S*)-NCS) (EC 4.2.1.78), commonly found in plant species such as *Thalictrum flavum*, *Coptis japonica*, and *Papaver somniferum*, catalyzes the Pictet–Spengler reaction between dopamine and carbonyl compounds (ketones and aldehydes), leading to the formation of tetrahydroisoquinolines (Salvatti et al., 2024) (Figure 1a). In nature, this reaction specifically occurs between dopamine and 4-hydroxyphenylacetaldehyde (4-HPAA) – both tyrosine derivatives - resulting in the formation of (*S*)-norcoclaurine (Figure 1a). This transformation constitutes the first committed step in the biosynthetic pathway of

benzylisoquinoline alkaloids (BIAs), a class of natural compounds that includes pharmaceutically relevant molecules such as codeine, morphine, berberine, and papaverine (Figure 1b) (Berkner et al., 2007; Samanani; Liscombe; Facchini, 2004).

The described features position this enzyme as a Pictet–Spenglerase of notable importance. As a result, (*S*)-NCS has become the focus of a growing number of studies, driven not only by its biological relevance but also by its potential application in non-natural substrates reactions, leading to the stereoselective formation of a wide range of tetrahydroisoquinoline derivatives (Salvatti et al., 2024). On the other hand, the still relatively limited number of studies, especially when compared to extensively studied enzymes such as lipases.

It is also important to highlight that the industrial production of key benzylisoquinoline alkaloids (BIAs) continues to rely on the cultivation of poppy plants. However, this agricultural dependence makes the supply chain vulnerable to disruptions caused by pests, plant diseases, and extreme weather conditions, which can compromise the consistent availability of these medically essential compounds (Arnold; Castiglione, 2023). This reinforces the need to develop alternative ways of producing this class of compounds, highlighting the relevance of the studies presented below.

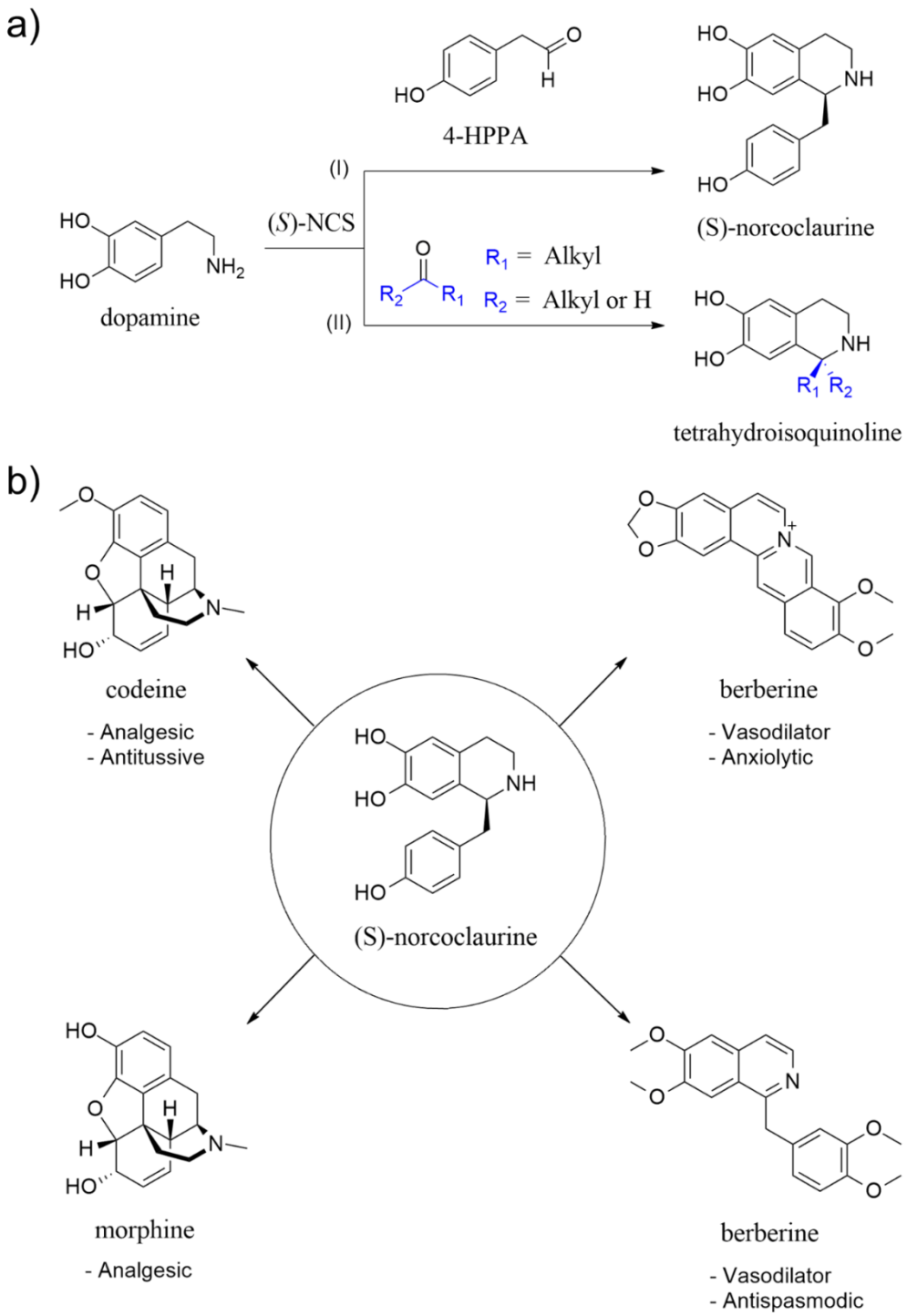

Figure 1. Reaction catalyzed by (S)-NCS and benzylisoquinoline alkaloids derived from (S)-norcoclaurine. **a)** General reaction scheme illustrating the transformations catalyzed by (S)-NCS; **b)** Natural derivatives of (S)-norcoclaurine and their applications.

1.2.1 Discovery and Early Studies

(*S*)-NCS was first identified in 1981 in a study investigating the initial step of benzylisoquinoline alkaloid biosynthesis. The enzyme, found in certain alkaloid-producing

plants, catalyzed the reaction between 3,4-dihydroxyphenylacetaldehyde and dopamine to form (*S*)-norlaudanosoline (Figure 2), whose stereochemistry was confirmed by CD spectroscopy (Rueffer et al., 1981). This contradicted a prior hypothesis that norlaudanosoline-1-carboxylic acid was the key intermediate (Wilson; Coscia, 1975), a view later abandoned due to lack of enzymatic activity with 3,4-dihydroxyphenylpyruvate.

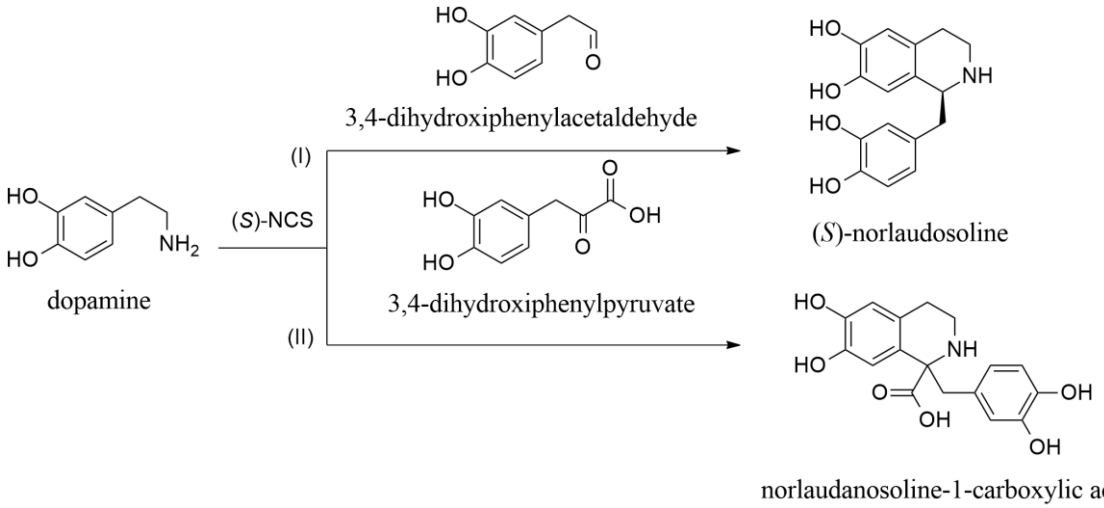

Figure 2. Scheme of reactions studied by (Rueffer et al., 1981). The enzyme name is already corrected to (*S*)-NCS although it is not done in the original study.

Although the initially proposed role of (*S*)-norlaudanosoline as the biosynthetic precursor was incorrect, the true intermediate being (*S*)-norcoclaurine, the 1981 study provided a crucial foundation for later research on (*S*)-NCS. Subsequent studies using radiolabeled precursors confirmed (*S*)-norcoclaurine as the authentic biosynthetic intermediate, leading to a redefinition of the enzyme's role and its renaming as (*S*)-NCS (Stadler et al., 1987; Stadler; Kutchan; Zenk, 1989; Stadler; Zenk, 1990). In 2001, (*S*)-NCS was isolated and partially characterized from *Papaver somniferum* cell cultures, where it catalyzed the stereoselective condensation of dopamine and 4-hydroxyphenylacetaldehyde under near-physiological conditions (Samanani; Facchini, 2001). It was also purified from *Thalictrum flavum*, showing a molecular mass of approximately 28 kDa (Samanani; Facchini, 2002). In 2004, the same group cloned the *Tf*NCS gene and expressed active truncated variants in *E. coli*, confirming their catalytic function (Samanani; Liscombe; Facchini, 2004). These studies represent the first successful isolation, cloning, and expression of (*S*)-NCS, paving the way for future structural, functional, and biotechnological advancements.

1.2.2 Relationship between (S)-NCS and PR-10/Bet v 1 Family Proteins

The isolation and sequence analysis of the gene encoding *Thalictrum flavum* (*S*)-norcoclaurine synthase (*Tf*NCS) enabled insightful bioinformatic comparisons with other plant proteins. Using the BLAST algorithm, Samanani et. al (2004) demonstrated that *Tf*NCS (Figure 3a) shares 28–38% identity and up to 60% similarity with members of the PR-10 and Bet v 1 (Figure 4b) protein families, groups well known for their roles in plant defense responses and allergenicity. This structural relationship suggests that (*S*)-NCS evolved from these ancestral protein families, acquiring a novel catalytic function while retaining key features of their three-dimensional fold. Interestingly, no significant homology was observed between *Tf*NCS and strictosidine synthase (STR) (Figure 3c), another Pictet–Spenglerase involved in the biosynthesis of monoterpenoid indole alkaloids. The lack of structural or functional similarity between (*S*)-NCS and STR, despite catalyzing analogous reactions, highlights the evolutionary plasticity of Pictet–Spengler chemistry and underscores the uniqueness of (*S*)-NCS as the entry-point enzyme in the biosynthesis of benzylisoquinoline alkaloids(Fernandes et al., 2013; Lichman, 2016; Samanani; Liscombe; Facchini, 2004).

The structural resemblance between *Tf*NCS and proteins from the PR-10/Bet v1 superfamily raises the need to understand these proteins a bit deeper. The Bet v 1 superfamily comprises a wide array of plant proteins that, despite their functional divergence, share a conserved three-dimensional fold. This canonical fold was first elucidated for the birch pollen allergen Bet v 1 through both X-ray crystallography and NMR spectroscopy (Gajhede et al., 1996; Schweimer et al., 1999). PR-10 (pathogenesis-related class 10) family, which includes Bet v 1 itself and a variety of other proteins involved in plant defense, is one of the major groups within the Bet v 1-like superfamily that includes the (*S*)-NCS. Members of the PR-10 family are typically upregulated in response to biotic and abiotic stress (Fernandes et al., 2013).

The protein Bet v 1 was identified as the major pollen allergen from birch (*Betula verrucosa*), being responsible for triggering allergic responses in sensitized individuals. Structurally, Bet v 1 adopts a distinctive fold composed of a seven-stranded antiparallel β-sheet enveloping a long C-terminal α-helix, forming a large, solvent-accessible hydrophobic cavity (Figure 3b). Remarkably, this fold is not restricted to plants but has been identified across all three domains of life. Such widespread phylogenetic distribution strongly suggests that the Bet v 1 fold emerged early in evolution and probably existed in the last universal common ancestor. Over evolutionary time, this primordial structural scaffold gave rise to a wide array of proteins with

varied functions while retaining the core features of the Bet v 1 architecture (Radauer; Lackner; Breiteneder, 2008).

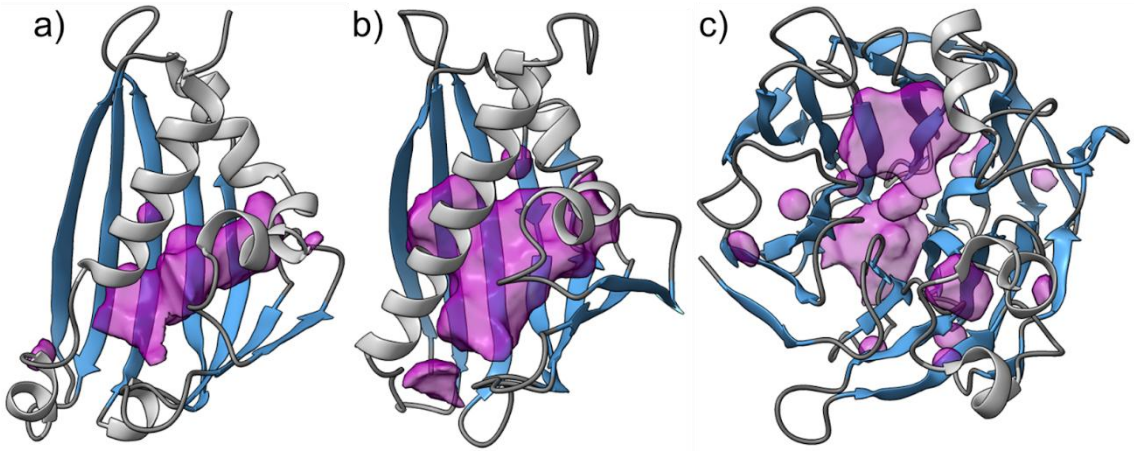

Figure 3. Crystallographic structure of the (*S*)-NCS, Bet v 1 and STR proteins. **a)** Δ19*Tf*NCS (PDB: 2VNE-B) **b)** Bet v 1(PDB: 1BV1) **c)** STR (PDB: 4IMB-B). The figures were created using ChimeraX 1.10 software.

1.2.3 Natural occurring (S)-NCS variants

In 2018, Lechner et al. expanded the known diversity of natural (S)-NCS enzymes by identifying eight homologous sequences through BLAST searches using the TfNCS gene, including three novel variants and the previously characterized CjNCS1 (Minami et al., 2007), all of which catalyze the Pictet–Spengler reaction with dopamine and 4-HPAA. These enzymes formed a comparative library (Table 1) to support structure–function studies (Lechner et al., 2018).

Table 1. Library of natural variants of (*S*)-NCS discovered by Lechner et. al. (2018).

Abbreviation	Origin organism	Sequence similarity (%)	Sequence identity (%)	Molecular mass (kDa)	Residues number
*Tf*NCS	*Thalictrum flavum*	100	100	22.2	200
*Am*NCS1	*Argemone mexicana*	67	51	21.5	193
*Am*NCS2	*Argemone mexicana*	64	50	22.4	197
*Cs*NCS	*Corydalis saxicola*	70	55	20.0	180
*Pb*NCS	*Papaver bracteatum*	71	55	19.5	172
*Ps*NCS1	*Papaver somniferum*	67	51	26.8	237

*Ps*NCS2	*Papaver somniferum*	69	51	23.7	208
*Cj*NCS1	*Coptis japonica*	-	-	40.0	352
*Cj*NCS2	*Coptis japonica*	77	64	20.3	179

In 2023, Zhang et al. discovered five novel NCSs (*Nn*NCS1–*Nn*NCS5) in *Nelumbo nucifera*, a species not previously associated with this activity. These enzymes, expressed and characterized in *E. coli*, catalyzed the condensation of dopamine with carbonyl substrates but, unlike all previously known NCSs, produced racemic mixtures of norcoclaurine. *Nn*NCS1, structurally resolved by X-ray crystallography, revealed a PR-10 fold with a modified active site, suggesting a structural basis for the lack of enantiopreference (Zhang et al., 2023). More recently, Li et al. (2024) identified sixteen putative NCS genes in *Stephania tetrandra*, selecting five (*St*NCS1–*St*NCS5) for structure prediction and functional validation. Only *St*NCS2 and *St*NCS4 displayed (*S*)-NCS activity both in *E. coli* and in engineered yeast strains, confirming their functional roles. These new variants further expand the biochemical and evolutionary diversity of the (*S*)-NCS family (Li et al., 2024).

1.2.4 (S)-NCS structure and reaction mechanism.

A significant advance in understanding the structure of (*S*)-NCS occurred in 2009 with the resolution of the first crystal structures of the truncated variant Δ19*Tf*NCS, in both apo (PDB: 2VNE) and holo (PDB: 2VQ5) forms (Ilari et al., 2009). The holo form revealed key active site residues, Tyr108, Glu110, Lys122, and Asp141, implicated in catalysis. In this structure, the aldehyde was located deep within the active site, with its carbonyl near Lys122, while dopamine was closer to the catalytic pocket entrance (Ilari et al., 2009). These findings supported the previously proposed "HPAA-first" mechanism, in which the aldehyde 4-hydroxiphenylacetaldehyde (4-HPAA) binds before dopamine, as inferred from kinetic and inhibition data (Luk et al., 2007; Samanani; Facchini, 2002). This model gained attraction and was reinforced by crystallographic and molecular modeling studies (Bonamore et al., 2010), but it was later questioned for failing to account for (*S*)-NCS's high selectivity for dopamine despite its broad aldehyde substrate scope, resulting in the formulation of the hypothesis that in fact, the Pictet-Spengler reaction would only be catalyzed by the enzyme if dopamine first bound to the active site (Lichman et al., 2015b).

To confirm this hypothesis molecular docking studies, kinetic assays, and site-directed mutagenesis were conducted, resulting in the proposal of an alternative model, termed the "dopamine-first" mechanism. According to this model, the reaction proceeds when dopamine binds first to the catalytic site, interacting directly with Lys122, while the aldehyde enters subsequently and is positioned at the entrance of the active site, partially solvent-exposed. This spatial arrangement not only accounts for the enzyme's specificity for dopamine but also explains its tolerance to structurally diverse aldehydes (Lichman et al., 2015b).

Definitive structural evidence for the "dopamine-first" mechanism was later provided by Lichman et al. (2017), who crystallized a Δ29*Tf*NCS variant in complex with a synthetic ligand mimicking the transition state of the reaction. The resulting structure (PDB: 5NON) confirmed the direct interaction of the catechol moiety of dopamine with Lys122 (Figure 4) and revealed the aldehyde positioned at the entrance of the active site (Lichman et al., 2017b). This spatial configuration provides a compelling mechanistic basis for the enzyme's selectivity, while also accounting for its substrate promiscuity.

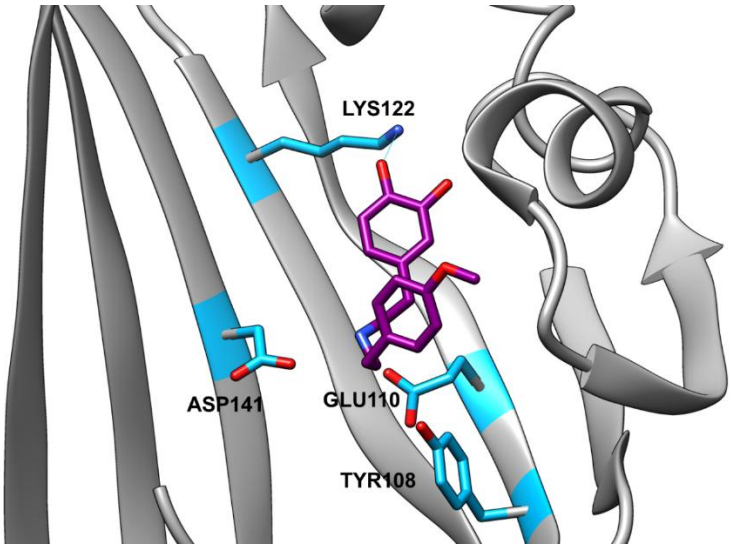

Figure 4. Crystallographic structure of *Tf*NCS focusing on the active site (PDB: 5NON). This structure, reported by Lichman et al. (2017), allows the identification of the four key active site residues - Tyr108, Glu110, Lys122, and Asp141 - with particular emphasis on the interaction between the hydroxyl group of the catechol ring in the transition state analogue and the amino group of residue Lys122. The C-terminal α-helix is hidden on this figure for better active site visualization.

Recent studies have reinforced the "dopamine-first" mechanism for (S)-NCS. Sheng and Himo (2019) used DFT calculations based on the TfNCS crystal structure (PDB: 5NON) and showed that, although both dopamine-first and HPAA-first binding modes are structurally possible, the HPAA-first pathway has higher activation barriers and is thus kinetically unfavorable. They

also found that the final deprotonation/rearomatization step determines enantioselectivity, with a 2.3 kcal/mol lower barrier favoring the (*S*)-product (Sheng; Himo, 2019).

More recently, Salvatti et al. (2024) investigated how (S)-NCS accommodates different aldehydes and ketones using enzymatic assays (via NMR) and computational tools like QSAR, DFT (Fukui functions), and molecular dynamics. Their findings showed that formation of the iminium intermediate is highly dependent on substrate electrophilicity and steric fit, supporting the dopamine-first model as both a mechanistic explanation and a predictive tool for evaluating substrate compatibility in biocatalysis (Salvatti et al., 2024).

1.2.5 Biocatalytic Potential of (S)-NCS: Substrate Diversity

(*S*)-NCS exhibits remarkable substrate promiscuity, making it highly versatile for biocatalysis. Its potential was first noted in 1981 when it catalyzed the condensation of dopamine with 3,4-dihydroxyphenylacetaldehyde to produce (*S*)-norlaudanosoline (Rueffer et al., 1981). Later, studies expanded its known substrate scope. Minami et al. (2007) tested *Cj*NCS1 with various aldehydes, carboxylic acids, and pyruvic acid, observing activity only with specific aldehydes and dopamine (Minami et al., 2007).

In 2012, Pesnot et al. evaluated CjNCS2 against 11 amines and 28 carbonyl compounds (Table A1 and A2 – Appendix), reporting high yields (up to 99%) and excellent enantioselectivity (>95% ee) with several aldehydes but limited amine acceptance. Docking studies identified key residues involved in aldehyde binding (Glu110, Asp141, Lys122) (Pesnot et al., 2012). That same year, Ruff, Bräse, and O'Connor tested TfNCS with 19 non-natural aldehydes and several amines (Table A3 and Figure A1 – Appendix), finding broad aldehyde tolerance but specificity for dopamine and meta-hydroxylated analogs (Ruff; Bräse; O'Connor, 2012). In 2014, Nishihachijo et al. tested a truncated CjNCS2 variant (Δ29CjNCS2) with 11 aldehydes, including previously untested compounds, confirming conversions up to 99% with substrates like 3-phenylpropanal, and further expanding the substrate scope of (*S*)-NCS (Table A4 - Appendix) (Nishihachijo et al., 2014).

Following this publication, a significant number of studies have broadened the substrate diversity associated with (*S*)-NCS applications. Among these, some stand out for reporting the enzymatic formation of tetrahydroisoquinoline scaffolds not previously accessible using (*S*)-NCS, including 1,1′-disubstituted THIQs, spiro-THIQs, and aryl-THIQs (Figure 5). These studies will be presented in the following sections.

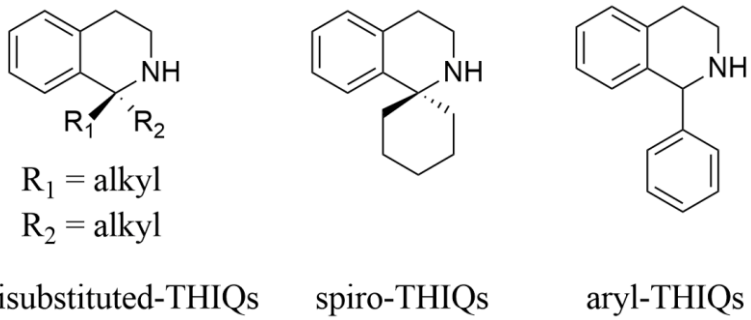

Figure 5. Tetrahydroisoquinoline scaffolds accessible through (*S*)-NCS-catalyzed reactions.

The study by Lichman et al. (2015) significantly advanced the rational understanding of the enzymatic promiscuity of (S)-NCS. Using site-directed mutagenesis, the authors investigated aspects of the "dopamine-first" mechanism and the enzyme's substrate acceptance profile. Particular emphasis was placed on the L76A mutation, which replaces leucine with alanine (a smaller side chain) at position 76, located within a loop at the entrance of the active site (Lichman et al., 2015b).

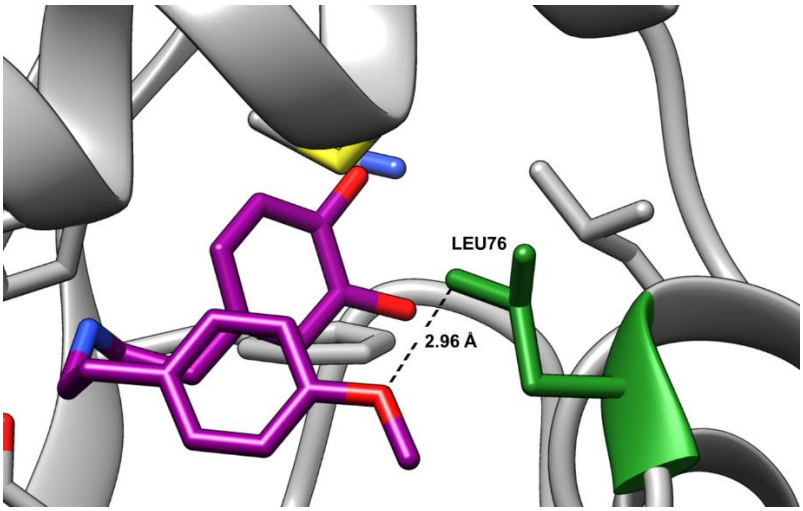

Figure 6. *Tf*NCS (PDB 5NON) active site entrance focusing on leucine 76. It is shown the distance between a carbon atom of Leu76 and an oxygen atom of the aldehyde portion of the iminium intermediary mimetic (Lichman et al., 2015b).

Structural analysis (Figure 6) revealed that this region directly influences the accommodation of carbonyl-containing compounds. The L76A variant showed a catalytic efficiency (kcat/Km) twice that of the wild-type enzyme when reacting with the bulky substrate (S)-citronellal, which had not been previously tested. Thus, this work represents a key advance in the rational engineering of (S)-NCS variants with expanded substrate scope and enhanced catalytic activity (Lichman et al., 2015b).

The same author published, two years later, reported a study demonstrating, for the first time, that (*S*)-NCS can catalyze reactions with ketones—previously thought unfeasible. The study led to the synthesis of novel 1,1′-disubstituted and spiro-tetrahydroisoquinolines (THIQs) (Figure 7) using ketones like 4-hydroxyphenylacetone, phenylacetone, and various substituted cyclohexanones. Mutagenesis at residue A79 proved critical: the A79I variant showed high efficiency with aliphatic ketones (up to >90% conversion, 95% ee), while A79F excelled with bulky cyclic ketones (up to ~100% conversion). These highlight the significance of the loop between residues 76 and 80 (located at the entrance of the active site) in influencing the substrate profile of (*S*)-NCS, as previously demonstrated by Lichman et al. (2015), and suggest that bulkier residues promote better accommodation and productive orientation of large substrates.(Lichman et al., 2017a).

Roddan et al. (2019) expanded the substrate scope of (S)-NCS by showing that engineered variants (Δ29*Tf*NCS mutants A79I, L76V, and M97V) can efficiently convert α-methyl-substituted aldehydes—previously considered poorly tolerated—into (1S,1′R)-configured products when reacted with dopamine and other amines (Figure A2 – Appendix). Dopamine showed the highest reactivity, and high conversion and stereoselectivity were achieved with most substrates. M97V, A79I, and L76V variants outperformed Δ29TfNCS in activity and selectivity for several products. Structural analysis of Δ33TfNCS revealed that the M97V mutation enlarges the active site to better fit bulkier aldehydes, improving selectivity but reducing stereoselectivity with smaller aldehydes (Roddan et al., 2019). The L76V mutation alters the active site entrance, favoring (R)-enantiomer binding and increasing diastereoselectivity. The effects of A79I had previously been described by Lichman et al. (2017a), highlighting its role in enhancing reactivity with specific substrates.

Roddan et al. (2020) expanded the substrate scope of (S)-NCS by synthesizing (1S)-aryl-THIQs from dopamine and various benzaldehydes using wild-type and mutant enzymes (M97V, M97F, L76V). The M97V variant achieved >99% conversion and enantiomeric excess. Optimized conditions enabled full conversion even for substrates previously unreactive (Figure A3 – Appendix) (Ruff; Bräse; O'Connor, 2012). Structural analysis (PDB: 6Z82) confirmed a "dopamine-first" mechanism and showed that M97V reduces steric hindrance, improving substrate alignment (Roddan et al., 2020)

Zhao et al. (2021) further broadened (S)-NCS's substrate scope by synthesizing over 20 complex THIAs—including 1,1′-disubstituted, spiro-, and bis-THIAs—from diverse ketones.

Using wild-type and variants (A79F, A79I, F80L, M97F, Y108F), they achieved up to 79% conversion and 86% ee. F80L selectively favored di-substitution in 1,4-cyclohexanedione reactions. Docking studies linked selectivity to catechol orientation near Lys122. These findings underscore the enzyme's catalytic promiscuity and potential for accessing structurally diverse THIAs (Zhao et al., 2021).

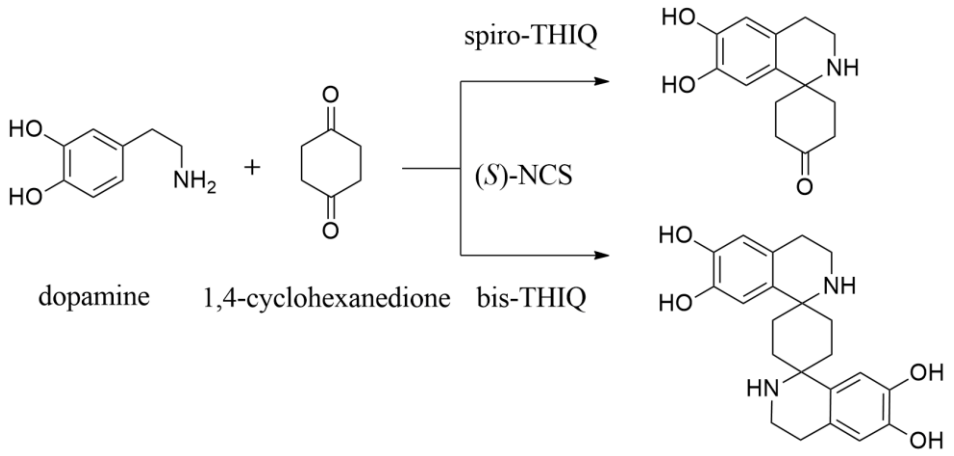

Figure 7. Formation of both mono- and di-Pictet–Spengler products with 1,4-cyclohexanedione.

1.2.6 Biocatalytic Potential of (S)-NCS: Application Strategies

Beyond its broad substrate scope, (*S*)-NCS has demonstrated significant application potential through various strategies, including enzymatic and chemoenzymatic routes, cascade reactions, use in living cells via microbial metabolic engineering, and, finally, enzyme immobilization.

1.2.6.1 Enzymatic and chemo-enzymatic reaction processes

In 2014, Maresh et al. developed a one-pot method to synthesize THIQs from amino acids by combining oxidative decarboxylation of L-tyrosine (using NaOCl) to form 4-HPAA with chemical or enzymatic Pictet–Spengler condensation. The enzymatic route, using TfNCS in maleate buffer, yielded (S)-THIQs with high stereoselectivity under mild conditions (Figure 8) (Maresh et al., 2014).

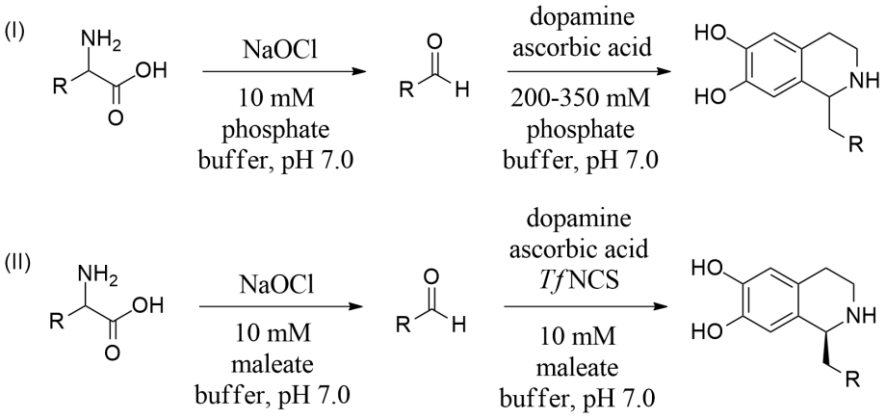

Figure 8. Reactional Scheme proposed by Maresh et. al. (2014). (I) – chemical strategy and (II) – chemo-enzymatic strategy.

Another elegant example of applying (*S*)-NCS in synthetic cascades was reported by Lichman et al. (2015a), which designed a one-pot, three-step chemoenzymatic cascade integrating a transaminase (CV2025) and Δ29*Tf*NCS to convert dopamine into (S)-norlaudanosoline and further into THPB alkaloids. The process reached 64% overall conversion and >95% ee, demonstrating the synthetic potential of combining enzymatic and chemical steps.(Lichman et al., 2015a).

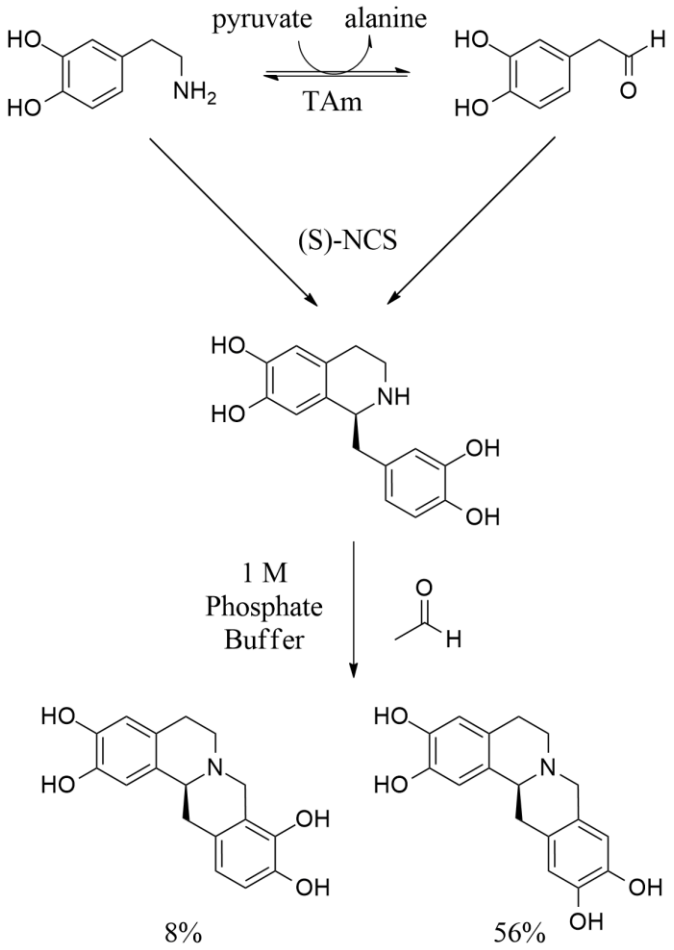

Figure 9. One-pot triangular chemoenzymatic cascades proposed by Lichman et. al. (2015).

Erdmann et al. (2017) synthesized trisubstituted THIQs with three chiral centers from low-cost precursors via enzymatic and chemoenzymatic routes. Using *Ec*AHAS-I, Cv2025, and Δ29*Tf*NCS-A79I, the enzymatic pathway yielded the (*1S,3S,4R*) isomer with 88% conversion and 97% isomeric purity, while the chemical pathway gave stereoisomers with opposite C1 configuration due to substrate control (Erdmann et al., 2017).

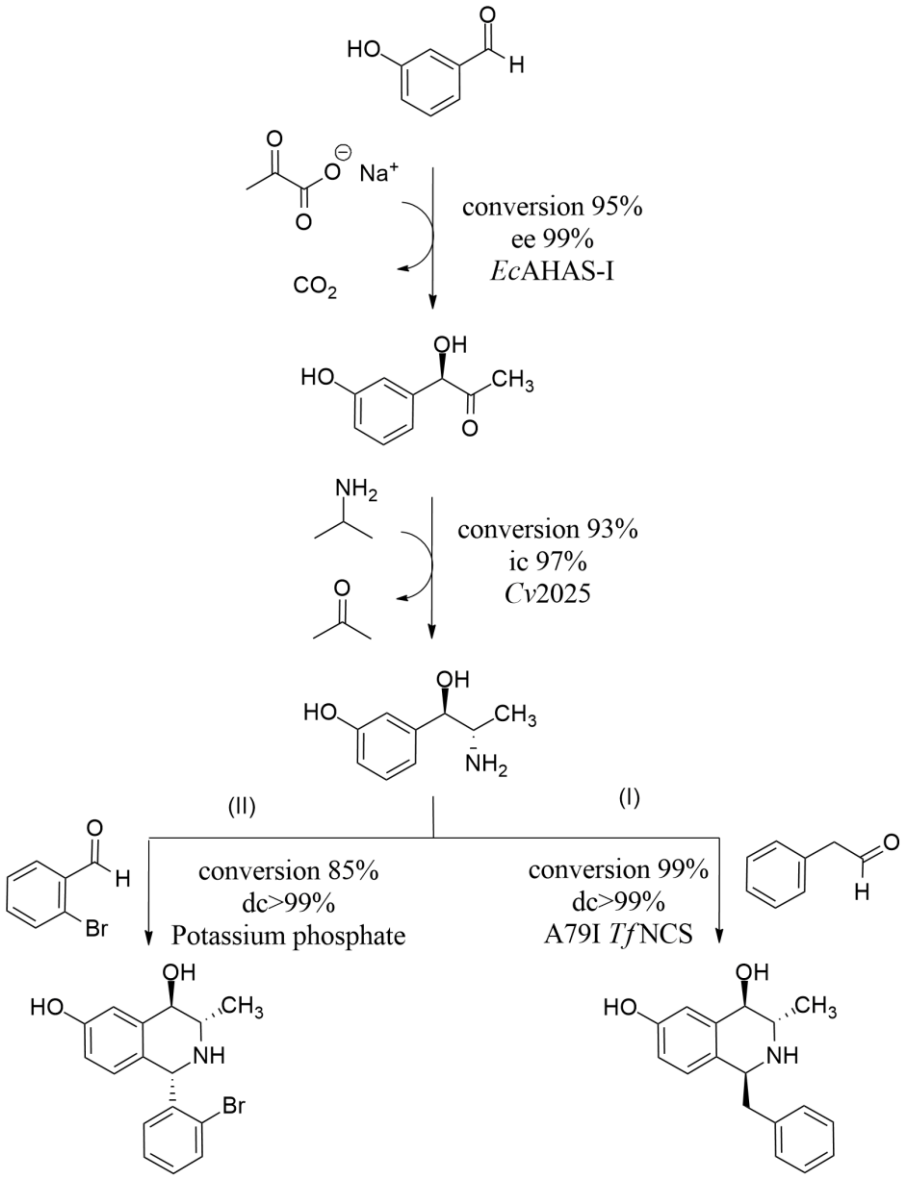

Figure 10. Enzymatic and chemoenzymatic routes proposed by Erdmann et al. (2017).

Finally, Zhao et al. (2018) developed a one-pot strategy for trolline synthesis by coupling asymmetric Pictet–Spengler reactions (via Δ29*Tf*NCS or variants) with intramolecular cyclization. Using A79F and optimized substrates, the method achieved up to 96% conversion and >99% ee, and extended to novel NCS substrates such as fluorinated dopamine analogs. (Zhao et al., 2018).

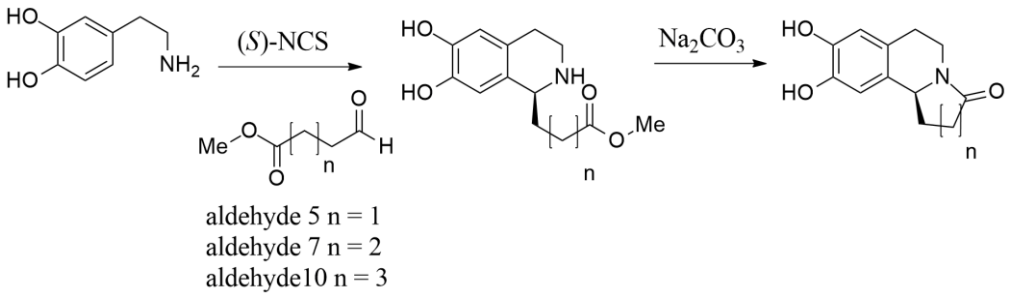

Figure 11. One-pot strategy proposed by Zhao et al. (2018).

In summary, these studies highlight not only the remarkable versatility of (*S*)-NCS in accepting non-natural substrates and generating products with high stereoselectivity but also reinforce the effectiveness of one-pot chemoenzymatic strategies for the synthesis of complex bioactive alkaloids without the need for intermediate purification. This represents a significant advancement from both a synthetic and a sustainability-oriented perspective in the field of biocatalysis.

1.2.6.2 Metabolic engineering strategies

(*S*)-NCS has become a key enzyme in metabolic engineering strategies for producing benzylisoquinoline alkaloids (BIAs) in yeast. In a pioneering study, Trenchard et al. (2015) introduced (*S*)-NCS into *Saccharomyces cerevisiae* as part of the first de novo biosynthetic platform to produce (*S*)-reticuline from central metabolites, enabling the enzymatic condensation of dopamine and 4-HPAA into norcoclaurine, an essential intermediate (Figure 12) (Trenchard et al., 2015).

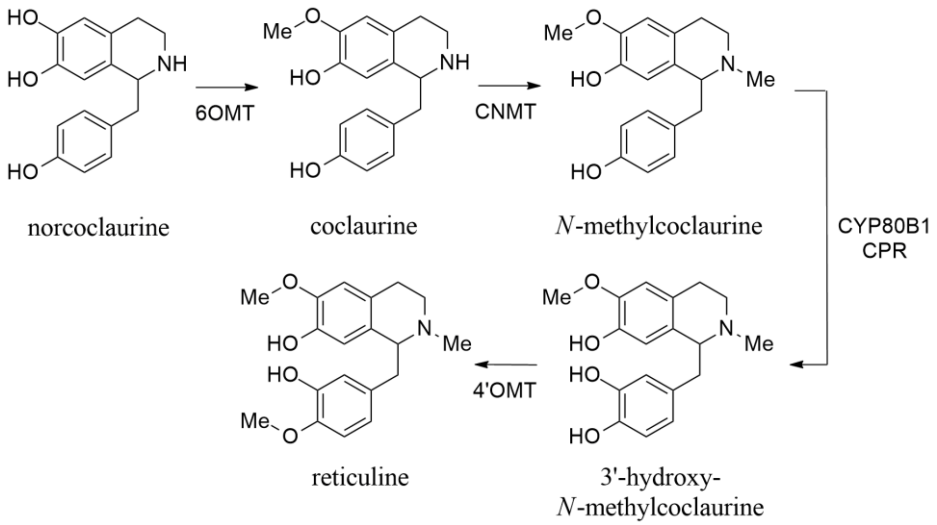

Figure 12. Metabolic pathway of BIAs up to reticuline proposed by Trenchard et. al. (2015). The enzymes involved are: 6OMT - 6-O-methyltransferase; CNMT - coclaurine-N-

methyltransferase; CYP80B1 - *N*-methylcoclaurine 3'-hydroxylase; CPR - cytochrome P450 NADPH-reductase; 4'OMT - 3'hydroxy-*N*-methylcoclaurine 4'-O-methyltransferase.

This strategy was later consolidated in patent US 2016/0319314 A1, which outlines microbial production methods for BIAs and their derivatives using engineered yeast, positioning (*S*)-NCS as a core component for synthesizing both natural and non-natural compounds. In a subsequent study, Galanie et al. (2015) incorporated (*S*)-NCS into a more complex system achieving complete biosynthesis of opioids from glucose, with (S)-NCS central to producing (*S*)-reticuline and feeding the morphinan pathway (Galanie et al., 2015). More recently, Pyne et al. (2020) employed engineered variants like *Cj*NCSΔN35 in a high-yield (S)-reticuline platform (up to 4.6 g/L) and used (*S*)-NCS to generate non-natural THIQs from exogenous amino acids (Pyne et al., 2020). Collectively, these efforts confirm (*S*)-NCS as a strategic and versatile enzyme for constructing modular yeast platforms capable of producing both natural and novel BIAs at scale.

1.2.6.3 (S)-NCS immobilization studies

Immobilization studies involving (*S*)-NCS are limited to only two published articles, which will be discussed in greater detail in this section. Beginning with the first publication, Lechner et al. (2018), previously mentioned in Section 2.3 of this chapter, investigated a series of naturally occurring (*S*)-NCS variants (Table 1). After constructing a library of nine natural variants of (*S*)-NCS, they were expressed in *Escherichia coli* BL21(DE3) and assessed the activity of each variant using lyophilized whole cells (Lechner et al., 2018).

In the initial phase of this study, various non-immobilized (*S*)-NCS variants was screened to identify the most promising candidate based on conversion and enantioselectivity, using whole-cell biocatalysts under standardized reaction conditions. Most variants, including *Am*NCS2, *Cj*NCS2, *Pb*NCS, *Ps*NCS2, and *Tf*NCS, achieved high conversions (>90%) and excellent enantiomeric excesses (>98%), while *Cj*NCS1 showed significantly lower performance. Control reactions with only buffer or E. coli cells revealed a non-stereoselective background reaction, highlighting the superior catalytic efficiency of the NCS variants. Following this screening, the authors optimized the expression of selected enzymes and tested their activity at higher substrate concentrations. *Pb*NCS, expressed in whole cells and used at 1 $mg \cdot mL^{-1}$, showed the best performance (60% conversion and >98% ee in 30 minutes) and was selected for subsequent immobilization experiments (Lechner et al., 2018).

Table 2. Conversions and enantiomeric excesses of recombinant NCS variants from the first screening realized by Lechner et. al. (2018).

Sample	Conversion (%)	e.e (%)
*Am*NCS1	90	>98
*Am*NCS2	>99	>98
*Cs*NCS	90	>98
*Cj*NCS1	35	41
*Cj*NCS2	>99	>98
*Pb*NCS	>99	>98
*Ps*NCS1	85	93
*Ps*NCS2	>99	>98
TfNCS	>99	>98
Whole cells	57	racemic
Buffer	3	no detection

Subsequently, the expression in *E. coli* cells was optimized for selected (*S*)-NCS variants using chaperones from Takara Chaperone Kit, and autoinduction media (4ZY-LAC). They then evaluated the performance of lyophilized cell and lysate samples in reaction media containing higher substrate concentrations (50 mM dopamine and 62 mM aldehyde), aiming to scale up the reaction. Among the tested samples, *Pb*NCS (1 mg mL^{-1}, expressed in whole cells) achieved the highest conversion (60%) and enantiomeric excess (e.e. >98%) within 30 minutes of reaction time and was therefore selected for immobilization experiments (Lechner et al., 2018).

In the immobilization phase of their study, Lechner et al. (2018) tested both whole-cell and purified enzyme approaches for immobilizing PbNCS. Whole-cell immobilization was performed via alginate encapsulation or by adding solid supports (Amberlite, Diaion HP-2MG, YTONG) to the culture medium to promote biofilm formation. For purified PbNCS, which contained a His-tag, affinity-based immobilization was carried out using Ni^{2+} (ABT HIGH Density NICKEL) and Fe^{2+}-based supports (EziG1–3). The immobilized biocatalysts were evaluated in the Pictet–Spengler reaction between dopamine and 4-HPAA (50 mM each). Among all tested systems, the EziG3-immobilized PbNCS (on semi-hydrophilic glass beads) gave the best performance, with 46% conversion and 88% ee (Table 3). This biocatalyst was further applied in a continuous-flow setup, yielding a dopamine conversion of 28 mM and 98% ee under steady-state conditions. While stability and reusability were not assessed, the study demonstrated the potential of immobilized *Pb*NCS for continuous biocatalysis, a promising direction for industrial applications.

Table 3. Conversions and enantiomeric excesses of immobilized samples (Lechner et al., 2018).

Sample	Conditions	Catalyst amount (mg mL^{-1})	Conversion (%)	e.e (%)
Cells	2 h	10	27	>98
Alginate	2 h	50	31	65
Diaion HP-2MG	0.5 h	50	20	30
Diaion HP-2MG	0.5 h 10% MeOH	50	28	>98
Amberlite FPC-3500	0.5 h	50	17	racemic
YTONG	0.5 h	100	12	racemic
ABT HIGH Density NICKEL	0.5 h	15	16	56
EziG1	0.5 h	50	33	66
EziG2	0.5 h	50	43	86
EziG3	0.5 h	50	46	88

Arnold and Castiglione (2023) developed a two-step chemoenzymatic continuous-flow system for the asymmetric synthesis of (S)-norlaudanosoline using whole-cell biocatalysts expressing PsNCS2 and transaminase CV2025. After optimizing enzyme expression and cell ratios in batch mode (best result: 96% conversion, >95% ee with TAm/NCS ratio of 0.055), five immobilization strategies were tested. Overgrown Diaion HP-2MG yielded the highest conversion (64%) and was selected for the continuous-flow setup (Arnold; Castiglione, 2023).

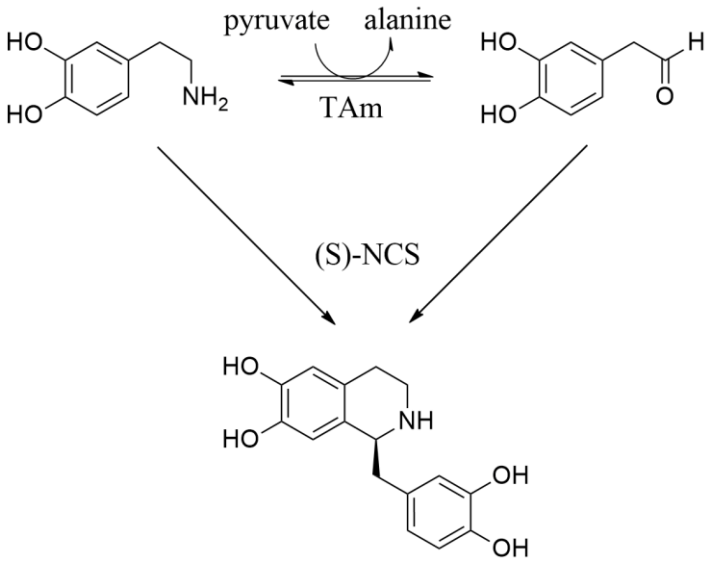

Figure 13. Schematic representation of the one-pot triangular cascade proposed by Lichman et al. (2015) and applied by Arnold and Castiglione (2023).

In a 5 mL 3D-printed column, the system maintained high ee (97%) with modest yield (6.5% decreasing to 5.8% after 80 CVs), achieving 118 mg (*S*)-norlaudanosoline per gram of dry cell mass per hour. Scale-up to a 48 mL packed-bed reactor (5.5 g catalyst) improved initial yield

to 88% with 94% ee, but productivity declined over time due to cell washout and partial enzyme deactivation. A 16% biomass loss and 48% activity drop after 48 h highlighted stability challenges. The authors proposed strategies to improve long-term performance, including protease-deficient strains and enhanced immobilization via coatings or covalent binding.

1.3 Enzyme Immobilization

Enzyme immobilization consists of enzyme(s) association to a solid structure, while retaining as much of their catalytic activity as possible after the process. This approach aims to overcome limitations associated with the use of free enzymes, such as low stability under elevated temperatures, the presence of organic co-solvents, or reaction conditions that differ from those found in biological systems. Immobilization yields heterogeneous biocatalysts that can be easily recovered from the reaction medium, enabling their reuse or application in continuous-flow systems (Britton; Majumdar; Weiss, 2018; Guisan et al., 2020).

1.3.1 Enzyme Stabilization Through Immobilization

Enzyme immobilization not only facilitates the separation and reuse of biocatalysts but also plays a fundamental role in the structural and functional stabilization of enzymes under adverse conditions. This stabilization can manifest in several ways, including increased thermal resistance, protection against denaturing agents (such as organic solvents), and improved operational stability in industrial processes.

1.3.1.1 Thermal Stabilization.

The thermal stability of immobilized enzymes often surpasses that of their non-immobilized counterparts. One of the possible mechanisms responsible for this effect is the conformational restriction imposed by the binding of the enzyme to a solid support (Klibanov, 1979), but other stabilizing effects associated with protein-material interactions can also influence this phenomena. A clear example of this phenomenon is found in the study by Ariaeenejad and Motamedi (2025), in which a metagenomic protease (PersiProtease1) was immobilized on carboxylated nanocellulose derived from quinoa husk residues using two distinct strategies: physical adsorption onto carboxylated nanocellulose (CNC) and covalent bonding to CNC activated with dicyclohexylcarbodiimide (DCNC). The enzyme's activity was evaluated across different temperatures, revealing that the free enzyme displayed maximum activity at 60 °C,

followed by a sharp decline above 80 °C, reaching only 51% residual activity at 90 °C. In contrast, immobilization shifted the temperature optimum to 80 °C. Under these conditions, the adsorbed form (PersiProtease1/CNCs) retained 65% of its activity at 90 °C, while the covalently immobilized form (PersiProtease1/DCNCs) retained 83%, indicating a significant enhancement in thermal stability (Ariaeenejad; Motamedi, 2025).

The authors attribute this effect to the increased conformational rigidity imposed by immobilization, particularly when covalent bonding is involved, which raises the activation energy required for enzyme unfolding and thus hinders thermal denaturation processes. However, the data also indicate that, although immobilization enhances catalytic performance at elevated temperatures, the same structural rigidity may impair activity at milder temperatures. This is due to the limited conformational flexibility, which is essential for the catalytic efficiency of the free enzyme under low-temperature conditions. Additionally, the authors suggest that steric effects and diffusional constraints resulting from immobilization may contribute to a slight reduction in activity at moderate temperatures when compared to the free enzyme. In summary, the results of this study illustrate how different immobilization strategies can distinctly affect the thermal performance of the enzyme, highlighting the central role of conformational rigidity in catalytic stabilization under extreme conditions (Ariaeenejad; Motamedi, 2025).

1.3.1.2 Stability against Organic Solvents and Denaturing Agents.

The presence of organic co-solvents represents a significant challenge to the structural and functional stability of enzymes in solution, as these compounds tend to denature proteins by disrupting hydrophobic, electrostatic, and hydrogen bonding interactions. However, immobilized enzymes often exhibit considerably greater resistance to such agents. This stabilization can be explained by the interactions between enzyme and material, and also by the possibility of formation of a protective microenvironment around the enzyme, provided by the support matrix (Guisan et al., 2020).

The gain in enzymatic stability in organic solvent-containing media can be advantageous both because it allows the enzyme to catalyze reactions involving substrates with low solubility in aqueous media and because certain enzymes may exhibit a different catalytic profile in organic media compared to aqueous environments. An example of this is lipases, which catalyze the

hydrolysis of esters to alcohols in aqueous media but promotes transesterification reactions of esters in organic solvents (Jesionowski; Zdarta; Krajewska, 2014; Klibanov, 2001).

One example of enzyme stabilization through immobilization is the encapsulation of cross-linked enzyme aggregates (CLEAs) of penicillin G acylase (PGA) within polyvinyl alcohol (PVA) hydrogels, forming so-called LentiKats. These biocatalysts demonstrated remarkable stability in an organic solvent: while the free enzyme was immediately denatured in a medium containing 75% (v/v) dioxane, the non-encapsulated CLEA had a half-life of only 8.9 hours, whereas the encapsulated CLEA remained fully active even after 300 hours of incubation under the same conditions. This difference was attributed to the "partitioning effect" provided by the highly hydrophilic nature of the hydrogel, which partially excludes the co-solvent from the interior of the matrix, thereby protecting the enzyme from direct solvating denaturation (Wilson et al., 2004).

Additionally, this type of encapsulation has also been shown to prevent enzyme aggregation and inactivation under harsh operational conditions. Analysis of dioxane distribution revealed a significantly lower concentration of the solvent inside the LentiKats, which reinforces the hypothesis of physical isolation from the aggressive environment, contributing to the preservation of the enzyme's catalytic activity (Wilson et al., 2004).

Moreover, the immobilization of enzymes in porous materials—regardless of the immobilization method—is an example of a stabilization strategy that prevents enzyme inactivation without necessarily requiring stabilization of its three-dimensional structure. Within the pores, enzymes are shielded from hydrophobic interfaces that may arise inside reactors, such as air bubbles or phase boundaries generated by agitation in biphasic systems and thus do not undergo unfolding due to interactions with such interfaces (Figure 14). In addition, being immobilized within the porous network, these enzymes typically do not undergo aggregation in the presence of co-solvents or under high-temperature and extreme pH conditions (Guisan et al., 2020, 2022).

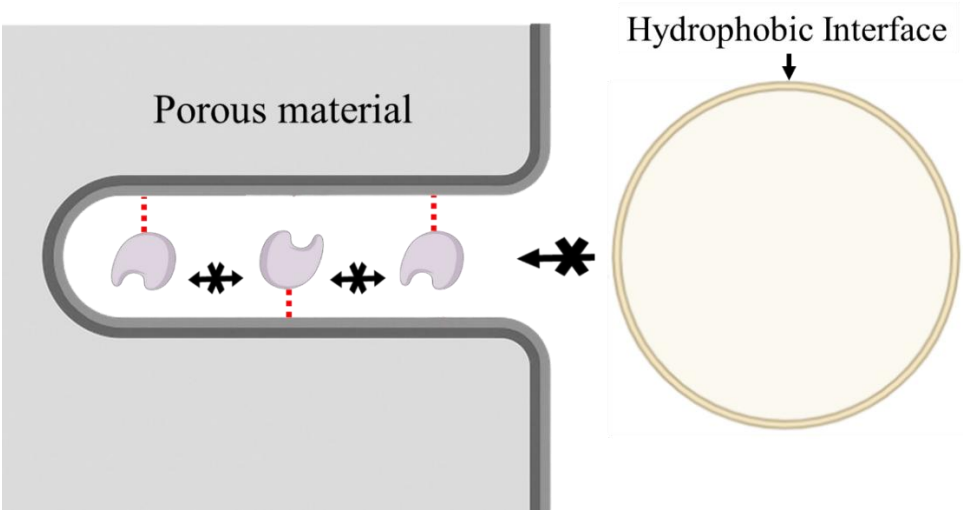

Figure 14. Generic representation of enzyme immobilization within a porous material. Inside the pores, enzymes are protected from interaction with hydrophobic interfaces, and enzyme aggregation is hindered. Figure created using https://biorender.com/ and Bioart.

This protective effect conferred by porous materials was explored by Uyama et al. (2024), who developed chitosan monoliths with hierarchical porosity for the immobilization of the enzyme α-amylase. The porous matrix, composed of interconnected macropores and mesoporous regions, provided an ideal microenvironment for the enzyme, combining substrate accessibility with physical confinement capable of minimizing denaturing effects. The authors employed both adsorption-based immobilization and covalent bonding mediated by epichlorohydrin (at varying concentrations). In both cases, the resulting biocatalysts outperformed the free enzyme in terms of resistance to thermal inactivation and stability across a broad pH range (Hajili; Sugawara; Uyama, 2024).

Notably, the monoliths with a higher degree of cross-linking (matrices with greater epichlorohydrin concentration) retained catalytic activity even after multiple cycles of use, indicating that the hierarchical structure of the support and the multipoint immobilization acted synergistically to protect the enzyme against denaturation, leaching, and aggregation under adverse conditions. These findings reinforce the importance of support structural design as a key factor in the functional stability of immobilized enzymes when exposed to organic solvents, pH fluctuations, and temperature variations (Hajili; Sugawara; Uyama, 2024).

1.3.2 Immobilization Techniques

Enzyme immobilization can be carried out using different strategies, each with specific advantages and limitations in terms of stability, catalytic activity, reusability, and cost. The main

approaches include adsorption, covalent binding, affinity immobilization, encapsulation, and cross-linked enzyme aggregates (CLEAs). Additionally, the choice of the system to be immobilized is also an important variable: one may work with purified enzymes, crude extracts, or even whole cells, each presenting different requirements and industrial applications. The direct immobilization of lysates or cells, for example, allows for reduced purification costs and, in some cases, provides greater robustness to the immobilized system by preserving natural interactions that stabilize the enzyme. On the other hand, the immobilization of purified enzymes prevents the occurrence of side reactions and generally ensures greater stereoselectivity (Guisan et al., 2020).

The following section will discuss the main immobilization methods, highlighting their technical characteristics, binding mechanisms, and practical examples. At the end of the section, special emphasis will be given to the adsorption technique, which holds relevance in the context of this work.

1.3.2.1 Covalent binding immobilization

Covalent enzyme immobilization involves attaching enzymes to solid supports through stable chemical bonds, offering strong and durable linkage between the enzyme and the material. These bonds form between functional groups on the support surface and specific amino acid residues (e.g., lysine, cysteine, aspartic acid, glutamic acid) on the enzyme (Júnior et al., 2021). Common functional groups used include epoxides (Ali et al., 2022), aldehydes (De Souza Lima et al., 2022; H. Orrego et al., 2018), carboxyls (Li et al., 2013), and thiols (Zhang et al., 2014), often introduced via surface functionalization strategies like glutaraldehyde or epichlorohydrin treatment. Spacers (e.g., APTES) can be employed to improve enzyme accessibility and activity (De Souza Lima et al., 2022).

A wide variety of natural (cellulose, chitosan) and synthetic (silica, polyacrylamides, magnetic nanoparticles) materials have been used, with the choice influencing enzyme stability, activity, and recovery (Júnior et al., 2021). Examples include Relizyme™ HA403 for co-immobilizing PDH and CHMO (Mallin; Wulf; Bornscheuer, 2013), silver nanodendrites (Rezaei et al., 2019), epoxy-silica (El-Zahab; Jia; Wang, 2004), and NHS-functionalized magnetic beads (Tan et al., 2016). While covalent immobilization offers high operational stability and reusability, especially in continuous-flow or organic systems, it requires careful planning to avoid modification of active site residues or enzyme denaturation due to harsh reaction conditions.

Enzyme orientation and preservation of catalytic accessibility are crucial for maintaining biocatalyst performance (Guisan et al., 2020, 2022).

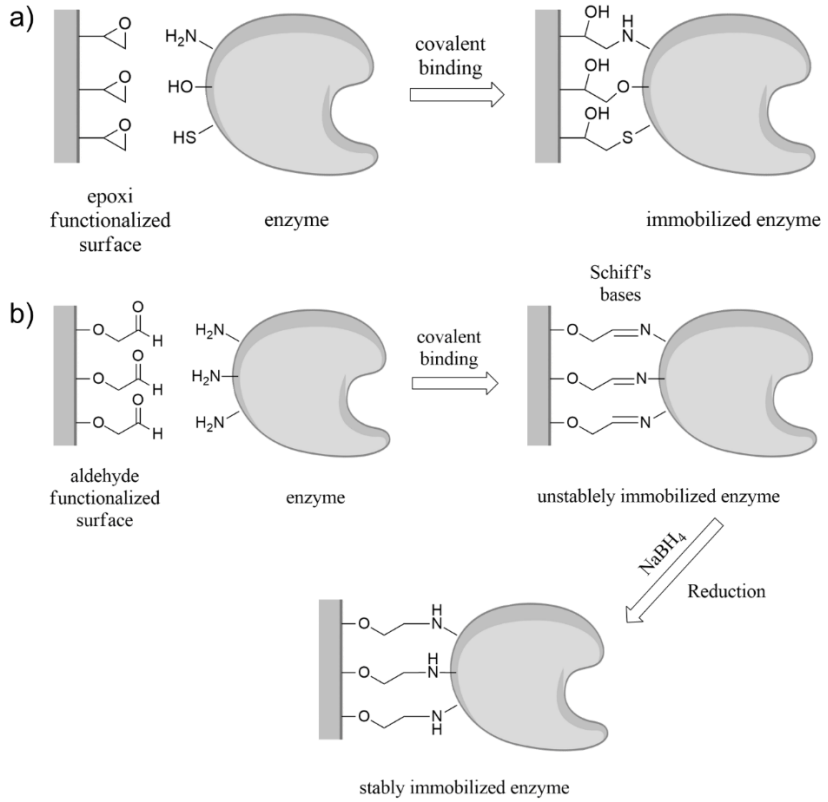

Figure 15. Examples of covalent immobilization mechanisms on functionalized surfaces. **a)** epoxy functionalized surface; **b)** aldehyde functionalized surface. Enzyme icon taken from Bioart.

1.3.2.2 Affinity immobilization

Affinity immobilization involves the use of specific interactions between groups present on the surface of the support material and particular amino acid residues of the enzyme (Britton; Majumdar; Weiss, 2018). A well-known example is the coordination interaction between histidine residues and metal ions such as Ni^{2+} or Fe^{2+} (Lechner et al., 2018) and Co^{2+} (Velasco-Lozano et al., 2020). This feature is even used in the context of purifying enzymes containing a polyhistidine tag (His-Tag).

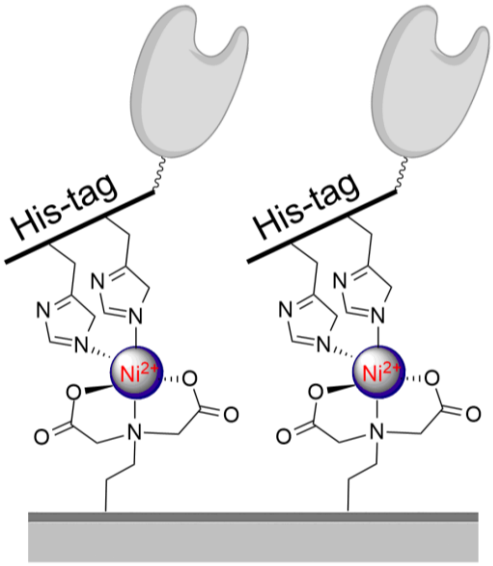

Figure 16. Ni-NTA affinity immobilization representation (Britton; Majumdar; Weiss, 2018). Enzyme icon taken from Bioart.

1.3.2.3 Encapsulation immobilization

Enzyme immobilization by encapsulation represents a relevant strategy to enhance the stability and catalytic efficiency of enzymes in various applied contexts. In this technique, the enzyme is physically confined within a polymeric matrix or structure, remaining immobile inside the capsules and not in direct contact with the reaction medium. Substrates and products diffuse through semipermeable membranes that surround the enzyme. This technique stands out from others due to the protection it provides against adverse reaction conditions, such as variations in pH, temperature, or the presence of organic solvents (Maghraby et al., 2023).

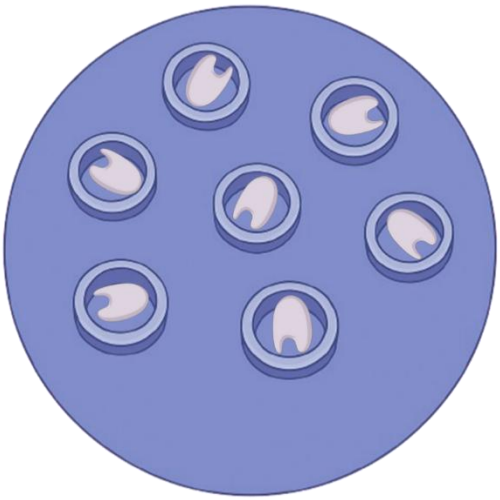

Figure 17. Encapsulation immobilization representation. Enzyme icon taken from Bioart.

Enzyme immobilization by encapsulation has been effectively applied using various materials and architectures to enhance biocatalyst protection and stability. Ji et al. (2015) encapsulated four dehydrogenases and NADH in hollow polymeric nanofibers via coaxial electrospinning, achieving high yields and reusability in CO_2-to-methanol conversion (Ji et al., 2015). Aranaz et al. (2015) encapsulated D-hydantoinase and D-carbamoylase in alginate–chitosan polyelectrolyte complexes, using one- and two-step methods to form gelled beads with good reusability and stability during lyophilization (Aranaz et al., 2015). Chen et al. (2018) used ZIF8 metal–organic frameworks to encapsulate dehydrogenases for pyruvate reduction, obtaining enhanced activity (5.3× higher than free enzymes), long-term stability, and low leaching (Chen et al., 2018). Despite these benefits, encapsulation may limit mass transport due to diffusional barriers and risks of structural rupture under certain conditions (Arnold; Castiglione, 2023; Júnior et al., 2021; Maghraby et al., 2023). Therefore, successful application depends on balancing enzyme protection with catalytic accessibility through careful control of matrix properties and operating parameters.

1.3.2.5 Cross-Linked Enzymes Aggregates (CLEAs)

The immobilization of enzymes through cross-linked enzyme aggregates (CLEAs) represents an approach distinct from traditional solid-support-based methodologies. Unlike conventional immobilization, CLEAs eliminate the need for carrier materials, thereby reducing associated costs and avoiding the dilution of catalytic activity by inert mass. This is a carrier-free immobilization technique in which the enzyme itself forms the biocatalyst structure, being covalently cross-linked by cross-linking agents, typically after the formation of enzyme aggregates (Cao; Van Rantwijk; Sheldon, 2000). The production of cross-linked enzyme aggregates (CLEAs) involves enzyme precipitation followed by cross-linking, typically using agents like glutaraldehyde, to form stable, insoluble biocatalysts. This method is simple, cost-effective, and yields high enzyme recovery, making it attractive for industrial use (Júnior et al., 2021).

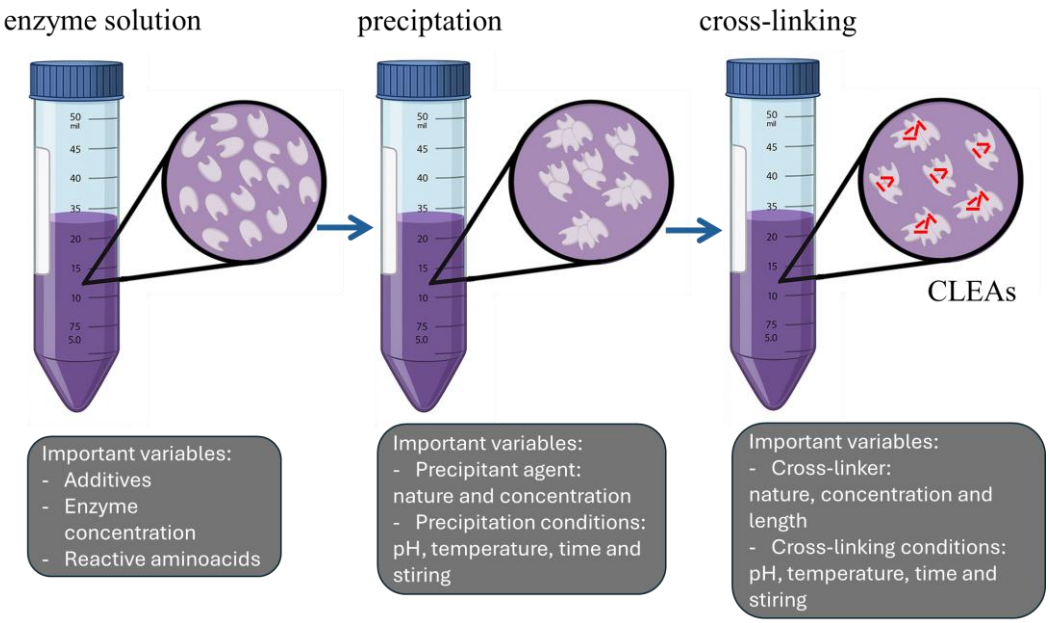

Figure 18. CLEAs production simplified protocol. Red lines represents the covalent bonds (Júnior et al., 2021). Icons were taken from Bioart and Bioicons.

Hernández-García et al. (2017) optimized CLEA formation using glycerol diglycidyl ether (GDE), achieving 98% activity recovery and improved thermal stability compared to glutaraldehyde-based CLEAs (Cochran; Cox, 1992; Hernández-García; García-García; García-Carmona, 2017; Myers; Montgomery; Anderson-Cook, 2016). Velasco-Lozano et al. (2014) introduced a carboxyl-based cross-linking method using a carbodiimide–succinimide system and PEIs, producing CLEAs from *Candida rugosa* lipase with superior activity, stability, and enantioselectivity (Velasco-Lozano et al., 2014). Jia et al. (2017) developed magnetic CLEAs (mCLEAs) by incorporating functionalized magnetic nanoparticles during cellulase cross-linking, enabling easier recovery and better thermal performance (Jia et al., 2017). Although CLEAs offer significant benefits, challenges remain in their recovery, especially in viscous media or continuous processes. Strategies like co-precipitation with polymers or magnetic particles can help address these limitations and enhance CLEA applicability (Júnior et al., 2021).

1.3.2.6 Adsorption immobilization

Enzyme immobilization by adsorption is considered the oldest and one of the simplest methodologies for anchoring enzymes to solid supports. It relies on reversible physical interactions between the enzyme and the surface of water-insoluble materials, such as hydrogen bonding, hydrophobic interactions, van der Waals forces, or combinations thereof. Although the non-covalent nature of these interactions makes the system more susceptible to desorption, it

also offers important advantages, such as preservation of the enzyme's structural integrity and the possibility of support regeneration. This technique has become particularly popular due to its operational simplicity, low cost, absence of toxic reagents, and good catalytic efficiency (Jesionowski; Zdarta; Krajewska, 2014; Júnior et al., 2021).

For a support to be suitable for adsorption, it must possess a high surface area, appropriate porosity for the intended application, good chemical and mechanical resistance, and insolubility in aqueous media. Additionally, it is important that the materials used exhibit functional groups on their surface that enable the formation of enzyme–material interactions. If these groups are not naturally present in the desired material, pre-immobilization surface modifications can be performed to introduce the necessary functionalities (Jesionowski; Zdarta; Krajewska, 2014). The types of materials that can be used are presented in Figure 19.

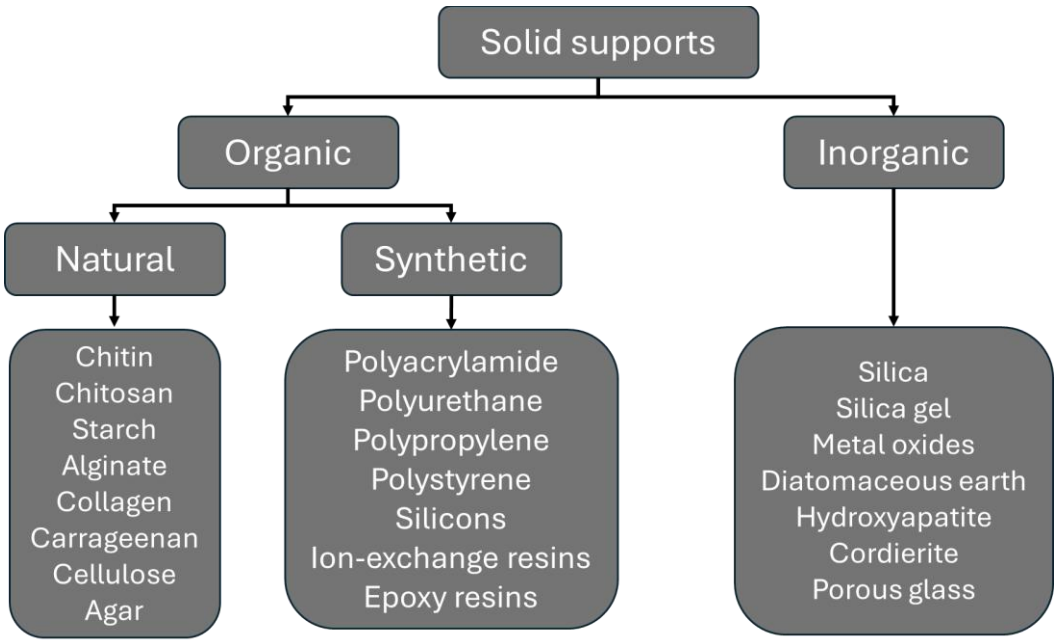

Figure 19. Types of materials used in enzyme immobilization by adsorption. (Jesionowski; Zdarta; Krajewska, 2014).

Among the most commonly used materials for adsorption-based immobilization, silicas stand out due to their high surface area, broad availability, low cost, good thermal stability, and high chemical resistance. These favorable properties are also observed in minerals such as mica and hydroxyapatite, which have been explored as supports due to their suitability for enzyme immobilization. Metal-based supports made of titanium, aluminum, or zirconium exhibit high mechanical strength and may establish strong interactions with specific enzymatic groups—an advantage in some cases, but one that can limit their applicability to certain systems. Magnetic materials, both organic and inorganic, have garnered significant interest because they allow the

recovery and control of the biocatalyst via magnetic fields. However, their high cost remains a barrier to large-scale implementation (Jesionowski; Zdarta; Krajewska, 2014).

Naturally derived materials such as chitin, chitosan, and cellulose have also been investigated, mainly due to their biocompatibility and availability. However, their use is limited by selective interactions with specific enzymes and by lower stability under process conditions. In contrast, synthetic polymeric matrices offer broad applicability, as they allow structural modifications tailored to the characteristics of the enzyme and the reaction medium. Additionally, these materials are typically easy and fast to produce and often exhibit good thermal and chemical resistance, making them versatile alternatives for more demanding catalytic systems (Jesionowski; Zdarta; Krajewska, 2014).

Here are some examples of the application of enzyme immobilization by adsorption, beginning with a natural organic material: cellulose membrane. Luo et al. (2022) developed a green and efficient method for multi-enzyme immobilization on cellulose membranes, aiming at the cascade conversion of CO_2 to methanol through either co-immobilization or sequential immobilization of the enzymes FDH, FaldDH, and ADH. The strategy was based on pressure-driven filtration, with adsorption serving as the mechanism for enzyme anchoring. The resulting enzyme-loaded membranes were then used as biocatalysts in continuous flow processes. The results showed that both immobilization strategies fully preserved enzymatic activity; however, the step catalyzed by FaldDH was identified as the rate-limiting step, restricting the overall efficiency of the cascade. Thus, while co-immobilization offered no major advantages, sequential immobilization allowed for individual optimization of each catalytic step and enhanced mass transfer under continuous flow conditions (Luo et al., 2015).

Another example of adsorption-based immobilization on an organic material, this time synthetic, involves the use of anionic macroporous polymethyl methacrylate particles. Valikhani et al. proposed the development of a self-sufficient and recyclable heterogeneous system based on the co-immobilization of the enzymes cytochrome P450 BM3 and glucose dehydrogenase (GDH) onto a solid anionic support functionalized with sulfopropyl groups (ReliSorb SP 400). Both enzymes were expressed as fusion proteins with the polycationic binding module Z_{basic2}, a peptide rich in arginine residues. (Gräslund et al., 2000) and were immobilized by adsorption onto the anionic material directly from the cell extract (lysate), without the need for prior purification. This strategy not only eliminates the purification step, but also allows precise control over the relative enzyme loading on the support, as well as

control over the orientation of the enzymes on the material surface (Figure 20) (Valikhani et al., 2018; Wiesbauer et al., 2011).

The system proved effective in the complete hydroxylation of lauric acid with high efficiency and internal NADPH regeneration from glucose, sustaining up to 27 consecutive cycles. This work underscores the potential of oriented enzyme immobilization by adsorption, guided and controlled by the presence of an electrically charged tag (in this case, Z_{basic2}) fused to a strategic region of the enzyme. It also highlights the importance of understanding the factors that govern adsorption-based immobilization, including the enzyme's orientation on the material surface (Valikhani et al., 2018).

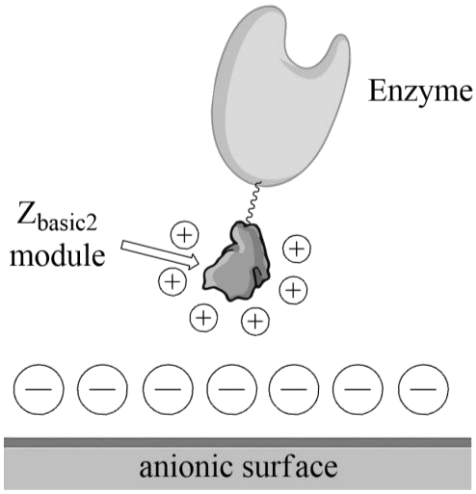

Figure 20. Strategy for oriented immobilization of chimeric enzymes through the Z_{basic2} binding module (Valikhani et al., 2018; Wiesbauer et al., 2011).

Finally, examples of studies involving the use of the inorganic materials Celite and Kaolin will be presented, as these materials stood out in the present work, as will be discussed in the following chapters:

Celite 545 is a porous inorganic material widely employed as a support in enzyme immobilization processes. It is a purified form of diatomaceous earth, composed essentially of fossilized diatom frustules, which confer a highly porous structure and high surface area. This unique morphology favors the adsorption of biomolecules and ensures good substrate accessibility to the active site of the immobilized enzymes. Moreover, the presence of hydroxyl groups on the surface of Celite enhances its reactivity, facilitating the formation of physical interactions, such as hydrogen bonds and van der Waals forces, between the support and the enzymes. These characteristics, combined with its chemical stability, low cost, and broad

availability, make Celite 545 an attractive support for the development of heterogeneous biocatalysts (Cruz et al., 2024; Han et al., 2009; Satar; Husain, 2009).

Satar and Husain (2009) investigated the immobilization of peroxidase extracted from white radish directly onto Celite 545 using a simple adsorption process from a partially purified enzyme preparation obtained via ammonium sulfate fractionation. Following adsorption, the enzyme was cross-linked with glutaraldehyde to enhance its stability. The resulting biocatalyst retained 60% of its initial activity after cross-linking and, while maintaining the same optimal pH and temperature as the non-immobilized enzyme (pH 5.5 and 40 °C), the immobilized preparation demonstrated reusability over six consecutive cycles and superior storage stability compared to the free form, retaining approximately 60% of its activity after 40 days at 4 °C (Satar; Husain, 2009).

Kaolin, on the other hand, is a natural clay mineral primarily composed of kaolinite, a hydrated aluminum silicate with a layered structure characterized by alternating sheets of silica tetrahedra (SiO_4) and alumina octahedra ($Al(OH)_6$), held together by hydrogen bonds. This structure endows the material with unique physicochemical properties, including thermal stability, low swelling in the presence of water, and a considerable specific surface area, which can vary depending on the geological origin and degree of processing. Studies such as that by Szewczuk-Karpisz et al. (2020) highlight the presence of hydroxyl and aluminol functional groups on the surface of kaolinite particles, which play a key role in interacting with ionic or molecular species through both physical and chemical adsorption mechanisms (Szewczuk-Karpisz et al., 2020).

Moreover, the surface of kaolin exhibits pH-dependent charge characteristics, with a tendency toward protonation of surface groups in acidic media and deprotonation in basic conditions, which significantly influences its adsorptive capacity. The combination of its lamellar structure, presence of active sites, and surface variability makes kaolin a promising support for enzyme immobilization by adsorption, particularly when a low-cost, abundant, and chemically stable alternative is sought. According to Palomino et al. (2008), kaolinite particles display a platy morphology and high specific surface area, enabling electrostatic interactions and the formation of colloidal networks in suspension, which can be leveraged to enhance enzyme binding in aqueous systems (Palomino; Burns; Santamarina, 2008).

An example of kaolin application as a support for enzyme immobilization by adsorption was presented by Šekuljica et al. (2016), who studied the binding of horseradish peroxidase (HRP)

onto natural kaolin without any prior chemical functionalization. The immobilization was carried out through physical adsorption, with pH 5.0 identified as the optimal condition for maximum immobilization efficiency. The immobilized enzyme preparation showed promising catalytic performance in the decolorization of the anthraquinone dye C.I. Acid Violet 109, achieving up to 87% removal under optimal conditions (pH 5.0, 24 °C, 40 mg/L dye, and 0.2 mM H_2O_2 within 40 minutes). These results demonstrate the tangible potential of the biocatalyst for application in industrial wastewater remediation processes involving dye contaminants (Šekuljica et al., 2016).

In addition to its high catalytic efficiency, the immobilized enzyme exhibited significant improvements in thermal stability, pH tolerance, and reusability. After seven consecutive cycles of use, the preparation retained approximately 35% of its initial activity. Additionally, immobilization reduced enzyme inhibition by dyes and co-substrates, enabling the effective treatment of higher dye concentrations—an advantageous feature for industrial wastewater remediation applications (Šekuljica et al., 2016).

In another study involving this material, Lima et al. (2021) evaluated the immobilization of endoglucanase on natural kaolin using two distinct approaches: physical adsorption and covalent binding. Covalent immobilization was performed after functionalizing the support with APTES and activating it with glutaraldehyde, while adsorption used untreated kaolin. Both strategies yielded similar immobilization efficiencies (60–65%) and preserved the catalytic properties of the free enzyme, with optimal activity observed between pH 4–5 and temperatures of 45–55 °C. Covalent immobilization provided greater thermal stability, allowing enzyme activity up to 75 °C, and both preparations retained 100% of their activity after 24 h at 50 °C and after 30 days at 4 °C (De Souza Lima et al., 2021).

Both immobilized systems were reusable for up to eight cycles, retaining approximately 86% of their initial activity, a performance superior to that reported in previous studies involving other enzymes and supports. Despite the greater robustness typically associated with covalent immobilization, physical adsorption proved equally effective, standing out for its simplicity, low cost, and sufficient stability for continuous use. These findings highlight the potential of kaolin as a promising natural matrix, even in the absence of chemical modifications, and demonstrate the practical viability of adsorption as a strategy for industrial applications.

While a considerable number of publications have explored the use of kaolin and Celite as matrices for enzyme immobilization via adsorption, to the best of the author's knowledge, none

have attempted to investigate the factors that may influence enzyme adsorption on these surfaces. In the present work, Monte Carlo simulations were employed to achieve a deeper theoretical understanding of these factors and to provide insights into the possible orientations of the enzyme on the kaolin surface (De Souza Lima et al., 2021).

2 OBJECTIVES

2.1 General Objective

To improve the biocatalytic performance of the heterologously expressed enzyme (S)-Norcoclaurine Synthase (variant Δ19*Tf*NCS) through the development of an adsorption immobilization methodology on low-cost materials, suitable for application in enantioselective Pictet-Spengler reaction.

2.2 Specific Objectives

1. To develop a robust expression and purification protocol for the Δ19*Tf*NCS variant, enabling its use as a biocatalyst in enantioselective Pictet–Spengler reactions.
2. To identify low-cost inorganic supports that are chemically and structurally suitable for the efficient immobilization of Δ19*Tf*NCS by physical adsorption.
3. To develop and optimize immobilization protocols that ensure high enzyme loading while preserving the catalytic activity of Δ19*Tf*NCS.
4. To evaluate the effect of immobilization on the catalytic performance of Δ19*Tf*NCS, including reusability, thermal stability, and tolerance to organic solvents.
5. To verify the preservation of the stereoselectivity of Δ19*Tf*NCS after immobilization using enantioselective chromatographic techniques.
6. To investigate, at molecular level, the mechanisms underlying the adsorption of Δ19*Tf*NCS onto the selected support through computational simulations, identifying key residues and preferred binding orientations.

3 MATERIALS AND METHODS

In this section, the materials and methods used to achieve the proposed objectives are presented. **It is important to note that, to provide a better understanding of the reasoning followed throughout the doctoral research, some methods, results, and discussions from the author's previous master's degree work will also be included in this thesis.** The experiments involved in the master's research are described *Material Selection and Immobilization of (S)-NCS*, along with the corresponding analyses of immobilization yield and reaction yield related to this step. The protocol for sample analysis by ^{1}H NMR was also established during the master's research and applied throughout all analyses in the doctoral work.

3.1 (*S*)-NCS expression and purification.

This section addresses the expression and purification of the Δ19*Tf*NCS enzyme, as well as the process of selecting the most suitable materials for the immobilization of (*S*)-NCS. The *Tf*NCS variant was chosen due to its extensive documentation in the literature, with specific focus on the Δ19*Tf*NCS construct, which is easier to express owing to the removal of the N-terminal signal peptide (Samanani; Liscombe; Facchini, 2004).

The gene encoding the N-terminally His_6-tagged Δ19*Tf*NCS (coding for residues 19–210 of (*S*)-NCS from *Thalictrum flavum*) was synthesized and cloned by GenScript (Piscataway, USA) into a pET28a plasmid. The plasmid was transformed into *Escherichia coli* BL21 (DE3) cells.

Bacterial transformation was carried out via heat shock. Briefly, 2 µL of plasmid (1 nM) was added to 100 µL of competent *E. coli* cells in aqueous solution containing 0.1 M $CaCl_2$ in an Eppendorf-type microtube. The mixture was incubated in a water bath at 42 °C for 1 minute and 30 seconds, followed by incubation on ice (4 °C) for 10 minutes.

Following transformation, the cells were centrifugated at 3000 rpm for 3 minutes at 4 °C. The supernatant was discarded, and 500 µL of liquid Luria Bertani (LB) medium (pH 7.4) was added to the cells. The transformed cells were incubated at 37 °C for 1 hour, on NL 161-04 Shaker Incubator (New Lab), the culture was centrifuged again, and 450 µL of the supernatant was removed. The remaining cell suspension was gently resuspended and plated onto LB-agar medium with 50 µg mL^{-1} kanamycin. Plates were incubated at 37 °C for approximately 16 hours, resulting in colony formation. A single colony was selected for Δ19*Tf*NCS expression.

The selected transformed colony was initially grown in 100 mL LB medium containing 50 μg mL^{-1} kanamycin at 37 °C for 16 h. This pre-culture was then transferred into 900 mL of fresh LB medium containing the same antibiotic concentration and incubated at 37 °C. Protein expression was induced with 0.5 mM isopropyl-β-D-thiogalactopyranoside (IPTG) once the optical density at 600 nm reached 0.6–0.8. The culture was incubated at 18 °C for 16 hours.

Cells were harvested by centrifugation at 4000 rpm for 40 minutes at 4 °C (Thermo Scientific TX-750 Swinging Bucket Rotor, Thermo Fisher, USA). The cell pellet was resuspended in lysis buffer containing 20 mM sodium phosphate (pH 7.4), 40 mM imidazole, 500 mM NaCl, 2 mM 1,4-dithiothreitol (DTT), and 2 mM phenylmethylsulfonyl fluoride (PMSF). Lysis was performed by sonication, and the lysate was clarified by centrifugation at 11000 rpm for 1 hour at 4 °C.

Δ19*Tf*NCS was purified from the lysate using Ni^{2+} affinity chromatography on a HisTrap HP Ni-NTA column (GE Healthcare, USA) equilibrated with 20 mM sodium phosphate buffer (pH 7.4) containing 40 mM imidazole and 500 mM NaCl. Elution was performed with a linear imidazole gradient up to 500 mM. Protein-containing fractions were further purified by size-exclusion chromatography in a Superdex 75 10/300 GL column (GE Healthcare, USA) pre-equilibrated with 50 mM HEPES (pH 7) and 100 mM NaCl.

The purified protein was stored at −20 °C for future use. Protein purity was assessed by SDS–PAGE electrophoresis, and concentration was determined by UV/Vis spectroscopy at 280 nm using an extinction coefficient of 19940 $M^{-1}cm^{-1}$, calculated from the His_6-tagged Δ19*Tf*NCS primary sequence using the Expasy ProtParam tool (Appendix) (Wilkins et al., 1999).

3.2 Material Selection and Immobilization of (*S*)-NCS.

Several low-cost, readily available, easy-to-handle materials were selected as potential matrices for (*S*)-NCS immobilization. The screened materials included Celite 545 (Fisher Scientific), Kaolin (Química Moderna), Diaion HP-2MG (Sigma Aldrich), silica gel (Sigma Aldrich), Dowex 1X8 (anionic resin), Dowex 50WX4, and Dowex 50WX8 (cationic resins, Dow Chemicals). The following protocol was implemented:

Step 1: Screening of Matrix Reactivity:

In the initial screening step, the inertness of the selected materials was assessed under conditions used in the biocatalytic Pictet-Spengler reaction and the absence of (*S*)-NCS, with

the reagents used in the Pictet-Spengler reaction, namely dopamine and hexanal. To this, 110 mg of each matrix was added to 5.0 mL of HEPES buffer (50 mM, pH 7) containing dopamine (2.5 mM), hexanal (2.5 mM), NaCl (100 mM), ascorbic acid (5 mM), and DMSO. The solution was stirred (180 rpm) at 37 °C for 1 h. The reaction mixture was centrifuged (3000 rpm, 4 °C, 10 min) to separate the solid matrix from the liquid medium. The supernatant was collected and stored at -20 °C for subsequent analysis. The inertness of each matrix was then assessed by monitoring changes in signals of dopamine and hexanal in the 1D ^{1}H NMR spectra of the solution before incubation and of the supernatant. Matrices not observed to cause changes in dopamine and hexanal concentrations were selected for the next step.

Step 2: Immobilization of (S)-NCS:

For this, 110 mg of each selected matrix was subjected to the immobilization protocol. The materials were washed thrice with HEPES buffer (50 mM, 100 mM NaCl, pH 7). Following the washing step, an appropriate volume of (*S*)-NCS stock solution was added to each matrix-containing medium, along with HEPES buffer for dilution. The final volume was adjusted to 248 µL, achieving a (*S*)-NCS concentration of 0.95 mg mL^{-1} in the immobilization medium.

The immobilization mixtures were homogenized for 1 hour at approximately 25 °C to facilitate enzyme adsorption onto the matrices. After immobilization, the samples were centrifuged (11,000 rpm, 4 °C, 10 min) using a Heraeus Fresco 17 centrifuge (Thermo Scientific, USA) to separate the solid matrices from the solution. The collected supernatants were submitted to Immobilization yields assessment described in the next section. Finally, the immobilized enzyme samples were washed three times with HEPES buffer (50 mM, 100 mM NaCl, pH 7) and subsequently used for reaction experiments.

Step 3 Enzymatic reaction:

Following immobilization, the matrices containing (*S*)-NCS were exposed to the same reaction conditions and sample collection and analysis protocol described in *Step 1* to evaluate the performance of each biocatalyst. Only the samples that successfully passed through screening steps were further evaluated for reuse, temperature profile, and dimethyl sulfoxide (DMSO) tolerance studies.

3.3 Assessment of (*S*)-NCS Immobilization Yields by UV/Vis spectroscopy

The following experimental procedure evaluated the immobilization yields of (*S*)-NCS on the matrices. The supernatants obtained in Step 2 of the last session were analyzed by UV/Visible spectroscopy using a Cary 50 Bio UV-Visible Spectrophotometer (Varian, USA). The absorbance at 280 nm was used to determine the concentration of (*S*)-NCS in the supernatant. The immobilization yield was calculated using equation 1 (Guisan et al., 2020).

$$\mathrm{IY}(\%) = \frac{\mathrm{C_i} - \mathrm{C_s}}{\mathrm{C_i}} \times 100\% \qquad \text{eq. 1}$$

Where: IY (%) is the immobilization yield expressed as a percentage. C_i is the initial enzyme concentration, and C_s is the enzyme concentration in the supernatant after immobilization.

3.4 Determination of Reaction Yield by Quantitative NMR Spectroscopy

The reaction yield for all experiments was determined using quantitative ^{1}H NMR spectroscopy. Samples were analyzed using a Bruker Avance Neo 600 MHz spectrometer equipped with a 5 mm double-resonance, multi-nuclear Z-gradient SmartProbe, located at the Laboratory of High-Resolution Magnetic Resonance (LAREMAR) of UFMG. ^{1}H NMR spectra were acquired, processed, and analyzed using Topspin 4.06 software (Bruker Inc., USA).

Sample Preparation for NMR Analysis:

Samples were prepared by mixing 538.5 µL of the reaction sample or control samples (reactants in HEPES buffer and 10% v/v DMSO) with 60 µL of D2O and 1.5 µL of a 55.58 mM stock solution of 2,2-dimethyl-2-silapentane-5-sulfonic acid (DSS), resulting in a final DSS concentration of 139 µM. The total volume of 600 µL was transferred into 5 mm NMR tubes for NMR experiments.

NMR Experiments:

^{1}H NMR spectra were acquired using the noesygppr1d pulse sequence with water signal suppression via pre-saturation. A recovery time of 20 seconds was applied to ensure proper relaxation between scans. The noesygppr1d pulse sequence was employed to suppress the water signal in the samples. This sequence had been previously validated for quantitative NMR analysis of aqueous samples (Løhre et al., 2021) and was therefore selected for this purpose in the present study.

The recovery delay was set to 20 seconds to ensure that hydrogen spins reached thermodynamic equilibrium, a prerequisite for quantitative analysis. This condition is met when the recovery time is at least five times longer than the longest longitudinal relaxation time (T1) in the sample (Santos; Colnago, 2013). These considerations underscore the potential of NMR spectroscopy as a technique capable of providing both quantitative and qualitative information simultaneously.

Calculation of Reaction Yield: The reaction yield (RY) was calculated using the following equation:

$$\mathrm{RY}(\%) = \frac{\mathrm{I4}'}{\mathrm{I4}' + \mathrm{I4}} \times 100\% \qquad \text{eq. 2}$$

Where: RY (%) represents the reaction yield expressed as a percentage, I4' is the integral of hydrogen 4 of the product, and I4 is the integral of hydrogen 4 of dopamine. All dopamine consumed during the reaction was assumed to be converted into the desired product. Therefore, the sum of I4 and I4' is the initial dopamine concentration.

3.5 Assessment of (*S*)-NCS Immobilization Yields on Kaolin and Celite 545

The following experimental procedure evaluated the immobilization yields of (*S*)-NCS on Kaolin and Celite 545 under varying conditions. **The methods described from this point onward, as well as the choice to use kaolin and celite 545, were carried out exclusively during the doctoral research.**

Kaolin and Celite 545 are mesoporous mineral-based materials. Kaolin is primarily composed of aluminum silicate hydroxide ($Al_2Si_2O_5(OH)_4$), while Celite 545 is a calcined diatomaceous earth consisting mainly of silicon dioxide (SiO_2), aluminum oxide (Al_2O_3), iron oxide (Fe_2O_3), sodium oxide (Na_2O), potassium oxide (K_2O), and calcium oxide (CaO). Both materials are low-cost, commercially available, and supplied in microparticulate form (with particle sizes in the range of tens of μm). In this study, kaolin from QM – Química Moderna (Brazil) and Celite® 545 from Thermo Fisher (USA) were used.

Kaolin (110 mg or 10 mg) and Celite 545 (110 mg) were added to aqueous solutions of (S)-NCS at concentrations of 1.0, 1.4, 3.8, or 7.5 mg mL^{-1}. The mixtures were homogenized for 1 and 3 hours to facilitate adsorption. Following immobilization, the samples were centrifuged (11,000 rpm, 4 °C, 10 min) using a Heraeus Fresco 17 centrifuge (Thermo Scientific, USA).

The supernatants were then analyzed by UV/Visible spectroscopy (Cary 50 Bio UV-Visible Spectrophotometer, Varian, USA). The absorbance at 280 nm was used to determine the concentration of (*S*)-NCS in the supernatant. The immobilization yield was calculated using equation 1

3.6 Immobilization of (S)-NCS onto Selected Material Supports

The immobilization of (*S*)-NCS onto the selected solid supports (Celite 545 and Kaolin) was as follows. Triplicate samples of 130 mg of Celite 545 and 10 mg of Kaolin (chosen due to its higher enzyme adsorption capacity) were weighed. The materials were washed thrice with HEPES buffer (50 mM, 100 mM NaCl, pH 7). Following the washing step, an appropriate volume of (*S*)-NCS stock solution was added to each matrix-containing medium, along with HEPES buffer for dilution. The final volume was adjusted to 248 µL, achieving a (*S*)-NCS concentration of 0.95 mg mL^{-1} in the immobilization medium. This concentration was diluted to 0.05 mg mL^{-1} in the final reaction medium (5 mL total volume). The immobilization mixtures were homogenized for 1 hour at approximately 25 °C to facilitate enzyme adsorption onto the matrices. After immobilization, the samples were centrifuged (11,000 rpm, 4 °C, 10 min) to separate the solid matrices from the solution. Finally, the immobilized enzyme matrices were washed three times with HEPES buffer (50 mM, 100 mM NaCl, pH 7) and subsequently used for reaction experiments.

3.7 Reaction Conditions and Catalytic Performance Evaluation of non-immobilized and Immobilized (*S*)-NCS.

The catalytic performance of non-immobilized and immobilized (*S*)-NCS was assessed by measuring reaction yield values. All reactions were conducted under the following conditions: dopamine (0.25 mM) and hexanal (2.5 mM) were added to the reaction medium (5 mL) consisting of HEPES buffer (50 mM, pH 7), NaCl (100 mM), ascorbic acid (5 mM), and DMSO (10% v/v, except in DMSO concentration profile experiments). The reaction medium containing DMSO was based on previous work conducted by Lichman et. al (2017).

The enzyme (either non-immobilized or immobilized) was added to achieve a final concentration of 0.05 mg/mL. Reactions were carried out at 37 °C (except in temperature profile experiments) with constant stirring (180 rpm) for 1 hour on NL 161-04 Shaker Incubator (New

Lab). Control samples, prepared without the enzyme, contained only the reactants on the reaction medium.

All experiments were performed in triplicate. Reactions were quenched by adding 1 mL of HCl (1 M). For immobilized enzyme samples, the reaction mixtures were centrifuged (3000 rpm, 4 °C, 10 min) to separate the solid matrices from the liquid medium. The supernatant was collected and stored at -20 °C for subsequent analysis. For non-immobilized enzyme samples, the reaction mixtures were centrifuged (2500 rpm, 4 °C, 20 min) using Centricon 25 mL concentrators (GE Healthcare) to remove the enzyme from the reaction medium. The enzyme-free supernatants were then frozen at -20 °C for further analysis.

3.8 Reaction recycle profile.

The reusability of the immobilized enzyme was evaluated over three reaction cycles. After each cycle, the immobilized enzyme samples were recovered by centrifugation, washed three times with 1 mL of HEPES buffer (50 mM, pH 7, 100 mM NaCl, 5 mM ascorbic acid, and 10% v/v DMSO), and then reused in the subsequent cycle.

3.9 Temperature and DMSO Concentration Profiles

The temperature profile of the reaction was assessed by conducting experiments at 37 °C, 47 °C, and 57 °C. For the dimethyl sulfoxide (DMSO) concentration profile, reactions were performed using DMSO concentrations of 10% v/v and 20% v/v.

3.10 Stereoselectivity assessment

The stereoselectivity of reactions catalyzed by immobilized and non-immobilized (*S*)-NCS was qualitatively evaluated using high-performance liquid chromatography (HPLC) with a chiral chromatography column. Reaction Protocol for Stereoselectivity Analysis: the reaction mixture was prepared by adding dopamine (10 mM), hexanal (20 mM), ascorbic acid (10 mM), and (*S*)-NCS (0.05 mg mL^{-1}) to a 10 mL buffer solution (HEPES 50 mM, 100 mM NaCl, pH 7, 10% v/v DMSO). HPLC Analysis: chromatography was performed using a Shimadzu LC- 20A system equipped with a chiral column (Astec CHIROBIOTIC T, 5 µm, 10 cm × 4.6 mm, Sigma-Aldrich, USA). The mobile phase consisted of a mixture of 20% v/v methanol (0.2% v/v acetic acid, 0.1% v/v triethylamine) and 80% v/v acetonitrile (0.2% v/v acetic acid, 0.1% v/v triethylamine), applied at a flow rate of 0.350 $mL.min^{-1}$. The column temperature was

maintained at 25 °C, and the total run time was 50 minutes. Analytes were detected using a UV/Vis detector at 280 and 230 nm wavelengths.

3.11 Characterization of Surface Properties.

Nitrogen Adsorption/Desorption Isotherms: Nitrogen Adsorption/Desorption experiments were made to determine the surface area, through Brunauer-Emmett-Teller (BET), model, of kaolin and Celite 545. Surface area values can provide deeper insight into the observed immobilization yields, as there is generally a direct relationship between surface area and the amount of immobilized enzyme, although this is not the only factor contributing to the phenomenon.

Considering the following BET equation :

$$\frac{P}{V(P_0 - P)} = \frac{1}{V_m C} + \frac{(C-1)P}{V_m C P_0} \qquad \text{eq. 3}$$

In which V is volume of gas adsorbed (per gram of sample), V_m is volume of gas adsorbed in the monolayer (cm^3/g) and C is the BET constant. Since P, P_0 and V can be obtained from $N_2(g)$ adsorption/desorption isotherm, the surface area can be obtained by plotting $P/V(P_0-P)$ versus P/P_0, which gives $(C-1)/(V_mC)$ as the line slope and $1/(V_mC)$ as y axis intercept (Ladavos et al., 2012). With those values V_m and C can be calculated and then used to calculate the specific surface area S_{BET}, which for $N_2(g)$ adsorption/desorption experiments is calculated by:

$$S_{BET}(m^2/g) = 4.35 \text{ x } V_m \qquad \text{eq. 4}$$

The experiment was carried out as follows: the samples first underwent degassing at 200 °C. Then, the $N_2(g)$ adsorption and desorption measurements were performed on the Autosorb 1 equipment (Quantachrome, USA) at 77 K. The surface area and total pore volume were calculated using the Brunauer-Emmett-Teller (BET) method (Simões et al., 2025).

Zeta Potential Measurements: Zeta potential experiments were conducted to determine the surface electrical charge of the kaolin and Celite 545 materials in the immobilization buffer (50 mM HEPES, 100 mM NaCl, pH 7). This information may aid in understanding the adsorption process, particularly with respect to electrostatic interactions.

Zeta potential is defined as the electric potential at the shear plane of the electrical double layer, formed by the Stern layer and the diffuse layer (Figure 21). It is widely used as an indirect measure of the effective surface charge of particles or solid interfaces dispersed in a liquid

medium. Experimental determination of zeta potential is typically performed using dynamic light scattering (DLS) instruments coupled with electrophoretic mobility analyzers. In this procedure, an electric potential is applied to the cell containing the dispersion, and the migration velocity of the particles under the applied electric field is recorded. The measured electrophoretic mobility is then converted into zeta potential values using appropriate electrokinetic models (Delgado et al., 2007).

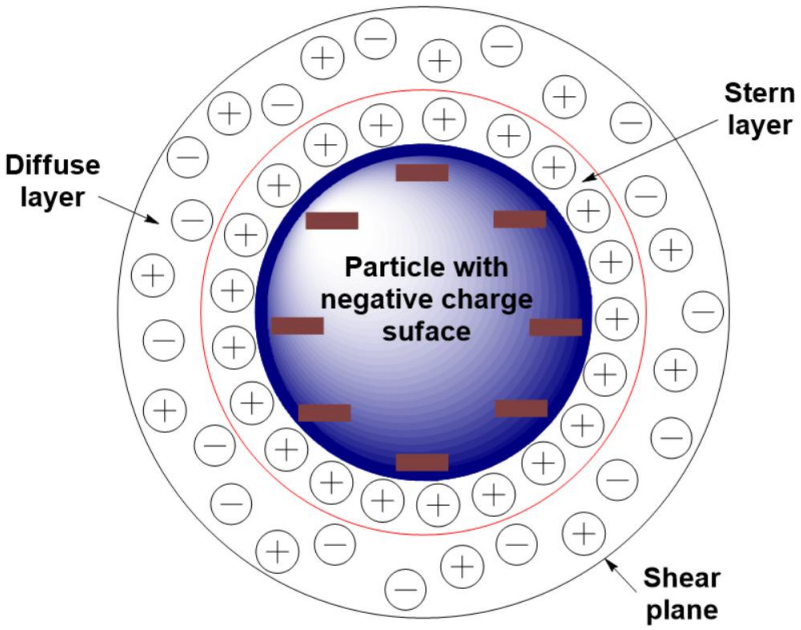

Figure 21. Schematic representation of the electrical double layer of a negative charged surface particle.

The zeta potential of the samples was measured using a Malvern Zetasizer Nano ZS (model BI-900, Worcestershire, United Kingdom) at the Pharmacy Department of UFVJM (**in collaboration with Prof. Dr. Rodrigo Verly**). The analyses used 700 µL Malvern cuvettes (model DTS1061) and monochromatic light scattering (10 mW Ne laser, λ = 632.4 nm). The intensity of the scattered light was measured at a 90° angle. For zeta potential determination, the samples were prepared at a concentration of 1 mg mL^{-1} in HEPES buffer (50 mM, 100 mM NaCl, pH 7).

3.12 Coarse-Grained Monte Carlo Simulations for (*S*)-NCS Adsorption on Kaolin

(*S*)-NCS interaction with Kaolin was computationally characterized using a coarse-grained model and the Metropolis Monte Carlo method, **which was made in collaboration with Prof. Dr. Sidney Jurado de Carvalho from Universidade Estadual Paulista (UNESP)**. The

Kaolin surface was modeled as a cylindrical pore with a surface density charge of σ = -0.3 C/m^2 and radius α = 6 nm, according to experimental values from references (Palomino; Burns; Santamarina, 2008; Szewczuk-Karpisz et al., 2020). The surface electrostatic potential, $\Psi(ri)$, was obtained using the solution of the linear Poisson-Boltzmann equation (Caetano et al., 2021; Cherstvy, 2012).

$$\Psi(r) = \frac{2\sigma K_0(\kappa\alpha) I_0(\kappa r)}{\varepsilon_0 \varepsilon_s \kappa [I_0(\kappa\alpha) K_1(\kappa\alpha) + I_1(\kappa\alpha) K_0(\kappa\alpha)]} \qquad \text{eq. 5}$$

Where r is the radial distance to the axis of the pore, I_n and K_n are the modified Bessel functions of first and second kind, respectively, ε_0 and ε_s = 78.7 are the permittivity of free space and the dielectric constant of the solvent, respectively, and κ = 1.0382 nm^{-1} is the inverse of Debye screening length, corresponding to an immobilization condition in which the salt concentration is 100 mM.

The (*S*)-NCS was modeled as a set of connected spherical beads, each one corresponding to an amino acid residue. The energy U(r, θ, ϕ) was calculated using the C-alpha Structure-Based Model (Caetano et al., 2021; Clementi; Nymeyer; Onuchic, 2000; Contessoto et al., 2016; De Oliveira et al., 2020; Koga; Takada, 2001; Whitford et al., 2009), which includes electrostatic interactions between the charged residues and between the charged residues and the charged surface. The energy function expression used is the following:

$$\begin{aligned} U(r,\theta,\phi) \; = & \sum_{\text{bonds}} \epsilon (r - r_0)^2 + \sum_{\text{angles}} \epsilon_\theta (\theta - \theta_0)^2 \\ & + \sum_{\text{dihedrals}} \epsilon_\theta \left[1 - \cos(\phi - \phi_0) + \frac{1}{2}(1 - \cos(3\phi - 3\phi_0)) \right] \\ & + \sum_{\text{contacts}} \epsilon_c \left[5 \left(\frac{d_{ij}}{r_{ij}} \right)^{12} - 6 \left(\frac{d_{ij}}{r_{ij}} \right)^{10} \right] \\ & + \sum_{\text{non-contacts}} \epsilon_{nc} \left(\frac{\sigma_{ij}}{r_{ij}} \right)^{12} \\ & + \sum_{\text{charges}} \left[\frac{z_i z_j e_0^2}{4\pi\epsilon_0\epsilon_s} \frac{\exp(-\kappa r_{ij})}{r_{ij}} + z_i e_0 \Psi(r_i) \right] \end{aligned} \qquad \text{eq. 6}$$

Where: r are the distances between pairs of consecutive residues, θ are the angles between three consecutive residues, and ϕ are the dihedral angles between four consecutive residues. The

values of r_0, θ_0, and ϕ_0, are the corresponding values of C-alpha in the native structure of (*S*)-NCS PDB (ID 5N8Q) (Lichman et al., 2017b) with the missing residues included using the software Modeller (Webb; Sali, 2016) (Figure 22). The r_{ij} are the distances between the i-th and j-th residues and d_{ij} are the distances between the same two residues ($j < i-3$) that form native contacts, according to the CSU (Contacts of Structural Units) contact map (Sobolev et al., 1999; Sobolev; Edelman, 1995). The repulsive interaction between residues that do not form native contacts was modulated by the parameter $\sigma_{ij} = 4$ Å (Caetano et al., 2021; Clementi; Nymeyer; Onuchic, 2000). The magnitude of the first three harmonic terms is modulated by the parameters $\epsilon_r = 100\epsilon_c$, $\epsilon_\theta = 20\epsilon_c$, and $\epsilon_\phi = \epsilon_{nc} = \epsilon_c$, as functions of the Lennard-Jones parameter ϵ_c (Caetano et al., 2021; Yu; Liu; Zhou, 2014; Yu; Zhou, 2016), which determines the magnitude of the attractive interaction energy between pairs of residues in contact in the native structure and is related to the melting temperature of the protein.

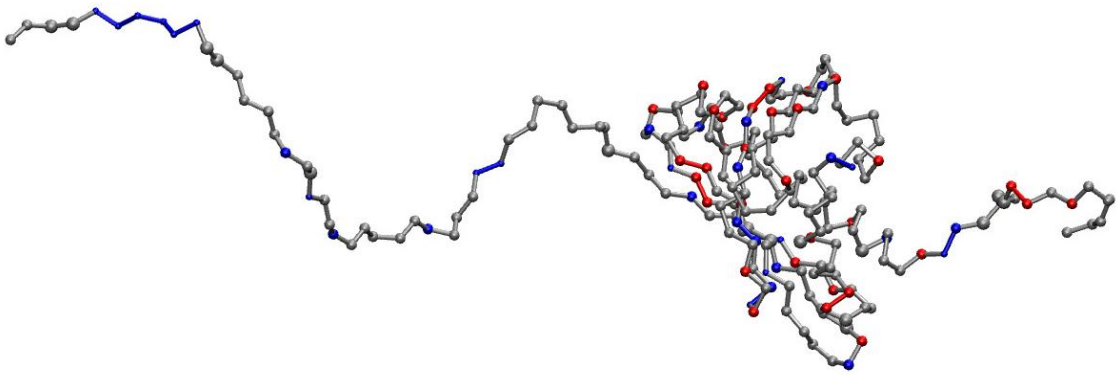

Figure 22. Structural snapshot of (*S*)-NCS highlighting all titratable residues at pH 7: positively charged residues (blue) and negatively charged residues (red). Note the concentration of positive charges in the N-terminal disordered sequence.

Following the procedure proposed in the reference (Caetano et al., 2021; Clementi; Nymeyer; Onuchic, 2000), the value of $\epsilon_c = 0.63$, used in this work, was determined so that the unfolding temperature obtained from simulations agrees with experimental melting temperature Tm = 335 K in order to properly model its experimental thermal stability. The last summation includes the electrostatic contribution, where e_0 is the electronic elementary charge z_i is the valence of the i-th residue and $\Psi(r_i)$ is the electrostatic potential at the i-th residue position, given by equation 5.

Constant-pH Monte Carlo simulations were employed to study the adsorption of (*S*)-NCS on the kaolin at pH 7 and 100 mM of salt concentration. To sample protein configurations, the used algorithm randomly chooses one out of five protein movements for each Monte Carlo step:

(1) translational displacement of a single random residue, (2) protein translational displacement, (3) protein rotation, (4) pivot rotation, and (5) crank-shaft rotation of a segment of the protein (Caetano et al., 2021; Sobolev et al., 1999). The configurations are accepted or rejected according to the Metropolis criterion (Sobolev et al., 1999; Stickler; Schachinger, 2016; Vitalis; Pappu, 2009). In 30% of the Monte Carlo steps, our algorithm changes the protonation state of a random titratable residue to sample the charge states of the protein residues. The new protonation state was also accepted according to the Metropolis criterion, with energy variation given by references (Lund; Jönsson, 2005; Reed; Reed, 1992).

$$\Delta U = \Delta U^{ES} \pm \chi[K_B T(pH - pK_a^0)\ln 10] \qquad \text{eq. 7}$$

Where ΔU^{ES} is the protonation-deprotonation electrostatic energy variation, pK_a^0 is the pK_a value of the randomly chosen residue in the absence of electrostatic interactions, $\chi = 1$ or -1 if the residue is basic or acidic, respectively and $K_B T$ is the thermal energy at room temperature (T = 298.15 K). The sign $\pm$ was positive for protonation and negative otherwise. The values of pK_a^0 of each titratable residue were taken from reference (Caetano et al., 2021). The average properties were calculated under 10^6 Monte Carlo steps, where each step corresponds to 10^3 attempts of the movements described above to decorrelate protein configurations.

4. RESULTS AND DISCUSSION

4.1 (*S*)-NCS expression and purification.

Nickel affinity chromatography was employed to purify the Δ19*Tf*NCS variant, which contains a polyhistidine tag (His-tag) in its structure, allowing its separation from other *E. coli* proteins released during cell lysis following expression. Histidine residues bind specifically to Ni^{2+} ions on the resin, enabling selective retention of the target protein. Subsequently, the application of an imidazole gradient, imidazole being a competitor for nickel binding sites, facilitates the controlled elution of the enzyme (Zeng; Li, 2004). As a result, Δ19TfNCS is gradually released from the column, yielding the purified protein. Figure 23 presents the nickel ion affinity chromatogram.

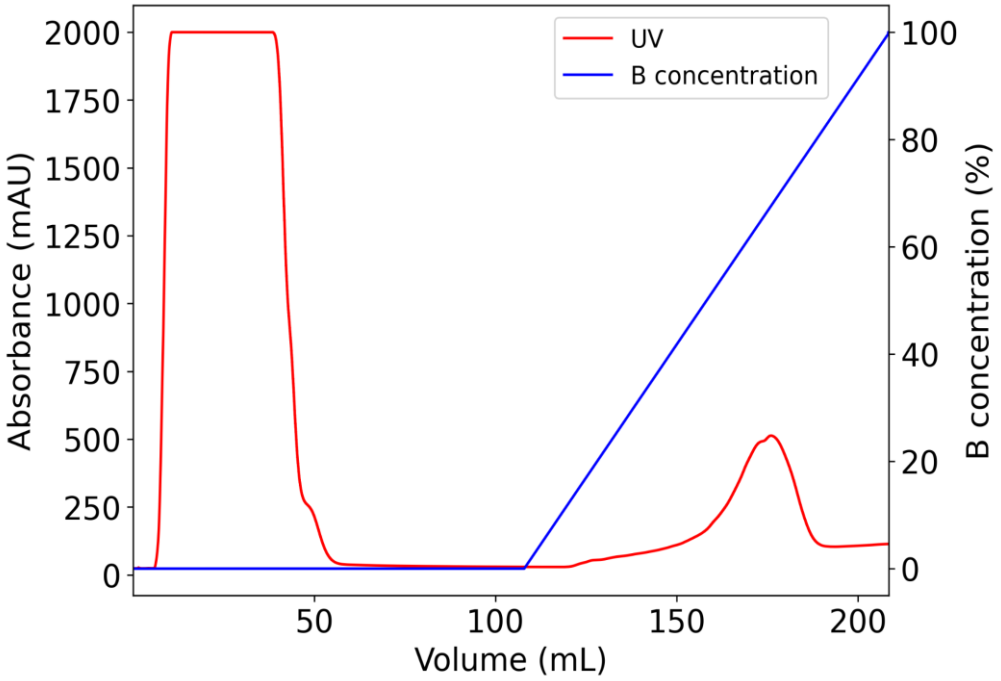

Figure 23. Chromatogram of Ni^{2+} affinity purification using a HisTrap HP Ni-NTA column (GE Healthcare, USA). Δ19*Tf*NCS-containing fractions were eluted between 150 and 190 mL (corresponding to ~40–90% buffer B), as indicated by the absorbance peak in this range. Buffers used: A (40 mM imidazole, 300 mM NaCl, 20 mM sodium phosphate, pH 7.4) and B (500 mM imidazole, 300 mM NaCl, 20 mM sodium phosphate, pH 7.4).

The impurities were eluted first, at low imidazole concentration (40 mM), which is indicated by the large and intense band between 0 and 60 mL. The protein was eluted at high imidazole concentrations (200–450 mM), indicating good accessibility of the N-terminal His_6 tag, likely due to this being an unstructured region of the protein (Berkner et al., 2007). This feature may

be is particularly advantageous considering the potential use of immobilization strategies that rely on interactions between the His-tag of Δ19*Tf*NCS and the surface of the support material.

Figure 24 presents the size exclusion chromatogram. Such a purification method enables the separation of proteins based on size differences, with larger proteins being eluted more quickly (Burgess, 2018). The protein was eluted first, which is indicated by the UV band beginning at 50 mL, then the imidazole was eluted after 100 mL (conductivity decrease band).

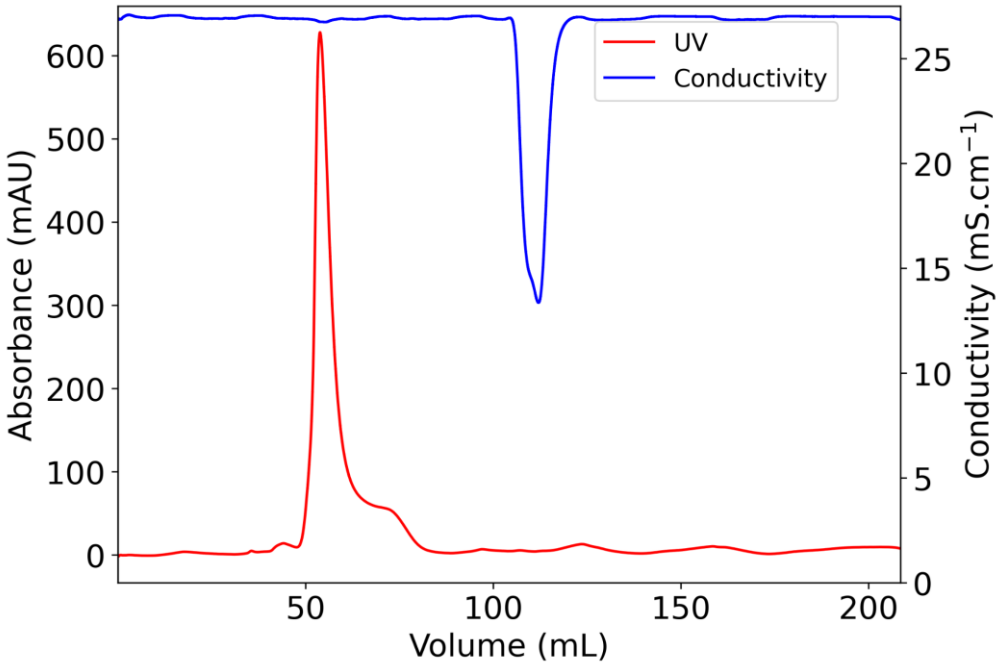

Figure 24. Chromatogram of size-exclusion purification using a Superdex 75 10/300 GL column (GE Healthcare, USA). Δ19*Tf*NCS eluted between 50–80 mL, confirming its presence by an absorbance peak in this range. The running buffer consisted of 50 mM HEPES, 100 mM NaCl, pH 7.

The fractions collected during the expression process were analyzed by SDS PAGE (Figure 25), allowing a qualitative assessment of the enzyme expression and purification process. On lanes 2 and 3 (lysate and lysis pellet), the bands of molecular mass about 23.4 kDa appears, corresponding to Δ19*Tf*NCS mass, which was calculated using the Expasy ProtParam tool (Apendix). On the other hand, the same protein is not present on Flow-Through sample, lane 5, which indicates a successful biding of the enzyme at His-Trap column resin.

Finally, the protein can be observed on the purified samples (lanes 6 and 7). Some impurities can be seen on lane 6, being eliminated latter on size exclusion chromatography purification step, lane 7.

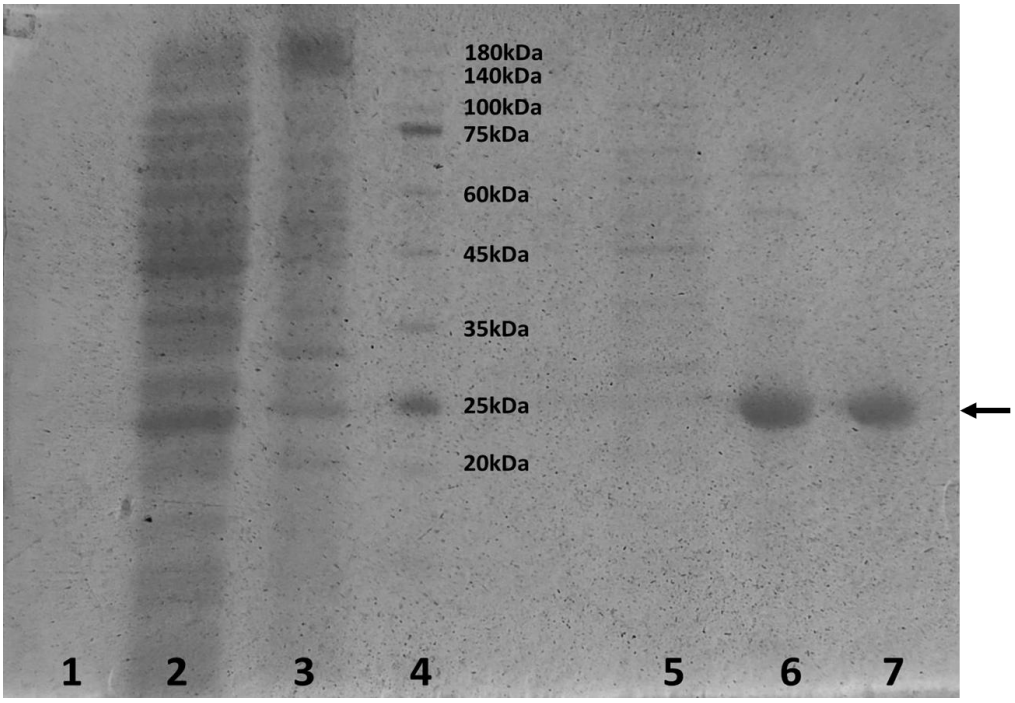

Figure 25. Electrophoresis gel of Δ19*Tf*NCS expression and purification samples. Lanes are labeled as follows: 1, inoculum; 2, lysate; 3, lysis pellet; 4, protein marker; 5, His-Trap flow-through; 6, Δ19*Tf*NCS eluted from His-Trap chromatography; and 7, Δ19*Tf*NCS further purified by Superdex size-exclusion chromatography. The arrow indicates the Δ19*Tf*NCS band region in the gel.

4.2 Monitoring Reaction Progress by ^{1}H NMR Spectroscopy.

A (*S*)-NCS-catalyzed reaction of dopamine and hexanal to give 1-pentyl-1,2,3,4-tetrahydroisoquinoline-6,7-diol was selected as a model reaction to evaluate the impact of immobilization on (*S*)-NCS performance by determining reaction yields and stereoselectivity. Yields were determined by monitoring the consumption of the limiting reactant dopamine and the formation of 1-pentyl-1,2,3,4-tetrahydroisoquinoline-6,7-diol, by ^{1}H NMR. To this aim, ^{1}H NMR signals whose integrals were directly related to the concentrations of these compounds were identified. The signals of the aromatic ring hydrogens of dopamine are shown in Figure 26. Among them, the dopamine H-4 signal was selected due to the superimposition of product H-3 and dopamine H-5 signals in ^{1}H NMR spectra. As a result, the remaining dopamine concentration after each reaction could be calculated from the integration of dopamine H-4 and DSS (internal standard) signals.

Conversions of (*S*)-NCS-catalyzed reactions have been determined by HPLC in previous studies (Lichman et al., 2017a). ^{1}H NMR monitoring, however, is advantageous because the method provides strong evidence for obtaining the expected product without the need for a product standard and detects and identifies side products.

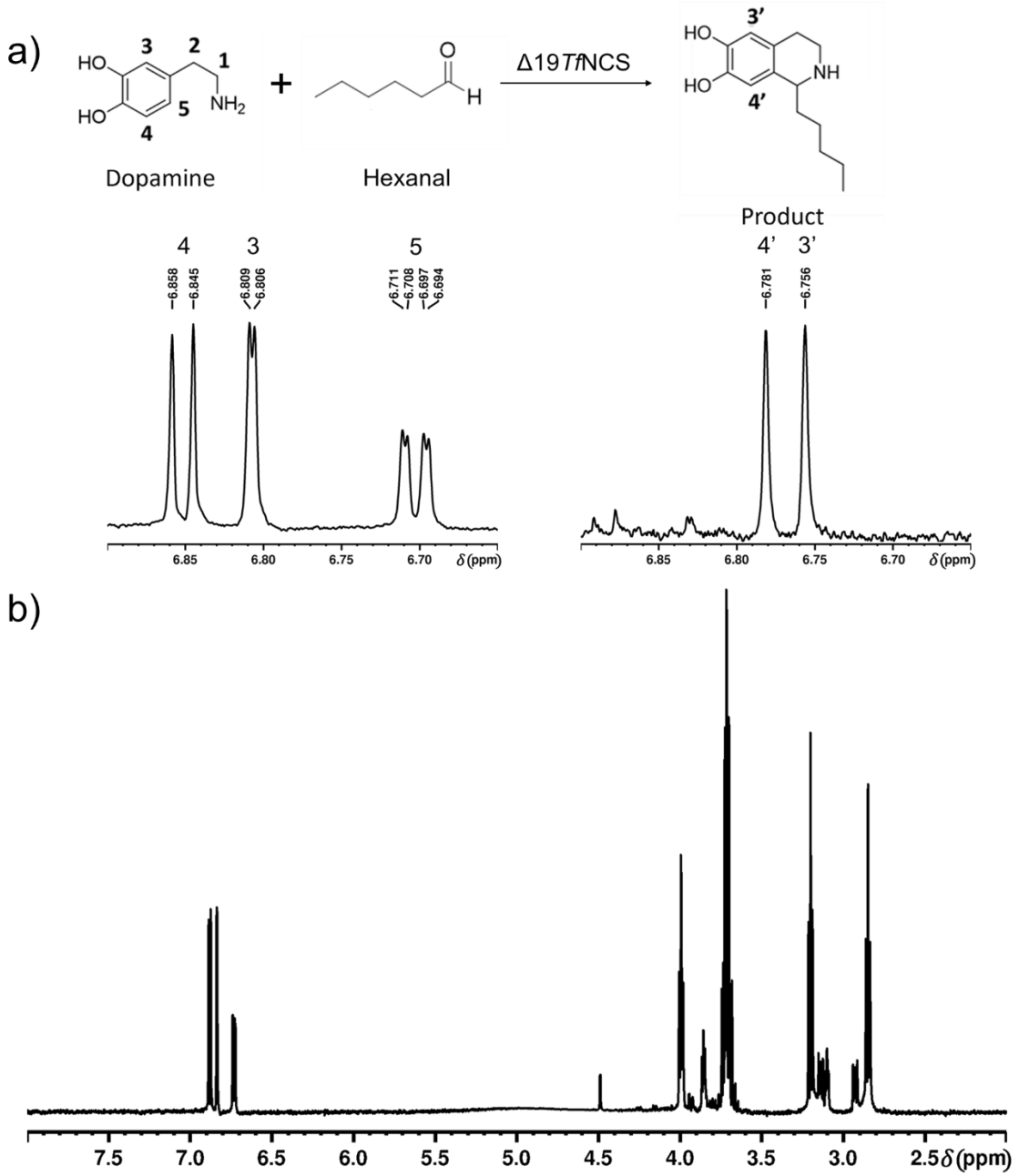

Figure 26. Reaction between dopamine and hexanal to give 1-pentyl-1,2,3,4-tetrahydroisoquinoline-6,7-diol. a) ^{1}H NMR spectrum (ppm) of dopamine (left) and 1-pentyl-1,2,3,4-tetrahydroisoquinoline-6,7-diol (right) zoomed at the aromatic ring region of both spectra. b) Full dopamine ^{1}H NMR spectrum (ppm) - 2.5 mM dopamine in 1 M phosphate buffer (pH 7.0) containing 5 mM ascorbic acid and 10% D_2O (v/v).

4.3 Screening and Selection of Solid Supports for (*S*)-NCS Immobilization

Inertness towards reactants is a crucial feature of a suitable material for enzyme immobilization. Because the Pictet-Spengler reaction has been reported to be catalyzed by acids (Overvoorde et al., 2015; Stöckigt et al., 2011; Vanden Eynden; Kunchithapatham; Stambuli, 2010; Youn, 2006) and phosphate (Ghirga et al., 2016; Salvatti et al., 2024), the ability of a given material

to catalyze this reaction was an important concern, since competition between enzymatic and non-enzymatic, non-enantioselective catalysis could lead to products with low enantiomeric excess. In addition, materials that absorb the reactants and products are also unsuitable for enzyme immobilization since this feature may be detrimental to mass transfer and hamper yield determination and product recovery.

To select suitable supports for (*S*)-NCS immobilization, seven commercial materials: silica gel, Dowex 50WX8, Dowex 50WX4, Dowex 1X8, Diaion HP-2MG, Kaolin, and Celite 545 (Table 4) were screened for their ability to adsorb dopamine and hexanal and catalyze the Pictet-Spengler reaction (Figure 27).

Table 4. Physical and Chemical Properties of Solid Supports Used in (*S*)-NCS immobilization.

Support	Properties
Silica gel (Sigma Aldrich)	Average pore size: 60 Å Granulometry: 230-400 Mesh
Dowex 1X8 (Dow Chemicals)	Basic anion resin (Cl^-) Co-polymeric material: styrene (92%) and divinylbenzene (8%) Granulometry: 200-400 Mesh
Dowex 50WX8 (Dow Chemicals)	Acid cation resin (H^+) Co-polymeric material: styrene (92%) and divinylbenzene (8%) Granulometry: 100-200 Mesh
Dowex 50WX4 (Dow Chemicals)	Acid cation resin (H^+) Co-polymeric material: styrene (96%) and divinylbenzene (4%) Granulometry: 100-200 Mesh
Kaolin (Química Moderna)	Material: aluminum silicate hydroxide $Al_2Si_2O_5(OH)_4$
Diaion HP-2MG (Sigma Aldrich)	Material: Polymethacrylate Granulometry: 25-50 Mesh Average pore size: 170 Å
Celite 545 (Fisher Scientific)	Material: Diatomaceous earth Granulometry: 0.02-0.1 mm

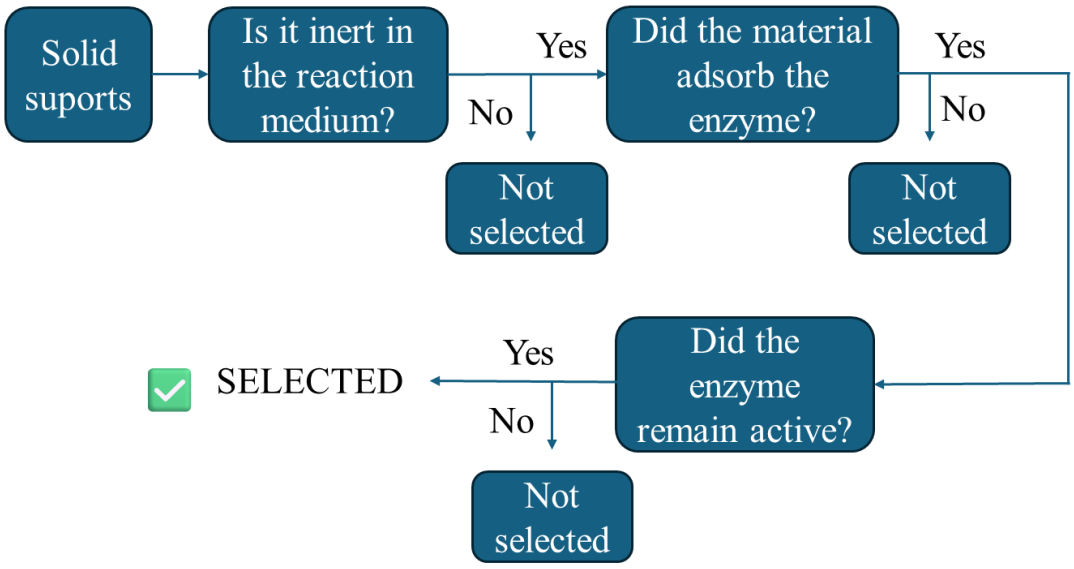

Figure 27. Organogram outlining the criteria for material selection.

No ^{1}H NMR signals of the reaction product were observed, ruling out the catalytic activity of all matrices. However, the adsorption of hexanal by silica gel was confirmed by the disappearance of the formyl hydrogen signal in ^{1}H NMR spectra, indicated by the red arrow in Figure 28a. In contrast, dopamine adsorption was observed for Dowex 50WX8 and Dowex 50WX4, indicated by the blue arrow in Figures 28b and 28c, likely due to ionic interactions with dopaminium cations. These findings excluded silica gel, Dowex 50WX-8, and Dowex 50WX-4 from further experimentation.

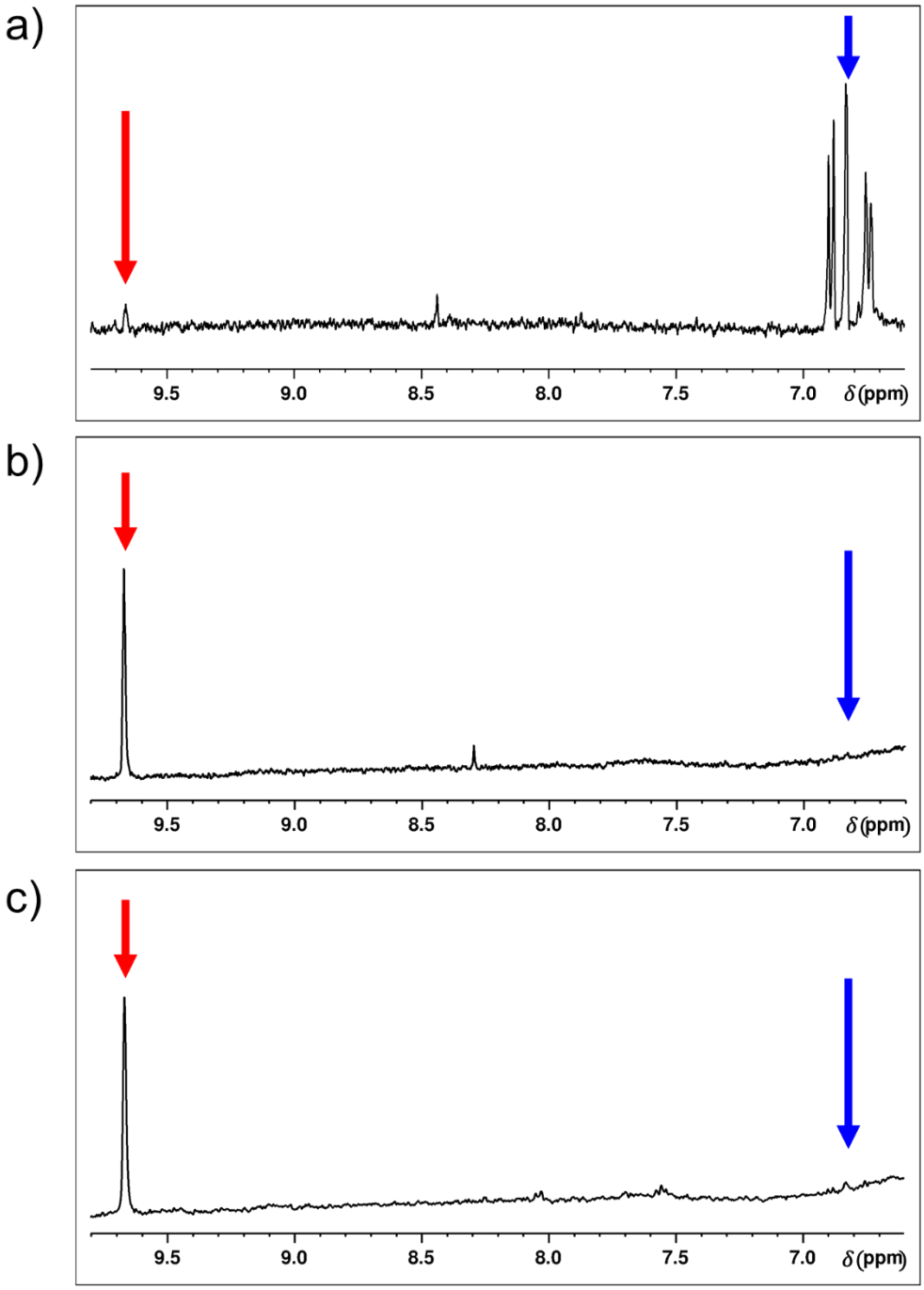

Figure 28. ^{1}H NMR spectrum (400 MHz, 298 K) of a sample containing 2.5 mM dopamine and 2.5 mM hexanal with a) silica gel b) Dowex 50WX8 and c) Dowex 50WX8 (all of them without immobilized Δ19*Tf*NCS) in 50 mM HEPES buffer (pH 7.0), 5 mM ascorbic acid, and 10% D_2O (v/v). The red arrow indicates the formyl hydrogen signal region, and the blue arrow indicates the region of the aromatic hydrogens from dopamine.

Kaolin, Celite 545, Dowex 1X8, and Diaion HP-2MG were evaluated for the immobilization of (S)-NCS. Diaion HP-2MG and Kaolin achieved the highest immobilization yields (99% and 91%, respectively), followed by Celite 545 (76%) and Dowex 1X8 (51%) (Figure 29).

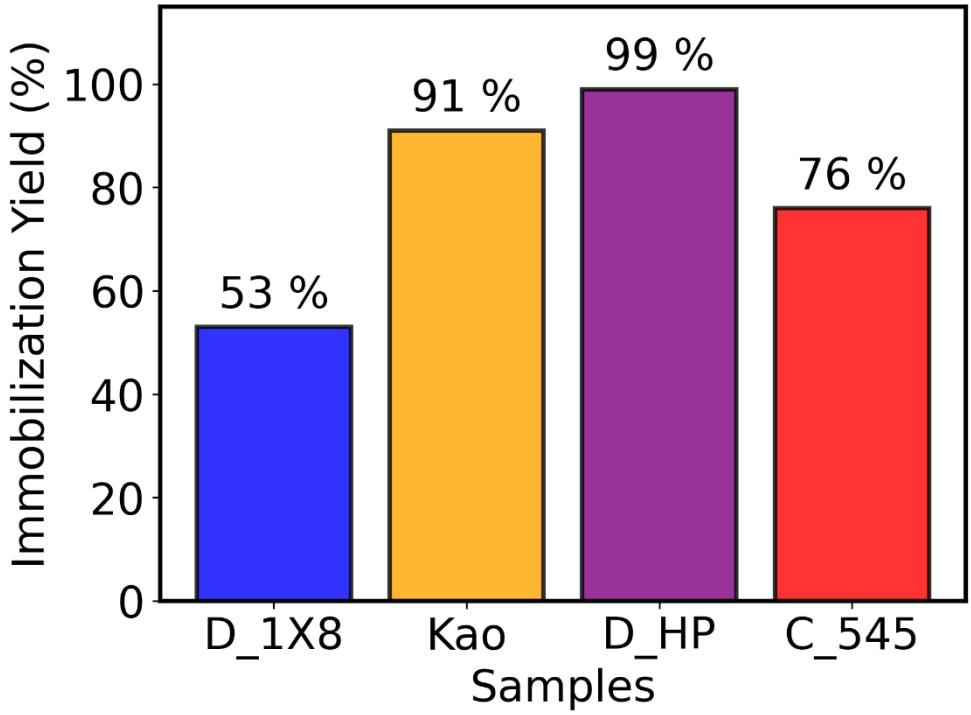

Figure 29. Immobilization yield of (*S*)-NCS on four inert matrices: Dowex 1X8 (D_1X8), Kaolin (Kao), Diaion HP-2MG (D_HP), and Celite 545 (C_545).

Among all the tested supports, Diaion HP-2MG exhibited the highest immobilization yield, followed by Celite 545, Ni-NTA, Kaolin, and finally Dowex 1 (Dowex 1X8). Diaion HP-2MG is an adsorbent composed of polymethacrylate containing ester groups. With an average pore size of 170 Å, it allows the diffusion of large molecules such as the Δ19*Tf*NCS enzyme into its porous structure, a favorable feature for adsorption-based processes and, consequently, for protein immobilization. This characteristic is reflected in the remarkably high immobilization yield observed for Δ19*Tf*NCS (99%).

This support has previously been used not only for enzyme adsorption but also for the immobilization of whole cells. A notable example can be found in the study by Lechner et al. (2018), which involved the immobilization of *E. coli* cells expressing (*S*)-NCS. In that work, Diaion HP-2MG was added directly to the *E. coli* BL21 (DE3) culture medium during IPTG induction, leading to the formation of a biofilm composed of *E. coli* cells expressing (*S*)-NCS on the surface of the support (Lechner et al., 2018).

Finally, catalytic performance was assessed by monitoring the reaction between dopamine and hexanal (Figure 30).

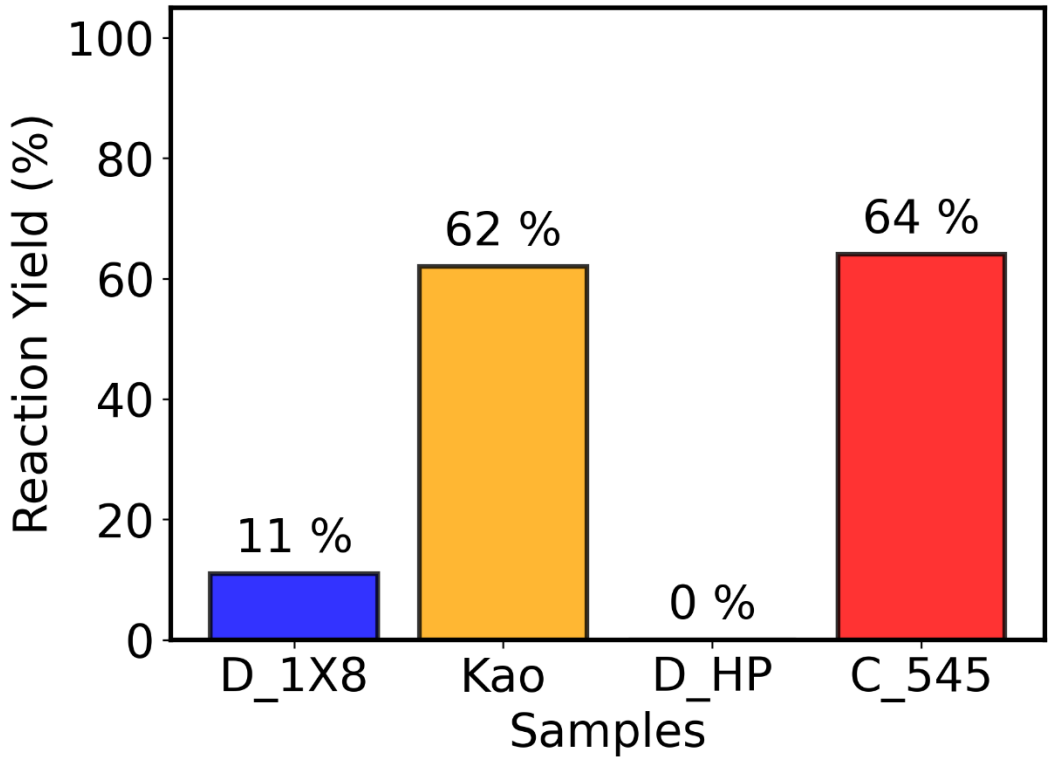

Figure 30. Reaction yield of immobilized enzyme samples for solid support selection. Matrices: Dowex 1X8 (D_1X8), Kaolin (Kao), Diaion HP-2MG (D_HP), and Celite 545 (C_545).

By comparing the reaction yields obtained for the immobilized Δ19*Tf*NCS on different support matrices with their respective immobilization yields (Figure 28), a direct correlation can be observed in most cases: the higher the immobilization yield, the greater the reaction yield. This trend suggests that, for most of the materials tested, the catalytic efficiency of the immobilized biocatalyst is primarily determined by the support's ability to retain Δ19*Tf*NCS.

An important exception to this pattern is the Diaion HP-2MG support. Despite exhibiting the highest immobilization yield among all tested matrices (99%), it resulted in the lowest catalytic activity. Several factors may account for this discrepancy. One possibility is partial enzyme inactivation upon adsorption to the hydrophobic surface of Diaion HP-2MG, potentially caused by protein unfolding. Another plausible explanation involves unfavorable enzyme orientation: Δ19*Tf*NCS may adsorb with its hydrophobic cavity, the active site, facing the matrix surface, thereby restricting substrate access (Guisan et al., 2020). Additionally, significant enzyme leaching during the washing and reaction steps cannot be ruled out, which would reduce the amount of active enzyme retained on the support and contribute to the observed low reaction yield.

In summary, immobilization on Diaion HP-2MG completely inhibited enzyme activity, and poor yields were observed for Dowex 1X8. In contrast, (S)-NCS immobilized on Celite 545 and Kaolin showed the highest reaction yields (64% and 62%, respectively). Therefore, Celite 545 and Kaolin were chosen for further studies.

4.4 Optimization of Immobilization Conditions for (*S*)-NCS on Kaolin and Celite 545

Immobilization was performed by mixing (*S*)-NCS with Kaolin or Celite 545 under varying enzyme concentrations and support masses, resulting in different initial protein/support mass ratios. Figure 31 presents the (S)-NCS immobilization yield values.

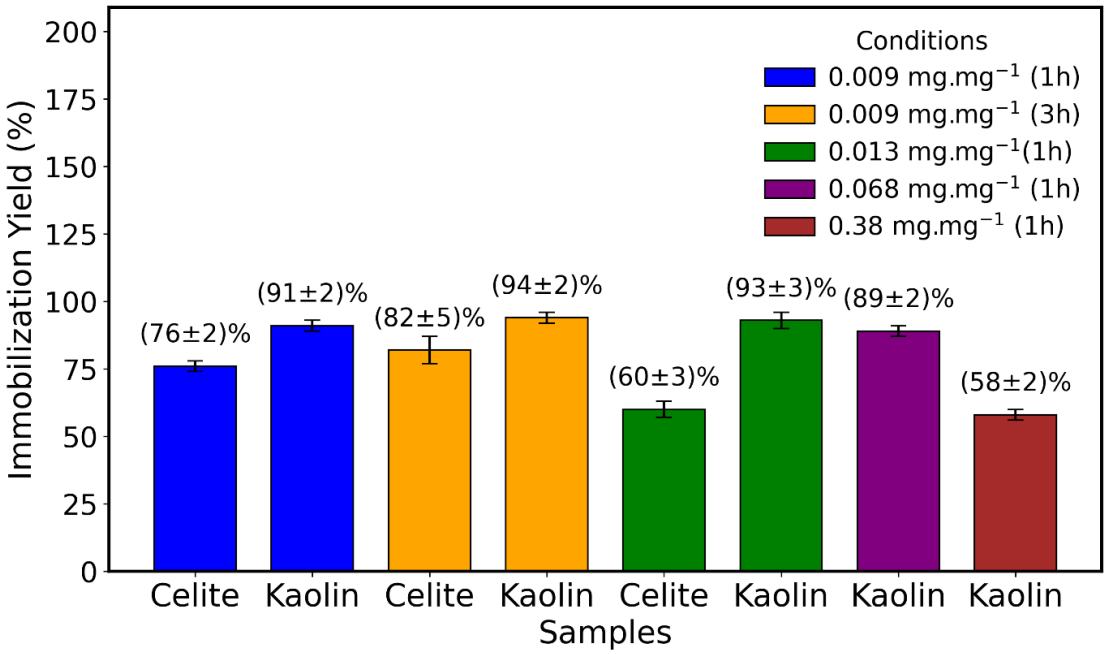

Figure 31. Immobilization yield of Δ19*Tf*NCS in the Kaolin and Celite 545 at different conditions. The immobilization media were homogenized for 1 hour or 3 hours at approximately 25 °C.

Kaolin consistently showed a higher immobilization capacity for (*S*)-NCS than Celite 545. Increasing the protein/support mass ratio from 0.009 to 0.013 reduced the immobilization yield of Celite 545, indicating saturation of active sites of this material; therefore, higher enzyme concentrations were not tested. In contrast, yields around 90% were maintained for Kaolin across protein /support ratios up to 0.067, with immobilization decrease 58 (± 2) % being observed only at a ratio of 0.38. The difference in immobilization efficiencies between kaolin and celite 545 will be better discussed, based on material characterizations, in Section 4.9.

Furthermore, varying the immobilization time from 1 to 3 hours did not significantly impact yields, confirming that 1 hour is sufficient. Based on these observations, a final protocol for Δ19*Tf*NCS immobilization on these materials was defined, which is reported in section 1.3 of this chapter.

4.5 Initial Reaction Performance: Free vs. Immobilized Enzyme at 37°C.

Reusability of immobilized Δ19*Tf*NCS samples was monitored by performing the biocatalyzed Pictet-Spengler reaction three times (Figure 32). The immobilized (*S*)-NCS preserved its catalytic performance over these experiments. Catalytic activity tends to decrease after enzyme immobilization; however, this decrease can be compensated by an increment in stability and ease of reuse, among other benefits, so that the use of the immobilizated biocatalyst becomes advantageous compared to the use of the free enzyme (Guisan et al., 2020).

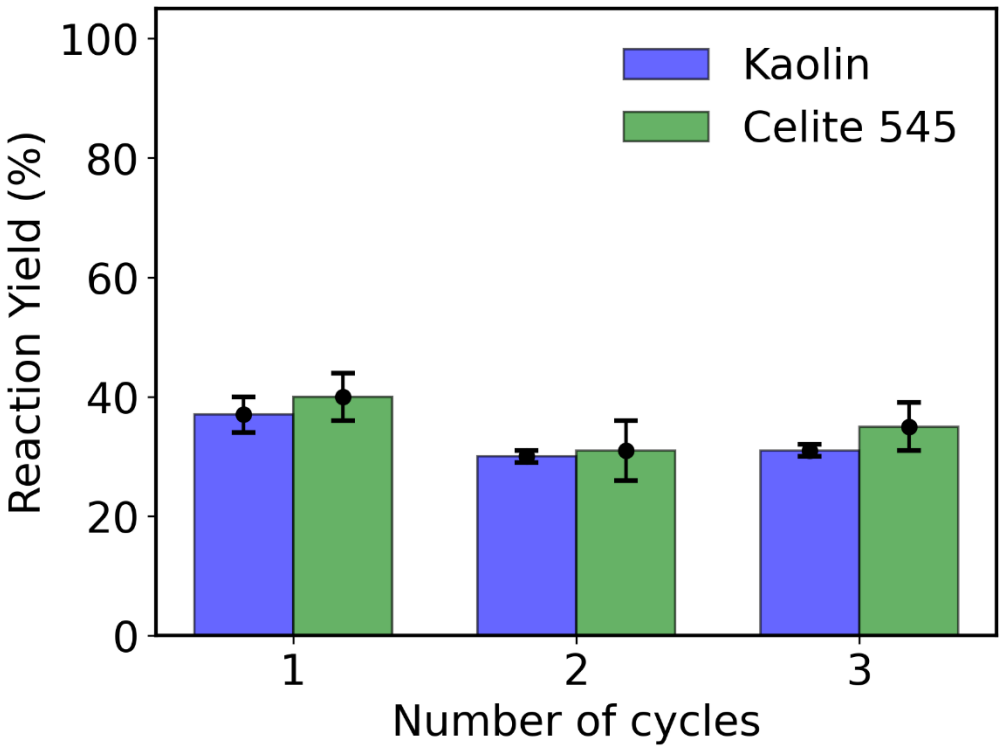

Figure 32. Reusability of Kaolin- and Celite 545-immobilized Δ19*Tf*NCS over three consecutive reaction cycles. Reactions were performed at 37°C for 1 h using the following conditions: 0.25 mM dopamine, 2.5 mM hexanal, 5 mM ascorbic acid, 0.05 mg·mL^{-1} enzyme, 50 mM HEPES buffer (pH 7), 100 mM NaCl, and 10% (v/v) DMSO.

The sample containing free Δ19*Tf*NCS exhibited, as expected, the highest reaction yield. This result is consistent with the literature, which commonly reports a decrease in the apparent activity of enzymes after immobilization, especially when factors such as limited diffusion,

structural inactivation, or unfavorable enzyme orientation on the support are present. Nevertheless, immobilization can be advantageous when accompanied by gains in thermal stability, resistance to organic solvents, and reusability, key factors that economically enable the industrial use of biocatalysts. (Guisan et al., 2020).

According to Wang et al. (2025), the catalytic activity of immobilized enzymatic systems is often limited by mass transfer processes, which occur on both macroscopic (mixing and fluid flow) and microscopic (external and internal diffusion into the support) scales. In the specific case of enzymes immobilized on porous materials such as kaolin and Celite, internal diffusion limitations represent one of the main factors reducing catalytic efficiency, hindering both the access of substrates to the active site and the release of products (Wang et al., 2025).

Moreover, even when using standardized protocols, the final concentration of active enzyme in immobilized systems may be lower than expected due to losses during the immobilization and washing steps. The interaction between the enzyme and support must strike a balance between conformational stability and catalytic accessibility, which does not always occur. Highly hydrophobic support, which is not the case with kaolin and celite, may promote enzyme binding with the active site facing the support surface, impairing catalysis. Additionally, the formation of aggregates or partial denaturation of the protein during adsorption can also contribute to enzymatic inactivation (Wang et al., 2025).

Nonetheless, it was observed that both kaolin and Celite 545 biocatalysts, used in this study, exhibited similar behavior over three usage cycles, with low variation on reaction yield values after the first reuse (Figure 32). This suggests that, although the systems present initial limitations, both show potential for application in continuous or batch processes with reuse. Further optimization is still possible, such as support functionalization to enable covalent binding immobilization strategies (De Souza Lima et al., 2022; Fai et al., 2017; Wang et al., 2025).

Additionally, it is important to note that in all cases, there were no detectable conversions in the control samples, indicating the absence of background reactions.

4.6 Temperature Effects on Free and Immobilized (*S*)-NCS Activity

The temperature-dependent activity profiles (Figure 33) reveal that while the free Δ19*Tf*NCS enzyme shows a sharp decline in reaction yield with increasing temperature (from 37 °C to 57 °C), a typical behavior associated with thermal denaturation and aggregation, both

immobilized samples exhibit increased activity up to 47 °C, indicating a significant improvement in thermostability. This fundamental difference can be attributed to the stabilizing effects conferred by immobilization, such as restricted conformational mobility, prevention of unfolding, and the formation of stabilizing interactions with the solid support surface, which help maintain the structural and functional integrity of the enzyme under conditions that would normally promote its inactivation (Ariaeenejad; Motamedi, 2025; Klibanov, 1979).

Furthermore, enzymatic thermostability is influenced not only by resistance to denaturation but also by the preservation of the active site architecture at elevated temperatures, which critically depends on the conformational rigidity imposed by immobilization (Punekar, 2025).

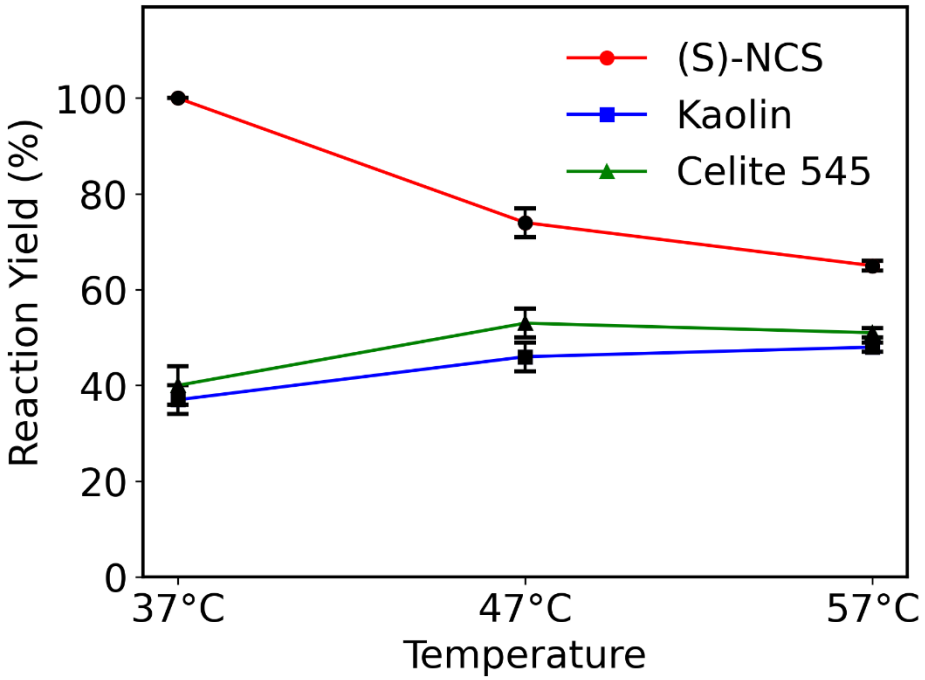

Figure 33. Temperature profile of the reaction at 37°C, 47°C, and 57°C. Reactions were performed at 37°C for 1 h using the following conditions: 0.25 mM dopamine, 2.5 mM hexanal, 5 mM ascorbic acid, 0.05 mg·mL^{-1} enzyme, 50 mM HEPES buffer (pH 7), 100 mM NaCl, and 10% (v/v) DMSO.

Another relevant factor is the effect of temperature on mass transfer processes. Increasing the temperature enhances the diffusion of both substrates and products, as the diffusion coefficient is directly proportional to temperature. This is particularly important for enzymes immobilized on porous supports such as kaolin and Celite 454, where internal diffusion represents a significant limitation to catalytic activity. Thermal elevation can thus partially mitigate this limitation, favoring the observed reaction rate up to a certain point (Ariaeenejad; Motamedi, 2025; Punekar, 2025).

4.7 Impact of DMSO Concentration on Free and Immobilized (*S*)-NCS Activity

Many of the aldehydes and ketones used as substrates in biocatalytic Pictet–Spengler reactions exhibit low solubility in aqueous media. Therefore, the addition of a water-miscible organic cosolvent, such as dimethyl sulfoxide (DMSO), becomes necessary to enable the reaction (Lichman et al., 2017a). However, the presence of DMSO can compromise the structural stability of non-immobilized enzymes, resulting in reduced reaction yields.

The data presented in Table 5 show the impact of DMSO concentration (10% and 20% v/v) on the reaction catalyzed by free Δ19*Tf*NCS and the enzyme immobilized on Kaolin or Celite 545. While the non-immobilized enzyme experienced a significant drop in yield, from 100% to 56±4%, the enzyme immobilized on Celite 545 also showed a decrease, although less pronounced (from 40±4% to 28±3%). In contrast, the enzyme immobilized on Kaolin demonstrated remarkable stability, maintaining consistent yields (37±3% and 35±3%) even in the presence of 20% DMSO.

Table 5. Yields of biocatalytic Pictet-Spengler reactions performed in HEPES buffer with 10% and 20% (v/v) DMSO concentration.

Sample	Reaction yield at 10% v/v DMSO	Reaction yield at 20% v/v DMSO
non-immobilized enzyme	100%	56±4%
Kaolin	37±3%	35±3%
Celite 545	40±4%	28±3%

This behavior can be explained based on classical studies on enzyme stabilization through immobilization. According to Klibanov (1979), immobilization provides two important protective mechanisms against denaturation by organic solvents: (i) an increase in the conformational rigidity of the enzyme, preventing unfolding caused by the cosolvent, and (ii) the creation of a protective microenvironment around the enzyme, in which the effective concentration of DMSO is lower than in the bulk reaction medium (Klibanov, 1979).

Another factor to consider is the role of immobilization on porous supports as a physical barrier against protein aggregation, which is often triggered by organic solvents. This structural protection prevents enzyme denaturation due to DMSO-induced aggregation (Guisan et al., 2020).

Therefore, the results observed in this study highlight Kaolin as a promising support for (*S*)-NCS applications under reaction conditions requiring high DMSO content. This feature is particularly valuable for the synthesis of benzylisoquinoline alkaloids derived from hydrophobic substrates, thereby reinforcing the system's potential for sustainable industrial applications.

4.8 Stereoselectivity of Free and Immobilized (*S*)-NCS in the Pictet-Spengler Reaction.

One of the most important advantages of enzymes over traditional catalysts is their ability to catalyze chemical reactions with high stereoselectivity. To investigate the effect of immobilization of (*S*)-NCS on Kaolin and Celite 545 on stereoselectivity, Chiral HPLC was used to qualitatively assess the enantiomeric excess of the tetrahydroisoquinoline produced by the Pictet-Spengler reaction between dopamine and hexanal. The non-enzymatic Pictet-Spengler reaction produced a racemic mixture, as evidenced by two peaks of similar intensity at retention times (rt) of approximately 34 min and 36 min (Figure 34a). In contrast, the enzymatic Pictet-Spengler reaction catalyzed by non-immobilized (*S*)-NCS showed high stereoselectivity, with a significantly more pronounced peak at 34 min than at 36 min (Figure 34b). Despite a slight loss in stereoselectivity of immobilized enzymes, a similar chromatographic profile was observed for reactions catalyzed by (*S*)-NCS immobilized on both Kaolin (Figure 34c) and Celite 545 (Figure 34d), confirming that the enzyme retains most of its stereoselectivity after immobilization.

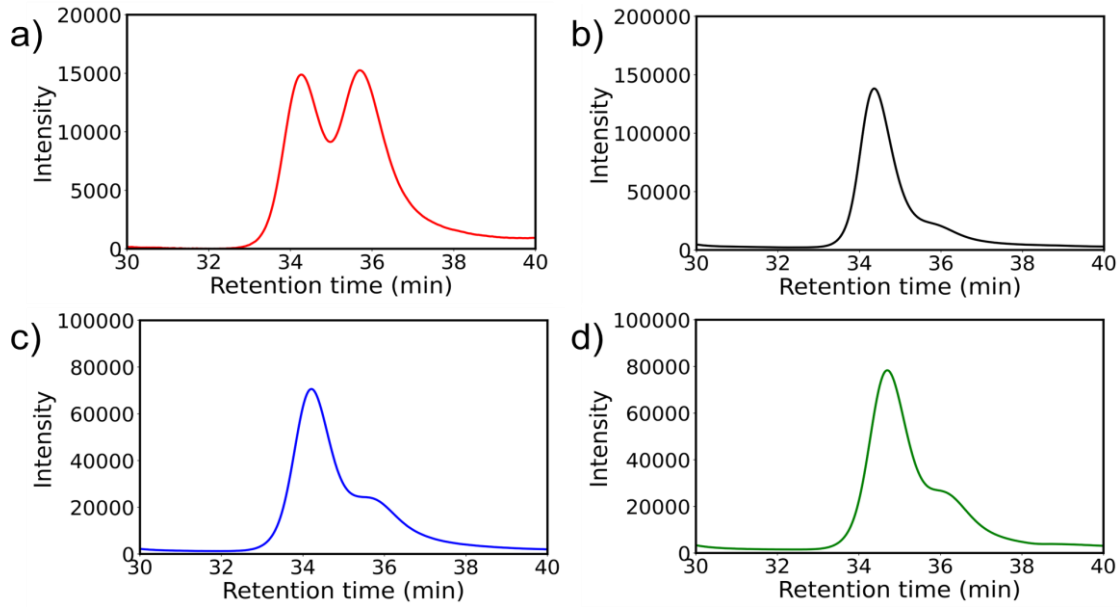

Figure 34. Chiral HPLC chromatograms expanded in the product detection region: **a)** Non-enzymatic Pictet-Spengler reaction catalyzed by phosphate buffer (reaction media - 1:1 AcCN: potassium phosphate buffer 100 mM, pH 6.0) at 50°C for 12 h. **b)** Reaction catalyzed by free (*S*)-NCS. **c)** Reaction catalyzed by (*S*)-NCS immobilized on Kaolin. **d)** Reaction catalyzed by (*S*)-NCS immobilized on Celite 545.

4.9 Surface Properties of Kaolin and Celite 545

To investigate the causes of higher (*S*)-NCS adsorption in Kaolin than in Celite 545, the matrix surfaces were characterized using N_2 sorption/desorption isotherms and zeta potential (zP) measurements. Figure 35 displays the N_2 sorption/desorption isotherms for Kaolin and Celite 545. Both materials exhibited hysteresis in their isotherms, indicating the presence of mesopores. Using the BJH method to calculate pore diameter distribution (Table 6), the average pore diameters for both materials fell within the mesoporous range. These mesopores can facilitate the adsorption of (*S*)-NCS within the pores, potentially enhancing the stability of the enzyme. This stabilization may result from two factors: (1) reduced enzyme exposure to the reaction medium, thereby minimizing interactions with air bubbles formed during stirring, and (2) decreased enzyme-enzyme interactions, which prevent aggregation (Guisan et al., 2020). This feature aligns with the data in Table 5, which shows that the reaction yield for (*S*)-NCS immobilized on Kaolin remains stable at both 10% and 20% v/v DMSO concentrations, whereas the yield for the free enzyme drops by half at a 20% v/v DMSO concentration. The BET method was also used to calculate surface areas and other properties from the sorption isotherms (Table 6).

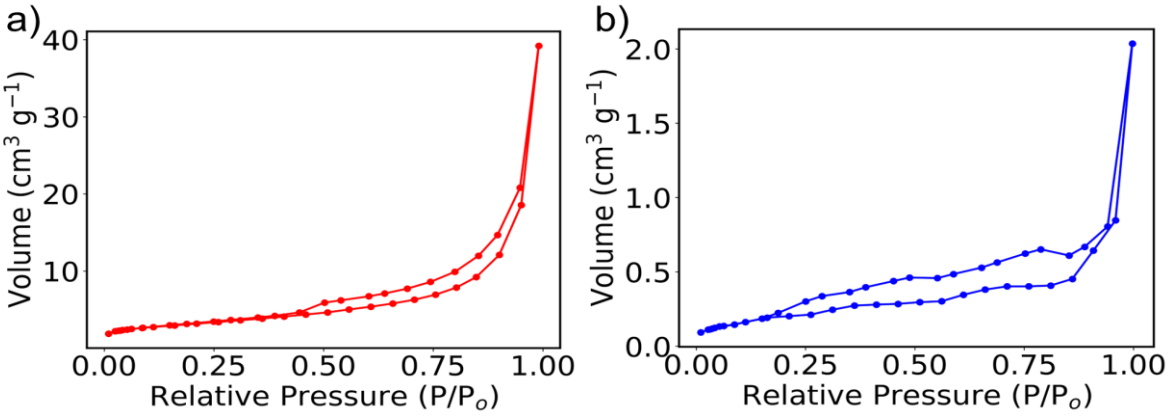

Figure 35. N_2 sorption/desorption isotherms for (a) Kaolin and (b) Celite 545. The N_2 adsorption and desorption measurements were performed on the Autosorb 1 equipment (Quantachrome, USA) at 77 K.

Table 6. The surface properties of materials are calculated through sorption isotherms.

Samples	Surface area B.E.T (m^2/g)	Total volume (cm^3/g)	Mesopore area (m^2/g)	Mesopore volume (cm^3/g)
Kaolin	11.063	6.062×10^{-2}	8.687	0.059
Celite 545	0.756	3.148×10^{-3}	0.341	0.003

Kaolin exhibited a significantly higher surface area (11.063 m²/g) than Celite 545 (0.756 m²/g), which correlates with its superior immobilization capacity (session 2.1 – Chapter 3). This suggests that Kaolin provides a larger surface area for enzyme-adsorbent interactions. To further investigate the immobilization mechanism, zeta potential (zP) measurements were conducted for both pure and enzyme-immobilized materials suspended in 50 mM HEPES and 100 mM NaCl (pH 7) (Table 7). The zeta potential of pure Kaolin (-36.3 mV) was more negative than that of Celite 545 (-15.4 mV). After immobilization, both materials exhibited a decrease in absolute zeta potential values, with kaolin showing a more pronounced change ($\Delta zP = 25$ mV) than Celite 545 ($\Delta zP = 6$ mV). This more significant change in zeta potential for Kaolin reflects its higher enzyme loading capacity, which is consistent with its greater surface area.

Table 7. Effect of enzyme immobilization on the zeta potential of Kaolin and Celite 545.

Sample	Zeta-Potential / mV
Kaolin	-36 ± 1
Kaolin + (*S*)-NCS	-11 ± 1
Celite 545	-15 ± 1
Celite 545 + (*S*)-NCS	-9 ± 2

It is important to consider that the theoretical isoelectric point (pI) of Δ19*Tf*NCS, calculated using the ExPASy ProtParam tool (see Appendix), is 6.07. Therefore, under the immobilization conditions employed (pH 7), the enzyme carries a net negative charge. As such, electrostatic interaction with the negatively charged surface of the support materials would only be possible through localized regions of positive charge on the protein. In this context, a theoretical study was conducted to investigate the electrostatic interaction mechanisms between the protein and the surface of the most prominent support material, kaolin.

4.10 Characterization of (*S*)-NCS Adsorption Interactions Using Coarse-Grained Monte Carlo Simulations

To elucidate the molecular basis of (*S*)-NCS immobilization on Kaolin, we performed coarse-grained simulations probing electrostatic interactions between the enzyme and the negatively charged Kaolin pores surface. This approach complements experimental data by resolving orientation-specific binding energetics inaccessible to bulk techniques.

Molecular simulations revealed that (*S*)-NCS strongly adsorbs to the Kaolin surface at pH 7, primarily through electrostatic interactions between the negatively charged surface and the positively charged N-terminal His-tag (Figure 36). Probability distributions of the five closest titratable residues (His-6, His-7, His-8, His-10, and Arg-17) confirmed their dominant role in binding, while downstream residues (Lys-46 and His-49) remained distal from the interface.

The simulations revealed that (*S*)-NCS remains adsorbed on the Kaolin surface, with no unfolding of the structured portion upon adsorption. The adsorption was energetically favorable, with an average binding energy of (−3.54 ± 3.63) k_BT derived from 10^6 sampled configurations. Desorption events were observed, although at a much lower frequency than adsorption events, indicating stable binding and effective sampling of the configurational space. This interaction was critically dependent on the His-tag: removing this sequence would invert the protein's net charge to −4e, abolishing the observed adsorption behavior. The simulations thus demonstrate that the disordered, histidine-rich N-terminus mediates the affinity and orientation of (*S*)-NCS on Kaolin.

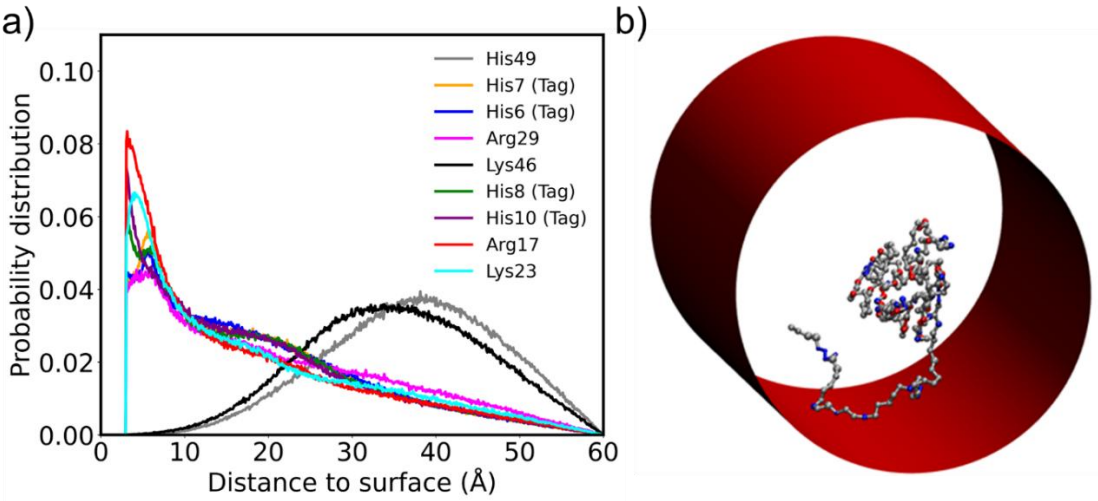

Figure 36. Protein orientation during adsorption. **a)** Probability distribution of the nine closest titratable residues (His10, His8, Arg17, Arg29, His49, Lys23, Lys46, His7, and His6) and the first two residues outside the disordered sequence (Lys-46 and His-49) as a function of their distance to the surface. **b)** Snapshot of (*S*)-NCS adsorbed on the kaolin surface, highlighting positively charged (blue) and negatively charged (red) residues at pH 7. The amino acid residues are numbered according to the Δ19*Tf*NCS sequence, which includes all residues preceding the thrombin cleavage site (this sequence is provided in the supporting information).

These results provide detailed insights into the immobilization mechanism of (*S*)-NCS on Kaolin. The electrostatic attraction between the positively charged N-terminal sequence and the negatively charged Kaolin surface is a key driver of protein adsorption. This is consistent with the experimental zeta potential values: kaolin (-36 ± 1 mV) exhibited a stronger affinity for (*S*)-NCS than Celite 545 (-16 ± 3 mV), as the higher negative charge of Kaolin enhances binding with the positively charged N-terminal sequence.

5. DISCUSSION

Enzyme immobilization is widely used to enhance stability, reusability, and applicability of biocatalysts in industrial processes. Among the various immobilization techniques, such as adsorption, covalent attachment (including single- and multi-point strategies) (Weltz et al., 2020), affinity binding (Hamzah; Nasir; Hamzah, 2014), and encapsulation (Shen et al., 2011), adsorption stands out for its simplicity and cost-effectiveness.

In this work, methodologies were developed to immobilize the enzyme (*S*)-NCS on cost-effective materials and investigate its adsorption mechanisms. To achieve this, a robust protocol was first established to monitor the Pictet-Spengler reaction catalyzed by (S)-NCS using ^{1}H NMR spectroscopy. Then, various materials were screened for their ability to immobilize this enzyme based on the following criteria: (i) chemical inertness to the reaction, avoiding interference with substrates or products, and (ii) efficient adsorption while preserving the enzyme's structure and activity. Under various experimental conditions, the performance of (S)-NCS immobilized on Kaolin and Celite 545, the most promising adsorbents, was further evaluated. These analyses focused on three critical parameters: reusability across multiple reaction cycles, stability under elevated temperatures and high DMSO concentrations, and preservation of enantioselectivity in the Pictet-Spengler reaction between dopamine and aldehydes.

The immobilization yield experiments revealed significant differences in the adsorption capacities of kaolin and Celite 545. Kaolin exhibited superior immobilization efficiency, maintaining high yields across a wide range of enzyme concentrations (up to 7.5 mg/mL). In contrast, Celite 545 showed a marked decrease in yield (from 76 ± 2% to 60 ± 3%) as the protein/support mass ratio increased from 0.009 to 0.013 mg/mg. This decline suggests saturation of Celite 545's active sites, limiting its utility at higher enzyme concentrations. In contrast, Kaolin's robust performance can be attributed to its significantly larger surface area (11.063 m^2/g vs. 0.756 m^2/g for Celite 545) and more negative zeta potential (-36.3 mV vs. -15.4 mV), which facilitates stronger electrostatic interactions with the positively charged N-terminal region of (*S*)-NCS.

The catalytic performance of immobilized (*S*)-NCS was evaluated under various conditions, including temperature increase, addition of DMSO, and reuse. Although immobilization often leads to a reduction in enzymatic activity due to factors such as diffusion limitations, structural alterations, and partial enzyme inactivation, the obtained results demonstrate that

immobilization on Kaolin and Celite 545 effectively preserves the catalytic functionality of (*S*)-NCS (Figures 30-34), while improving its thermo- and chemo stability. The observed decrease in enzymatic activity following immobilization can be attributed to both intrinsic factors, such as conformational changes or altered enzyme dynamics, and microenvironmental factors, including the porosity of the support material (Guisan et al., 2020). A critical consideration is the role of diffusion limitations, which impact the transport of reactants to the enzyme's active site and the subsequent release of products into the reaction medium.

As a result, the measured enzymatic activity reflects the "apparent" or "effective activity" (Guisan et al., 2020) of the entire immobilized system, rather than the intrinsic activity of the enzyme alone. This distinction is crucial for interpreting the performance of immobilized enzymes, as diffusion constraints can mask the true catalytic potential of the enzyme. The influence of diffusion limitations is further supported by the increased enzyme activity at elevated temperatures, where enhanced diffusion rates mitigate these constraints, leading to improved reaction yields.

When comparing the performance of the immobilized enzyme, both Kaolin and Celite 545 exhibited similar reaction yields over three consecutive uses. The yields for each support were virtually identical, and when considering the error ranges provided by the standard deviations, no statistically significant difference in performance could be attributed to either material. This similarity suggests that the factors contributing to reducing effective enzymatic activity, such as diffusion limitations, structural alterations, or microenvironmental effects, are comparable for both supports.

The immobilized enzymes retained significant activity over multiple reaction cycles, with Kaolin showing superior long-term stability and reusability compared to Celite 545 (Figure 32). This enhanced stability is particularly advantageous for industrial applications that require the repeated use of biocatalysts.

Temperature profile experiments revealed distinct behaviors between free and immobilized (*S*)-NCS (Figure 33). Lower yields with increasing temperature were observed for reactions catalyzed by the free enzyme, likely due to thermal denaturation and aggregation. In contrast, the immobilized enzymes demonstrated improved yields at elevated temperatures (37°C to 47°C), indicating that immobilization enhances thermal stability. This result can be attributed to three key factors considering the enzyme-support system: (1) The direct relationship between increased temperature and increased reaction rate (Punekar, 2025) (2) the increased diffusion

coefficient and corresponding diffusion rates of reactants and products within the support matrix at higher temperatures (Wang et al., 2025), and (3) the structural stabilization of Δ19*Tf*NCS provided by immobilization, which mitigates or prevents enzyme inactivation at elevated temperatures (Ariaeenejad; Motamedi, 2025; Klibanov, 1979). These factors explain the increased reaction yield for immobilized Δ19*Tf*NCS under higher temperature conditions.

The impact of DMSO concentration on enzyme activity further underscored the advantages of immobilization. While the free enzyme and Δ19*Tf*NCS immobilized on Celite 545 exhibited a significant drop in reaction yield at higher DMSO concentrations, the Kaolin-immobilized enzyme maintained catalytic performance. This improved stability is likely due to the protective microenvironment provided by Kaolin, which shields the enzyme from the destabilizing effects of organic solvents (Klibanov, 1979). This property is particularly valuable for reactions involving poorly water-soluble substrates, such as hexanal, where high DMSO concentrations are often required. Furthermore, tolerance to organic solvents usually allows for higher substrate loadings, thus facilitating process intensification, which is crucial for developing cost-effective industrial processes.

Chiral HPLC analysis confirmed that both Kaolin and Celite 545 maintained the high stereoselectivity of Δ19*Tf*NCS in the Pictet-Spengler reaction, with only a slight reduction in enantioselectivity compared to the free enzyme. Lechner and co-workers reported a similar trend after affinity-based immobilization of (*S*)-NCS onto EziG supports (Lechner et al., 2018). This finding highlights the potential of Kaolin and Celite 545 as support for biocatalytic enantioselective reactions, in which preserving stereoselectivity is paramount.

Different approaches to studying protein-material surface interaction have recently been developed. Caetano and co-workers (Caetano et al., 2021) studied the adsorption of hen egg-white Lysozyme (HEWL) into a charged confining pore of negatively charged silica using a coarse-grained and constant-pH Monte Carlo simulation. The protein's preferred orientations toward the charged surface were evaluated, and the most important residues for the interaction were identified. They also analyzed the effect of changing the pH, the salt concentration, and the porous size distribution on the (HEWL) interaction.

Coarse-grained Monte Carlo simulations were employed to provide molecular-level insights into the experimental findings to investigate the molecular interactions between (*S*)-NCS and Kaolin at pH 7.4. The simulations were performed using a Cα-based coarse-grained model, where each amino acid was represented by a single bead centered at the Cα atom (Caetano et

al., 2021; Clementi; Nymeyer; Onuchic, 2000; Contessoto et al., 2016; De Oliveira et al., 2020; Koga; Takada, 2001; Whitford et al., 2009). The Kaolin surface was modeled as a negatively charged cylindrical pore, with its surface density charge of σ = -0.3 C/m^2 and radius α = 6 nm, according to experimental values from references (Palomino; Burns; Santamarina, 2008; Szewczuk-Karpisz et al., 2020). Electrostatic interactions were treated using Debye-Hückel potentials, accounting for the ionic strength of the buffer (100 mM NaCl). The simulations explored over 10^6 protein configurations, providing a statistically robust representation of the adsorption process.

The results revealed that the N-terminal region of (*S*)-NCS, which contains an engineered histidine tag, consisting of a disordered sequence rich in positively charged histidine residues (such as His-6, His-7, His-8, His-10, and Arg-17), plays a critical role in binding to the negatively charged Kaolin surface. The probability distribution of the five closest titratable residues to the surface showed that these residues are primarily responsible for protein-surface binding, with His-10 and His-8 exhibiting the highest binding affinity. In contrast, residues outside this disordered sequence, such as Lys-46 and His-49, remained significantly farther from the surface, as indicated by their probability distribution profiles.

The average binding energy for (*S*)-NCS adsorption on Kaolin was calculated to be (-3.54 ± 3.63) k_BT, indicating a favorable and stable interaction. This value was derived from the electrostatic contributions of all simulated protein configurations. Notably, the simulations revealed a clear preference for adsorbed configurations, with desorbed configurations occurring at a much lower frequency, confirming the strong adsorption affinity of (*S*)-NCS for Kaolin and the conservation of (*S*)-NCS tertiary structure. The preferential orientation of (*S*)-NCS during adsorption, driven by the positively charged N-terminal sequence, ensures that the catalytic site, composed of residues Tyr108, Glu110, Lys122, and Asp141(Ilari et al., 2009; Lichman et al., 2017b; Sheng; Himo, 2019; Zhang et al., 2024), remains accessible to the solvent, preserving enzymatic activity.

These computational analyses align with the experimental zeta potential data, which showed a more pronounced change in absolute zeta potential for Kaolin (ΔzP = 25 mV) compared to Celite 545 (ΔzP = 6 mV), reflecting its higher enzyme loading capacity. The simulations also provide a molecular-level explanation for Kaolin's superior immobilization efficiency, highlighting the critical role of electrostatic interactions in driving protein adsorption.

It is worth noting that, as discussed in the previous section, the net charge of Δ19*Tf*NCS at pH 7 is negative (pI 6.07). However, simulations suggested the presence of a localized positive charge at the N-terminal region of the enzyme under the immobilization conditions. This N-terminal region appears to mediate the interaction with the support surface, while the more structured, negatively charged portion of the protein tends to face the inner part of the pore, likely due to electrostatic repulsion from the surface. This orientation is potentially favorable for the biocatalysis of the Pictet–Spengler reaction.

Integrating experimental and computational methodologies represents a significant advancement toward a deeper comprehension of factors underlying enzyme immobilization. While traditional techniques such as enzyme activity assays, zeta potential measurements, and surface characterization provide valuable insights, combining these with coarse-grained Monte Carlo simulations offers a more detailed understanding of the molecular mechanisms driving immobilization. The simulations identified key residues in the N-terminal region of (*S*)-NCS responsible for binding to Kaolin, providing a molecular-level explanation for the observed experimental trends. This dual approach enhances the understanding of enzyme immobilization and sets the stage for future studies exploring more complex systems and supports.

This study demonstrates the potential of Kaolin and Celite 545 as cost-effective and efficient support for immobilizing (*S*)-NCS. Kaolin offers superior immobilization capacity, thermal stability, and resistance to organic solvents, making it a promising candidate for industrial biocatalysis. The preservation of enantioselectivity and the ability to reuse the immobilized enzyme further underscore the practical advantages of these materials. Integrating experimental and computational approaches provides a robust framework for understanding enzyme-support interactions at a molecular level, paving the way for the rational design of immobilized biocatalysts with enhanced performance and stability.

6 CONCLUSIONS

This study successfully achieved the proposed goal of enhancing the biocatalytic performance of (*S*)-NCS, in terms of thermo-stability, solvent tolerance, reusability and stereoselectivity preservation, which was achieved through the development of a cost-effective immobilization strategy.

The stablished expression and purification protocol of the Δ19*Tf*NCS variant was consistent and reproducible, enabling the downstream immobilization studies. A systematic screening of support materials, identified kaolin and Celite 545 as promising low-cost candidates for physical adsorption, based on criteria such as chemical inertness, adsorption efficiency, and preservation of enzymatic activity. The immobilized biocatalysts were characterized and evaluated, revealing significant enhancements in thermos-stability, operational reusability, and solvent tolerance when compared to the free enzyme. Notably, kaolin outperformed Celite 545 in several key aspects, including immobilization yield, stability at elevated temperatures and DMSO concentrations. These superior properties were attributed to the physicochemical features of kaolin, such as its higher specific surface area and more negative zeta potential, which favored stronger electrostatic interactions with the positively charged N-terminal region of the enzyme. Additionally, both kaolin- and Celite-immobilized enzymes maintained high levels of stereoselectivity in the synthesis of tetrahydroisoquinoline alkaloids, with only minor reductions compared to the free enzyme. These results are particularly relevant for the development of scalable and sustainable biocatalytic processes, where stereoselectivity is critical.

Finally, coarse-grained Monte Carlo simulations offered molecular-level insights into enzyme-support interactions. The simulations suggested that histidine-rich residues within the engineered N-terminal tag play a central role in mediating the adsorption of Δ19*Tf*NCS onto kaolin. These findings corroborated the experimental zeta potential data and supported the hypothesis of a preferential orientation that maintains the catalytic site accessible to the solvent, thus preserving enzymatic function.

Together, the integration of experimental and computational methodologies provided a relevant contribution to the rational design and evaluation of immobilized (*S*)-NCS. The study highlights the viability of using kaolin as an effective and scalable support for (*S*)-NCS, offering a combination of low cost, high stability, and preserved catalytic performance.

7 FUTURE PERPECTIVES

- Evaluation of more active *Tf*NCS variants obtained through protein engineering, aiming to enhance catalytic activity and selectivity.
- Removal of the His-tag from Δ19*Tf*NCS to experimentally investigate the role of this region in protein–matrix interactions.
- Chemical functionalization of kaolin and Celite 545 to enable covalent immobilization strategies, aiming to improve enzyme retention and stability.
- Exploration of nanomaterials as support matrices to increase surface area per unit mass, including:
    - Magnetic nanoparticles, for facilitated biocatalyst recovery.
    - Kaolin-based nanoparticles, maintaining chemical compatibility with the enzyme.
- Application of solid-state NMR spectroscopy using isotopically enriched Δ19*Tf*NCS immobilized on kaolin to:
    - Experimentally identify enzyme residues involved in surface interactions.
    - Investigate structural changes in the enzyme upon immobilization.

STATEMENT ON THE USE OF ARTIFICIAL INTELLIGENCE

I declare that the content of this thesis was entirely written by me, based on my original research. To improve the clarity, fluency, and linguistic accuracy of the text, I used generative artificial intelligence tools, specifically ChatGPT (OpenAI), as support for scientific language revision in both English and Portuguese.

The use of AI was limited to the reformulation of excerpts previously written by me, with the goal of enhancing terminological precision, textual cohesion, and academic style, without compromising the scientific content, authorship, or originality of this thesis.

REFERENCES

ALI, Ali O. *et al.* Epoxy functionalized iron oxide magnetic nanoparticles for catalase enzyme covalent immobilization. **Chemical Papers**, v. 76, n. 7, p. 4431–4441, 1 jul. 2022.

ARANAZ, I. *et al.* Optimization of d-amino acid production catalyzed by immobilized multi-enzyme system in polyelectrolyte complex gel capsules. **Journal of Molecular Catalysis B: Enzymatic**, v. 121, p. 45–52, 1 nov. 2015.

ARIAEENEJAD, Shohreh; MOTAMEDI, Elaheh. Carboxylated nanocellulose from quinoa husk for enhanced protease immobilization and stability of protease in biotechnological applications. **Scientific Reports**, v. 15, n. 1, p. 256, 2 jan. 2025.

ARNOLD, Adson Hagen; CASTIGLIONE, Kathrin. Comparative Evaluation of the Asymmetric Synthesis of (S)-Norlaudanosoline in a Two-Step Biocatalytic Reaction with Whole Escherichia coli Cells in Batch and Continuous Flow Catalysis. **Catalysts**, v. 13, n. 10, p. 1347, out. 2023.

BERKNER, Hanna *et al.* High-yield expression and purification of isotopically labeled norcoclaurine synthase, a Bet v 1-homologous enzyme, from Thalictrum flavum for NMR studies. **Protein Expression and Purification**, v. 56, n. 2, p. 197–204, dez. 2007.

BERNAL, Claudia; RODRÍGUEZ, Karen; MARTÍNEZ, Ronny. Integrating enzyme immobilization and protein engineering: An alternative path for the development of novel and improved industrial biocatalysts. **Biotechnology Advances**, v. 36, n. 5, p. 1470–1480, 1 set. 2018.

BONAMORE, Alessandra *et al.* Norcoclaurine Synthase: Mechanism of an Enantioselective Pictet-Spengler Catalyzing Enzyme. **Molecules**, v. 15, n. 4, p. 2070–2078, abr. 2010.

BRITTON, Joshua; MAJUMDAR, Sudipta; WEISS, Gregory A. Continuous flow biocatalysis. **Chemical Society Reviews**, v. 47, n. 15, p. 5891–5918, 30 jul. 2018.

BURGESS, Richard R. A brief practical review of size exclusion chromatography: Rules of thumb, limitations, and troubleshooting. **Protein Expression and Purification**, v. 150, p. 81–85, 1 out. 2018.

CAETANO, Daniel L. Z. *et al.* Adsorption of lysozyme into a charged confining pore. **Physical Chemistry Chemical Physics**, v. 23, n. 48, p. 27195–27206, 15 dez. 2021.

CAO, Linqiu; VAN RANTWIJK, Fred; SHELDON, Roger A. Cross-Linked Enzyme Aggregates: A Simple and Effective Method for the Immobilization of Penicillin Acylase. **Organic Letters**, v. 2, n. 10, p. 1361–1364, 1 maio 2000.

CHEN, Wei-Hai *et al.* Biocatalytic cascades driven by enzymes encapsulated in metal–organic framework nanoparticles. **Nature Catalysis**, v. 1, n. 9, p. 689–695, set. 2018.

CHERSTVY, A. G. Critical polyelectrolyte adsorption under confinement: Planar slit, cylindrical pore, and spherical cavity. **Biopolymers**, v. 97, n. 5, p. 311–317, 2012.

CLEMENTI, Cecilia; NYMEYER, Hugh; ONUCHIC, José Nelson. Topological and energetic factors: what determines the structural details of the transition state ensemble and “en-route” intermediates for protein folding? an investigation for small globular proteins1. **Journal of Molecular Biology**, v. 298, n. 5, p. 937–953, 19 maio 2000.

COCHRAN, William G.; COX, Gertrude M. **Experimental Designs, 2nd Edition | Wiley**. 2. ed. *[S.l.]*: Wiley, 1992.

CONTESSOTO, Vinícius G. *et al.* NTL9 Folding at Constant pH: The Importance of Electrostatic Interaction and pH Dependence. **Journal of Chemical Theory and Computation**, v. 12, n. 7, p. 3270–3277, 12 jul. 2016.

CRUZ, Guillermo *et al.* Enhancing rhamnolipid production via immobilized *Pseudomonas stutzeri* lipase: A comparative study. **Bioorganic Chemistry**, v. 153, p. 107855, 1 dez. 2024.

DE OLIVEIRA, Vinícius M. *et al.* pH and Charged Mutations Modulate Cold Shock Protein Folding and Stability: A Constant pH Monte Carlo Study. **Journal of Chemical Theory and Computation**, v. 16, n. 1, p. 765–772, 14 jan. 2020.

DE SOUZA LIMA, J. *et al.* Immobilization of endoglucanase on kaolin by adsorption and covalent bonding. **Bioprocess and Biosystems Engineering**, v. 44, n. 8, p. 1627–1637, 2021.

DE SOUZA LIMA, J. *et al.* Cellulase immobilized on kaolin as a potential approach to improve the quality of knitted fabric. **Bioprocess and Biosystems Engineering**, v. 45, n. 4, p. 679–688, 2022.

DELGADO, A. V. *et al.* Measurement and interpretation of electrokinetic phenomena. **Journal of Colloid and Interface Science**, Elkin 06, International Electrokinetics Conference, June 25-29, Nancy, France. v. 309, n. 2, p. 194–224, 15 maio 2007.

EL-ZAHAB, Bilal; JIA, Hongfei; WANG, Ping. Enabling multienzyme biocatalysis using nanoporous materials. **Biotechnology and Bioengineering**, v. 87, n. 2, p. 178–183, 20 jul. 2004.

ERDMANN, Vanessa *et al.* Enzymatic and Chemoenzymatic Three-Step Cascades for the Synthesis of Stereochemically Complementary Trisubstituted Tetrahydroisoquinolines. **Angewandte Chemie International Edition**, v. 56, n. 41, p. 12503–12507, 2017.

FAI, A. E. C. *et al.* Immobilization of fungi β-galactosidase on celite to produce galactooligosaccharides during lactose hydrolysis. v. 24, n. 1, p. 353–358, 2017.

FERNANDES, Humberto *et al.* Structural and functional aspects of PR-10 proteins. **The FEBS Journal**, v. 280, n. 5, p. 1169–1199, 2013.

FRÖHLING, Magnus; HIETE, Michael (ORGS.). **Sustainability and Life Cycle Assessment in Industrial Biotechnology**. Cham: Springer International Publishing, 2020. v. 173

GALANIE, Stephanie *et al.* Complete biosynthesis of opioids in yeast. **Science**, v. 349, n. 6252, p. 1095–1100, 4 set. 2015.

GHIRGA, Francesca *et al.* Occurrence of Enantioselectivity in Nature: The Case of (S)-Norcoclaurine. **Chirality**, v. 28, n. 3, p. 169–180, 2016.

GRÄSLUND, Torbjörn *et al.* Charge engineering of a protein domain to allow efficient ion-exchange recovery. **Protein Engineering**, v. 13, n. 10, p. 703–709, 1 out. 2000.

GUISAN, Jose M. *et al.* (ORGS.). **Immobilization of Enzymes and Cells: Methods and Protocols**. New York, NY: Springer US, 2020. v. 2100

GUISAN, Jose M. *et al.* Enzyme immobilization strategies for the design of robust and efficient biocatalysts. **Current Opinion in Green and Sustainable Chemistry**, v. 35, p. 100593, 1 jun. 2022.

H. ORREGO, Alejandro *et al.* Stabilization of Enzymes by Multipoint Covalent Attachment on Aldehyde-Supports: 2-Picoline Borane as an Alternative Reducing Agent. **Catalysts**, v. 8, n. 8, p. 333, ago. 2018.

HAJILI, Emil; SUGAWARA, Akihide; UYAMA, Hiroshi. Application of Hierarchically Porous Chitosan Monolith for Enzyme Immobilization. **Biomacromolecules**, v. 25, n. 6, p. 3486–3498, 10 jun. 2024.

HAMZAH, Sofiah; NASIR, Fatin; HAMZAH, Amirah. Lysozyme Adsorption Onto Immobilised Metal Affinity Chromatographic Adsorbent: Effect of pH and Ionic Strength. **International Journal of Applied Engineering Research**, v. 9, p. 17783–17792, 1 jan. 2014.

HAN, Qi *et al.* Potassium Fluoride on Celite. *In*: **Encyclopedia of Reagents for Organic Synthesis**. *[S.l.]*: John Wiley & Sons, Ltd, 2009.

HERNÁNDEZ-GARCÍA, Samanta; GARCÍA-GARCÍA, María Inmaculada; GARCÍA-CARMONA, Francisco. Improving the production, activity, and stability of CLEAs with diepoxides. **Biotechnology Progress**, v. 33, n. 5, p. 1425–1429, 2017.

ILARI, Andrea *et al.* Structural basis of enzymatic (S)-norcoclaurine biosynthesis. **The Journal of Biological Chemistry**, v. 284, n. 2, p. 897–904, 9 jan. 2009.

JESIONOWSKI, Teofil; ZDARTA, Jakub; KRAJEWSKA, Barbara. Enzyme immobilization by adsorption: a review. **Adsorption**, v. 20, n. 5, p. 801–821, 1 ago. 2014.

JI, Xiaoyuan *et al.* Tethering of Nicotinamide Adenine Dinucleotide Inside Hollow Nanofibers for High-Yield Synthesis of Methanol from Carbon Dioxide Catalyzed by Coencapsulated Multienzymes. **ACS Nano**, v. 9, n. 4, p. 4600–4610, 28 abr. 2015.

JIA, Junqi *et al.* Novel Magnetic Cross-Linked Cellulase Aggregates with a Potential Application in Lignocellulosic Biomass Bioconversion. **Molecules**, v. 22, n. 2, p. 269, fev. 2017.

JÚNIOR, Aldo Araújo da Trindade *et al.* Multicatalytic Hybrid Materials for Biocatalytic and Chemoenzymatic Cascades—Strategies for Multicatalyst (Enzyme) Co-Immobilization. **Catalysts**, v. 11, n. 8, p. 936, ago. 2021.

KLIBANOV, Alexander M. Enzyme stabilization by immobilization. **Analytical Biochemistry**, v. 93, p. 1–25, 1 jan. 1979.

KLIBANOV, Alexander M. Improving enzymes by using them in organic solvents. **Nature**, v. 409, n. 6817, p. 241–246, jan. 2001.

KOGA, N.; TAKADA, S. Roles of native topology and chain-length scaling in protein folding: a simulation study with a Go-like model. **Journal of Molecular Biology**, v. 313, n. 1, p. 171–180, 12 out. 2001.

LADAVOS, A. K. *et al.* The BET equation, the inflection points of N2 adsorption isotherms and the estimation of specific surface area of porous solids. **Microporous and Mesoporous Materials**, v. 151, p. 126–133, 15 mar. 2012.

LECHNER, Horst *et al.* Library of Norcoclaurine Synthases and Their Immobilization for Biocatalytic Transformations. **Biotechnology Journal**, v. 13, n. 3, p. 1700542, 2018.

LI, Qingzhong *et al.* Enzyme Immobilization on Carboxyl-Functionalized Graphene Oxide for Catalysis in Organic Solvent. **Industrial & Engineering Chemistry Research**, v. 52, n. 19, p. 6343–6348, 15 maio 2013.

LI, Xinyi *et al.* Phylogenetic analysis and functional characterization of norcoclaurine synthase involved in benzylisoquinoline alkaloids biosynthesis in Stephania tetrandra. **Journal of Cellular Physiology**, v. 239, n. 10, p. e31065, 2024.

LICHMAN, B. R. **Norcoclaurine synthase: the mechanism and biocatalytic potential of a Pictet-Spenglerase**. Doctoral—London, England: UCL (University College London), 28 jan. 2016.

LICHMAN, Benjamin R. *et al.* One-pot triangular chemoenzymatic cascades for the syntheses of chiral alkaloids from dopamine. **Green Chemistry**, v. 17, n. 2, p. 852–855, 2015a.

LICHMAN, Benjamin R. *et al.* "Dopamine-first" mechanism enables the rational engineering of the norcoclaurine synthase aldehyde activity profile. **The FEBS journal**, v. 282, n. 6, p. 1137–1151, mar. 2015b.

LICHMAN, Benjamin R. *et al.* Enzyme catalysed Pictet-Spengler formation of chiral 1,1'-disubstituted- and spiro-tetrahydroisoquinolines. **Nature Communications**, v. 8, n. 1, p. 14883, 3 abr. 2017a.

LICHMAN, Benjamin R. *et al.* Structural Evidence for the Dopamine-First Mechanism of Norcoclaurine Synthase. **Biochemistry**, v. 56, n. 40, p. 5274–5277, 10 out. 2017b.

LIU, Qian; XUN, Guanhua; FENG, Yan. The state-of-the-art strategies of protein engineering for enzyme stabilization. **Biotechnology Advances**, Biorefining: an indispensable solution for bioresource utilization and sustainable development. v. 37, n. 4, p. 530–537, 1 jul. 2019.

LØHRE, Camilla *et al.* A Workup Protocol Combined with Direct Application of Quantitative Nuclear Magnetic Resonance Spectroscopy of Aqueous Samples from Large-Scale Steam Explosion of Biomass. **ACS Omega**, v. 6, n. 10, p. 6714–6721, 16 mar. 2021.

LUK, Louis Y. P. *et al.* Mechanistic Studies on Norcoclaurine Synthase of Benzylisoquinoline Alkaloid Biosynthesis: An Enzymatic Pictet−Spengler Reaction. **Biochemistry**, v. 46, n. 35, p. 10153–10161, 1 set. 2007.

LUND, Mikael; JÖNSSON, Bo. On the charge regulation of proteins. **Biochemistry**, v. 44, n. 15, p. 5722–5727, 19 abr. 2005.

LUO, Jianquan *et al.* Cascade catalysis in membranes with enzyme immobilization for multi-enzymatic conversion of CO2 to methanol. **New Biotechnology**, v. 32, n. 3, p. 319–327, 25 maio 2015.

MAGHRABY, Yasmin R. *et al.* Enzyme Immobilization Technologies and Industrial Applications. **ACS Omega**, v. 8, n. 6, p. 5184–5196, 14 fev. 2023.

MALLIN, H.; WULF, H.; BORNSCHEUER, U. T. A self-sufficient Baeyer–Villiger biocatalysis system for the synthesis of ε-caprolactone from cyclohexanol. **Enzyme and Microbial Technology**, v. 53, n. 4, p. 283–287, 10 set. 2013.

MARESH, Justin J. *et al.* Facile one-pot synthesis of tetrahydroisoquinolines from amino acids via hypochlorite-mediated decarboxylation and Pictet–Spengler condensation. **Tetrahedron Letters**, v. 55, n. 36, p. 5047–5051, 3 set. 2014.

MINAMI, Hiromichi *et al.* Functional Analysis of Norcoclaurine Synthase in *Coptis japonica**. **Journal of Biological Chemistry**, v. 282, n. 9, p. 6274–6282, 2 mar. 2007.

MYERS, Raymond H.; MONTGOMERY, Douglas C.; ANDERSON-COOK, Christine M. **Response Surface Methodology: Process and Product Optimization Using Designed Experiments**. 4th. ed. *[S.l.]*: Wiley, 2016.

NISHIHACHIJO, M. *et al.* Asymmetric synthesis of tetrahydroisoquinolines by enzymatic Pictet-Spengler reaction. **Bioscience, Biotechnology and Biochemistry**, v. 78, n. 4, p. 701–707, 2014.

OVERVOORDE, Lois M. *et al.* Mechanistic Insights into a BINOL-Derived Phosphoric Acid-Catalyzed Asymmetric Pictet–Spengler Reaction. **The Journal of Organic Chemistry**, v. 80, n. 5, p. 2634–2640, 6 mar. 2015.

PALOMINO, Angelica M.; BURNS, Susan E.; SANTAMARINA, J. Carlos. Mixtures of Fine-Grained Minerals — Kaolinite and Carbonate Grains. **Clays and Clay Minerals**, v. 56, n. 6, p. 599–611, dez. 2008.

PESNOT, Thomas *et al.* The Catalytic Potential of Coptis japonica NCS2 Revealed – Development and Utilisation of a Fluorescamine-Based Assay. **Advanced Synthesis & Catalysis**, v. 354, n. 16, p. 2997–3008, 2012.

PUNEKAR, Narayan S. **ENZYMES: Catalysis, Kinetics and Mechanisms**. Singapore: Springer Nature, 2025.

PYNE, Michael E. *et al.* A yeast platform for high-level synthesis of tetrahydroisoquinoline alkaloids. **Nature Communications**, v. 11, n. 1, p. 3337, 3 jul. 2020.

RADAUER, Christian; LACKNER, Peter; BREITENEDER, Heimo. The Bet v 1 fold: an ancient, versatile scaffold for binding of large, hydrophobic ligands. **BMC Evolutionary Biology**, v. 8, n. 1, p. 286, 15 out. 2008.

REED, Christopher E.; REED, Wayne F. Monte Carlo study of titration of linear polyelectrolytes. **The Journal of Chemical Physics**, v. 96, n. 2, p. 1609–1620, 15 jan. 1992.

REZAEI, Saghar *et al.* Development of a novel bi-enzymatic silver dendritic hierarchical nanostructure cascade catalytic system for efficient conversion of starch into gluconic acid. **Chemical Engineering Journal**, v. 356, p. 423–435, 15 jan. 2019.

RODDAN, Rebecca *et al.* Acceptance and Kinetic Resolution of α-Methyl-Substituted Aldehydes by Norcoclaurine Synthases. **ACS Catalysis**, v. 9, n. 10, p. 9640–9649, 4 out. 2019.

RODDAN, Rebecca *et al.* Single step syntheses of (1S)-aryl-tetrahydroisoquinolines by norcoclaurine synthases. **Communications Chemistry**, v. 3, n. 1, p. 1–10, 13 nov. 2020.

ROSSINO, Giacomo *et al.* Biocatalysis: A smart and green tool for the preparation of chiral drugs. **Chirality**, v. 34, n. 11, p. 1403–1418, 2022.

RUEFFER, Martina *et al.* (*S*)-norlaudanosoline synthase: The first enzyme in the benzylisoquinoline biosynthetic pathway. **FEBS Letters**, v. 129, n. 1, p. 5–9, 29 jun. 1981.

RUFF, Bettina M.; BRÄSE, S.; O'CONNOR, Sarah E. Biocatalytic production of tetrahydroisoquinolines. **Tetrahedron Letters**, v. 53, n. 9, p. 1071–1074, 29 fev. 2012.

SALVATTI, Brunno A. *et al.* Understanding the Enzyme (S)-Norcoclaurine Synthase Promiscuity to Aldehydes and Ketones. **Journal of Chemical Information and Modeling**, v. 64, n. 11, p. 4462–4474, 10 jun. 2024.

SAMANANI, Nailish; FACCHINI, Peter J. Isolation and partial characterization of norcoclaurine synthase, the first committed step in benzylisoquinoline alkaloid biosynthesis, from opium poppy. **Planta**, v. 213, n. 6, p. 898–906, 1 out. 2001.

SAMANANI, Nailish; FACCHINI, Peter J. Purification and Characterization of Norcoclaurine Synthase: THE FIRST COMMITTED ENZYME IN BENZYLISOQUINOLINE ALKALOID BIOSYNTHESIS IN PLANTS*. **Journal of Biological Chemistry**, v. 277, n. 37, p. 33878–33883, 13 set. 2002.

SAMANANI, Nailish; LISCOMBE, David K.; FACCHINI, Peter J. Molecular cloning and characterization of norcoclaurine synthase, an enzyme catalyzing the first committed step in benzylisoquinoline alkaloid biosynthesis. **The Plant Journal**, v. 40, n. 2, p. 302–313, 2004.

SANTOS, Maiara da S.; COLNAGO, Luiz Alberto. Validação de método quantitativo por RMN de ^{1}H para análises de formulações farmacêuticas. **Química Nova**, v. 36, p. 324–330, 2013.

SATAR, Rukhsana; HUSAIN, Qayyum. Adsorption of peroxidase on Celite 545 directly from ammonium sulfate fractionated white radish (Raphanus sativus) proteins. **Biotechnology Journal**, v. 4, n. 3, p. 408–416, 2009.

ŠEKULJICA, Nataša Ž. *et al.* Immobilization of horseradish peroxidase onto kaolin. **Bioprocess and Biosystems Engineering**, v. 39, n. 3, p. 461–472, 1 mar. 2016.

SHELDON, Roger A.; BRADY, Dean. The limits to biocatalysis: pushing the envelope. **Chemical Communications**, v. 54, n. 48, p. 6088–6104, 12 jun. 2018.

SHELDON, Roger A.; PEREIRA, Pedro C. Biocatalysis engineering: the big picture. **Chemical Society Reviews**, v. 46, n. 10, p. 2678–2691, 22 maio 2017.

SHEN, Qiuyun *et al.* Gelatin-templated biomimetic calcification for β-galactosidase immobilization. **Process Biochemistry**, v. 46, n. 8, p. 1565–1571, 1 ago. 2011.

SHENG, Xiang; HIMO, Fahmi. Enzymatic Pictet–Spengler Reaction: Computational Study of the Mechanism and Enantioselectivity of Norcoclaurine Synthase. **Journal of the American Chemical Society**, v. 141, n. 28, p. 11230–11238, 17 jul. 2019.

SIMÕES, Ana L. A. *et al.* 3D Graphene-Like Carbon Structures from Poly(Acrylic Acid): A Novel Synthetic Route. **Chemistry – An Asian Journal**, v. 20, n. 2, p. e202400832, 2025.

SOBOLEV, V. *et al.* Automated analysis of interatomic contacts in proteins. **Bioinformatics (Oxford, England)**, v. 15, n. 4, p. 327–332, abr. 1999.

SOBOLEV, V.; EDELMAN, M. Modeling the quinone-B binding site of the photosystem-II reaction center using notions of complementarity and contact-surface between atoms. **Proteins**, v. 21, n. 3, p. 214–225, mar. 1995.

STADLER, R. *et al.* Revision of the early steps of reticuline biosynthesis. **Tetrahedron Letters**, v. 28, n. 12, p. 1251–1254, 1 jan. 1987.

STADLER, Richard; KUTCHAN, Toni M.; ZENK, Meinhart H. (*S*)-norcoclaurine is the central intermediate in benzylisoquinoline alkaloid biosynthesis. **Phytochemistry**, v. 28, n. 4, p. 1083–1086, 1 jan. 1989.

STADLER, Richard; ZENK, Meinhart H. A revision of the generally accepted pathway for the biosynthesis of the benzyltetrahydroisoquinoline alkaloid reticuline. **Liebigs Annalen der Chemie**, v. 1990, n. 6, p. 555–562, 1990.

STICKLER, Benjamin A.; SCHACHINGER, Ewald. **Basic Concepts in Computational Physics**. Cham: Springer International Publishing, 2016.

STÖCKIGT, Joachim *et al.* The Pictet–Spengler Reaction in Nature and in Organic Chemistry. **Angewandte Chemie International Edition**, v. 50, n. 37, p. 8538–8564, 2011.

SZEWCZUK-KARPISZ, Katarzyna *et al.* Chromium(VI) reduction and accumulation on the kaolinite surface in the presence of cationic soil flocculant. **Journal of Soils and Sediments**, v. 20, n. 10, p. 3688–3697, 1 out. 2020.

TAN, Cheau Yuaan *et al.* Immobilization of a Bacterial Cytochrome P450 Monooxygenase System on a Solid Support. **Angewandte Chemie International Edition**, v. 55, n. 48, p. 15002–15006, 2016.

The Nobel Prize in Chemistry 2018. Disponível em: <https://www.nobelprize.org/prizes/chemistry/2018/summary/>. Acesso em: 9 abr. 2025.

TRENCHARD, Isis J. *et al. De novo* production of the key branch point benzylisoquinoline alkaloid reticuline in yeast. **Metabolic Engineering**, v. 31, p. 74–83, 1 set. 2015.

VALIKHANI, Donya *et al.* A tailor-made, self-sufficient and recyclable monooxygenase catalyst based on coimmobilized cytochrome P450 BM3 and glucose dehydrogenase. **Biotechnology and Bioengineering**, v. 115, n. 10, p. 2416–2425, 2018.

VANDEN EYNDEN, Matthew J.; KUNCHITHAPATHAM, Kamala; STAMBULI, James P. Calcium-Promoted Pictet-Spengler Reactions of Ketones and Aldehydes. **The Journal of Organic Chemistry**, v. 75, n. 24, p. 8542–8549, 17 dez. 2010.

VELASCO-LOZANO, Susana *et al.* Carrier-Free Immobilization of Lipase from Candida rugosa with Polyethyleneimines by Carboxyl-Activated Cross-Linking. **Biomacromolecules**, v. 15, n. 5, p. 1896–1903, 12 maio 2014.

VELASCO-LOZANO, Susana *et al.* Co-immobilization and Colocalization of Multi-Enzyme Systems for the Cell-Free Biosynthesis of Aminoalcohols. **ChemCatChem**, v. 12, n. 11, p. 3030–3041, 2020.

VITALIS, Andreas; PAPPU, Rohit V. Methods for Monte Carlo simulations of biomacromolecules. **Annual Reports in Computational Chemistry**, v. 5, p. 49–76, 1 jan. 2009.

WANG, D. *et al.* Optimizing enzymatic bioreactors: The role of mass transfer in enhancing catalytic efficiency and stability. **Chemical Engineering Journal**, v. 508, 2025.

WEBB, Benjamin; SALI, Andrej. Comparative Protein Structure Modeling Using MODELLER. **Current Protocols in Bioinformatics**, v. 54, p. 5.6.1-5.6.37, 20 jun. 2016.

WELTZ, James S. *et al.* Reduced Enzyme Dynamics upon Multipoint Covalent Immobilization Leads to Stability-Activity Trade-off. **Journal of the American Chemical Society**, v. 142, n. 7, p. 3463–3471, 19 fev. 2020.

WHITFORD, Paul C. *et al.* An all-atom structure-based potential for proteins: bridging minimal models with all-atom empirical forcefields. **Proteins**, v. 75, n. 2, p. 430–441, 1 maio 2009.

WIESBAUER, Johanna *et al.* Oriented Immobilization of Enzymes Made Fit for Applied Biocatalysis: Non-Covalent Attachment to Anionic Supports using Zbasic2 Module. **ChemCatChem**, v. 3, n. 8, p. 1299–1303, 2011.

WILKINS, Marc R. *et al.* Protein Identification and Analysis Tools in the ExPASy Server. *In*: LINK, Andrew J. (Org.). **2-D Proteome Analysis Protocols**. Totowa, NJ: Humana Press, 1999. p. 531–552.

WILSON, Lorena *et al.* Encapsulation of crosslinked penicillin G acylase aggregates in lentikats: Evaluation of a novel biocatalyst in organic media. **Biotechnology and Bioengineering**, v. 86, n. 5, p. 558–562, 2004.

WILSON, M. L.; COSCIA, C. J. Early stages of Papaver alkaloid biogenesis. **Journal of the American Chemical Society**, v. 97, n. 2, p. 431–432, 1 jan. 1975.

YOUN, So Won. The Pictet-Spengler Reaction: Efficient Carbon-Carbon Bond Forming Reaction in Heterocyclic Synthesis. **Organic Preparations and Procedures International**, v. 38, n. 6, p. 505–591, 1 dez. 2006.

YU, Gaobo; LIU, Jie; ZHOU, Jian. Mesoscopic coarse-grained simulations of lysozyme adsorption. **The Journal of Physical Chemistry. B**, v. 118, n. 17, p. 4451–4460, 1 maio 2014.

YU, Gaobo; ZHOU, Jian. Understanding the curvature effect of silica nanoparticles on lysozyme adsorption orientation and conformation: a mesoscopic coarse-grained simulation study. **Physical Chemistry Chemical Physics**, v. 18, n. 34, p. 23500–23507, 24 ago. 2016.

ZENG, Jia; LI, Ding. Expression and purification of His-tagged rat mitochondrial 3-ketoacyl-CoA thiolase wild-type and His352 mutant proteins. **Protein Expression and Purification**, v. 35, n. 2, p. 320–326, 1 jun. 2004.

ZHANG, Guanghui *et al.* Lipase Immobilized on Graphene Oxide As Reusable Biocatalyst. **Industrial & Engineering Chemistry Research**, v. 53, n. 51, p. 19878–19883, 24 dez. 2014.

ZHANG, Man *et al.* Engineering a norcoclaurine synthase for one-step synthesis of (S)-1-aryl-tetrahydroisoquinolines. **Bioresources and Bioprocessing**, v. 10, n. 1, p. 15, 1 mar. 2023.

ZHANG, Shiqing *et al.* Computational mechanistic investigation of the kinetic resolution of α-methyl-phenylacetaldehyde by norcoclaurine synthase. **Communications Chemistry**, v. 7, n. 1, p. 1–7, 27 mar. 2024.

ZHAO, J. *et al.* Norcoclaurine Synthase-Mediated Stereoselective Synthesis of 1,1'-Disubstituted, Spiro- And Bis-Tetrahydroisoquinoline Alkaloids. **ACS Catalysis**, v. 11, n. 1, p. 131–138, 2021.

ZHAO, Jianxiong *et al.* One-pot chemoenzymatic synthesis of trolline and tetrahydroisoquinoline analogues. **Chemical Communications**, v. 54, n. 11, p. 1323–1326, 1 fev. 2018.

APPENDIX

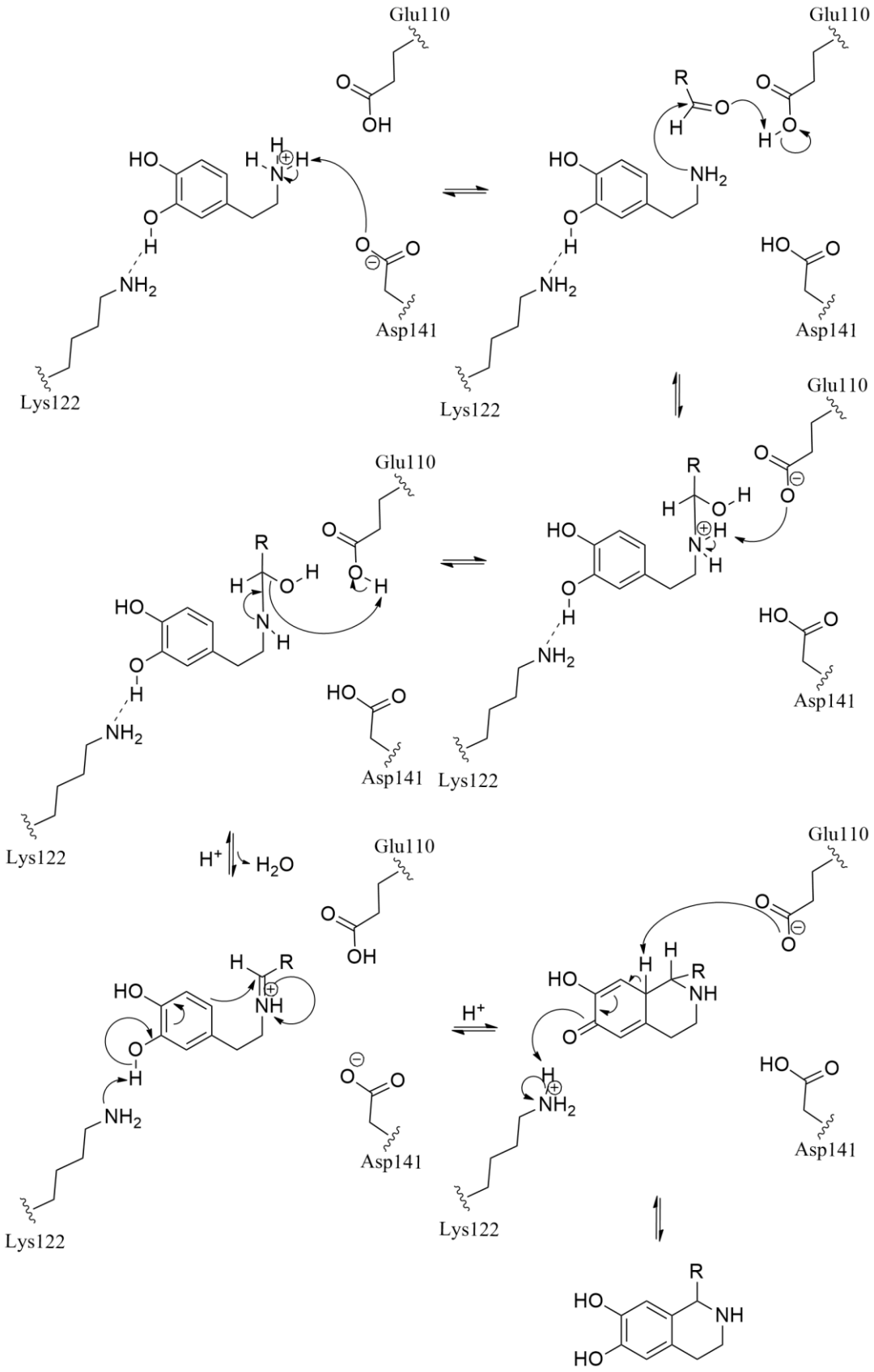

Figure A1 Dopamine-first mechanism. Mechanism model proposed by Sheng and Himo (2019) with simplifications.

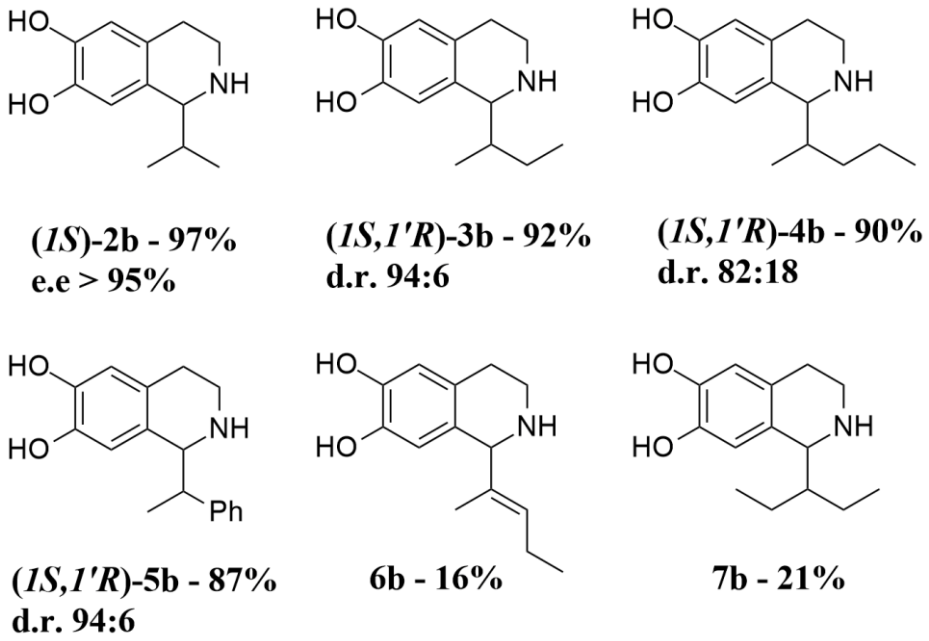

Figure A2 Reaction products obtained by Roddan et al. (2019) using Δ33*Tf*NCS. Reactions were performed with dopamine·HCl (10 mM), aldehyde (20 mM), sodium ascorbate (5 mM), and Δ33*Tf*NCS (0.2 mg·mL^{-1}) in HEPES buffer (100 mM, pH 7.5) containing 10% DMSO (v/v), at 37 °C for 18 h in 250 µL scale. The reported diastereomeric ratios (d.r.) indicate predominant formation of the (*1S,1'R*) stereoisomer.

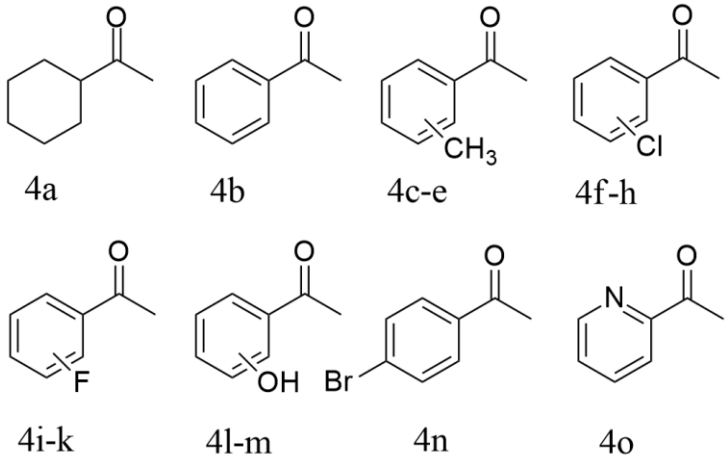

Figure A3 Benzaldehydes used by Roddan et. al. (2020) in the synthesis of (1S)-aryl-tetrahydroisoquinolines. For compounds 4c to 4k the substituents are in positions *ortho*-, *metha*- and *para*- following the alphabetical order. For compounds 4l and 4n the substituents are in positions *metha*- and *para*- respectively.

Table A1. Library of 11 amines tested by Pesnot et al. (2012). Reaction between amines and 4-HPAA (1h and 37 °C).

Compound n°/ conversion	Amine	Compound n°/ conversion	Amine
1 – 81%	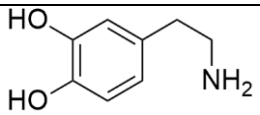	38 – 77%	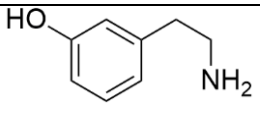

33 – 0%	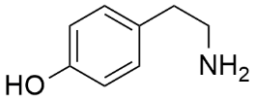	39 – 0%	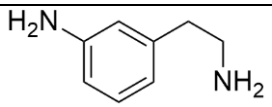
34 – 0%	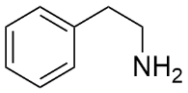	40 – 0%	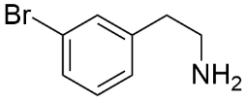
35 – 0%	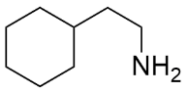	41 – 0%	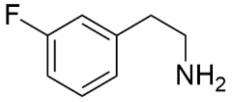
36 – 0%	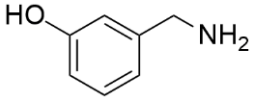	42 – 0%	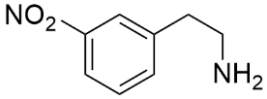
37 – 33%	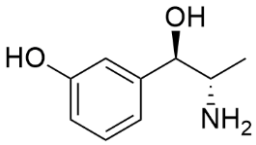		

Table A2. Library of 27 aldehydes and 1 ketone tested by Pesnot et al. (2012). Reaction between carbonylic compounds and dopamine (1h and 37 °C).

Compound n°/ conversion	Carbonylic compound	Compound n°/ conversion	Carbonylic compound
2 – 86%	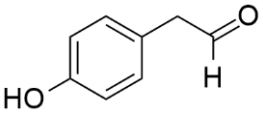	19 – 54%	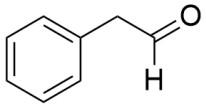
6 - ~ 0%	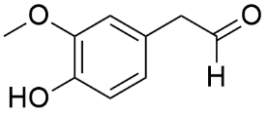	20 – 0%	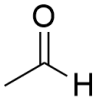
7- ~ 0%	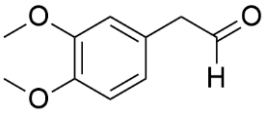	21 - ~ 0%	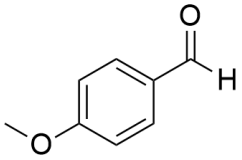
8 - 36%	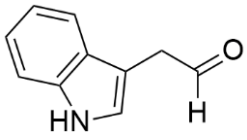	22 – 0%	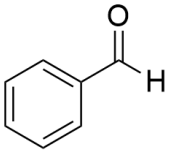
9 - 47%	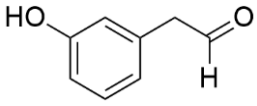	23 – 0%	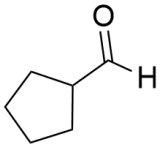
10 - 46%	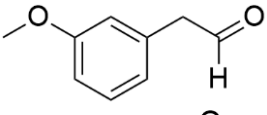	24 – cold not be determined	
11 - 32%	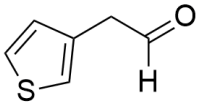	25 – 55%	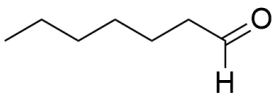
12 – 99%	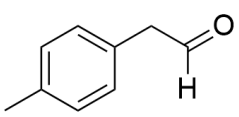	26 - ~ 0%	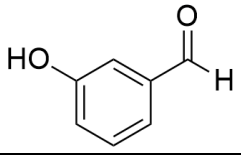

13 - ~ 0%	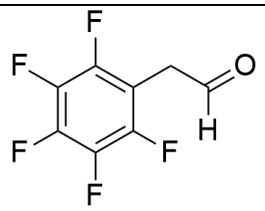	27 - ~ 0%	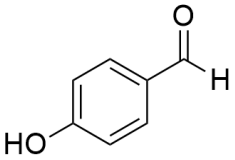
14 – 28%	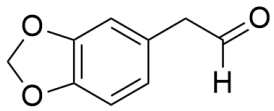	28 - ~ 0%	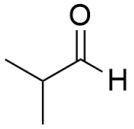
15 – 88%	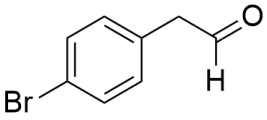	29 – 0%	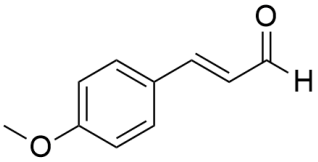
16 – 83%	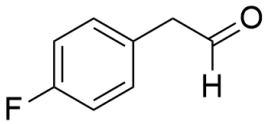	30 – 0%	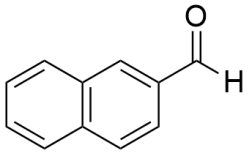
17 – 87%	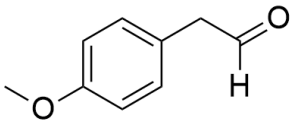	31 – 0%	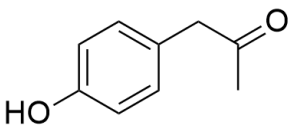
18 - ~ 0%	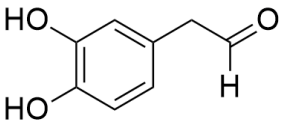	32 – 62%	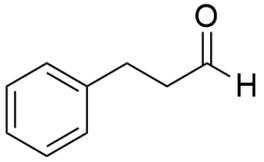

Table A3. Library of 20 aldehydes tested by Ruff; Bräse; O'Connor (2012). Reaction between aldehydes and dopamine (3h and 37 °C).

Compound n°/ conversion	Carbonylic compound	Compound n°/ conversion	Carbonylic compound
4 – 60%	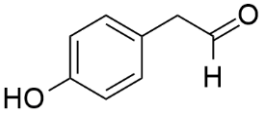	16 – 51%	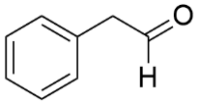
7 – 65%	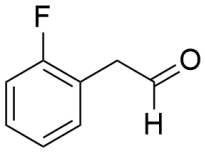	17 – 68%	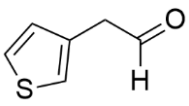
8 – 66%	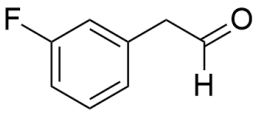	18 – 61%	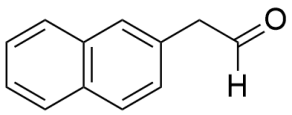
9 – 71%	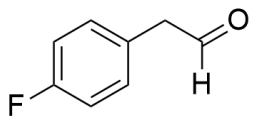	19 – 71%	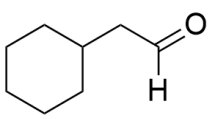
10 – 66%	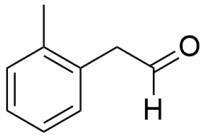	20 – 42%	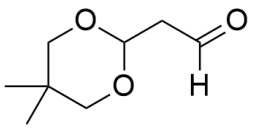

11 – 58%	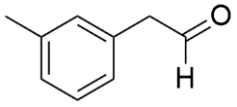	21 – 52%	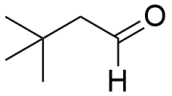
12 – 57%	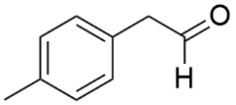	22 – Not detected	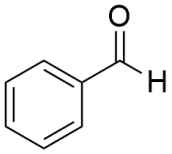
13 – 69%	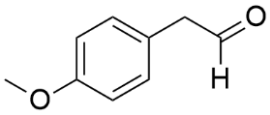	23 – Not detected	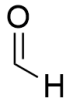
14 – 69%	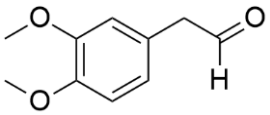	24 – Not detected	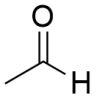
15 – 65%	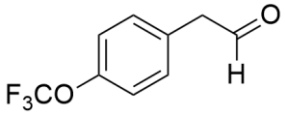	25 – Not detected	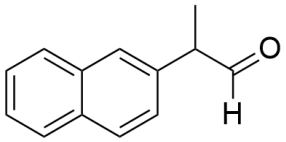

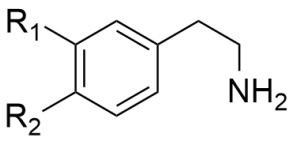

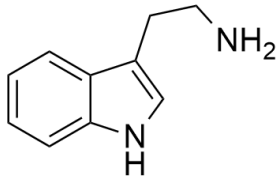

41 - R_1 = H, R_2 = F
42 - R_1 = H, R_2 = NH_2
43 - R_1 = OMe, R_2 = H
44 - R_1 = R_2 = H
46 - R_1 = OH, R_2 = H
47 - R_1 = OH, R_2 = OMe

45 - tryptamine

Figure A4. Library of 6 aldehydes tested by Ruff; Bräse; O'Connor (2012). Reaction between amines and 4-HPAA (3h and 37 °C).

Table A4. Library of 9 inedited aldehydes tested by (Nishihachijo et al., 2014). Reaction between 10 mM aldehydes and 10 mM dopamine (15 min and 30 °C).

Compound conversion	**Amine**	**Compound conversion**	**Amine**
3-phenylpropanal 99%	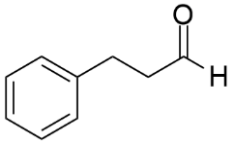	isobutanal 6%	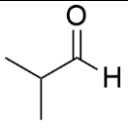
3-(4-(trifluoromethyl) phenyl) propanal 82%	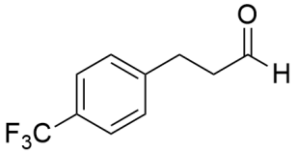	pentanal 67%	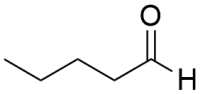

2-phenylpropanal 8%	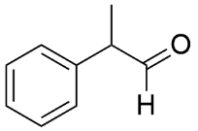	hexanal 27%	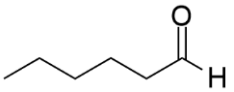
3-(4 isopropylphenyl)-2-methylpropanal 2%	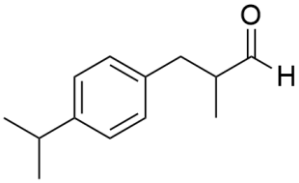	glutaraldehyde 10%	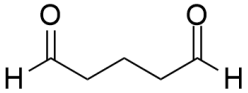
butanal 35%	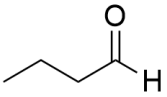		

Δ19*Tf*NCS primary sequence

MGSS**HHHHHH**SSG**LVPRGS**HMQKLILTGRPFLHHQGIINQVSTVTKVIHHELEVAAS
ADDIWTVYSWPGLAKHLPDLLPGAFEKLEIIGDGGVGTILDMTFVPGEFPHEYKEKFI
LVDNEHRLKKVQMIEGGYLDLGVTYYMDTIHVVPTGKDSCVIKSSTEYHVKPEFVKI
VEPLITTGPLAAMADAISKLVLEHKSKSNSDEIEAAIITV

His-tag: Blue site

Thrombin cleavage site: Red site

Expasy ProtParam tool results for the sequence above:

Number of amino acids: 212

Theoretical pI: 6.07

Molecular weight: 23433.95

Amino acid composition:

Residue	N° of residues	Percentage
Ala (A)	11	5.2%
Arg (R)	3	1.4%
Asn (N)	3	1.4%
Asp (D)	11	5.2%
Cys (C)	1	0.5%
Gln (Q)	4	1.9%
Glu (E)	15	7.1%
Gly (G)	17	8.0%
His (H)	17	8.0%
Ile (I)	18	8.5%

Leu (L)	19	9.0%
Lys (K)	15	7.1%
Met (M)	6	2.8%
Phe (F)	6	2.8%
Pro (P)	11	5.2%
Ser (S)	15	7.1%
Thr (T)	13	6.1%
Trp (W)	2	0.9%
Tyr (Y)	6	2.8%
Val (V)	19	9.0%
Pyl (O)	0	0.0%
Sec (U)	0	0.0%

Total number of negatively charged residues (Asp + Glu): 26

Total number of positively charged residues (Arg + Lys): 18

Atomic composition:

Carbon C 1060

Hydrogen H 1661

Nitrogen N 279

Oxygen O 306

Sulfur S 7

Formula: $C_{1060}H_{1661}N_{279}O_{306}S_7$

Total number of atoms: 3313

Extinction coefficients:

Extinction coefficients are in units of M^{-1} cm^{-1}, at 280 nm measured in water.

Ext. coefficient 19940

Abs 0.1% (=1 g/l) 0.851, assuming all pairs of Cys residues form cystines

Ext. coefficient 19940

Abs 0.1% (=1 g/l) 0.851, assuming all Cys residues are reduced

Estimated half-life:

The N-terminal of the sequence considered is M (Met).

The estimated half-life is: 30 hours (mammalian reticulocytes, in vitro).

>20 hours (yeast, in vivo).

>10 hours (Escherichia coli, in vivo).

Instability index:

The instability index (II) is computed to be 25.91

This classifies the protein as stable.

Aliphatic index: 99.25

Grand average of hydropathicity (GRAVY): -0.064

Reactants ^{1}H NMR spectra

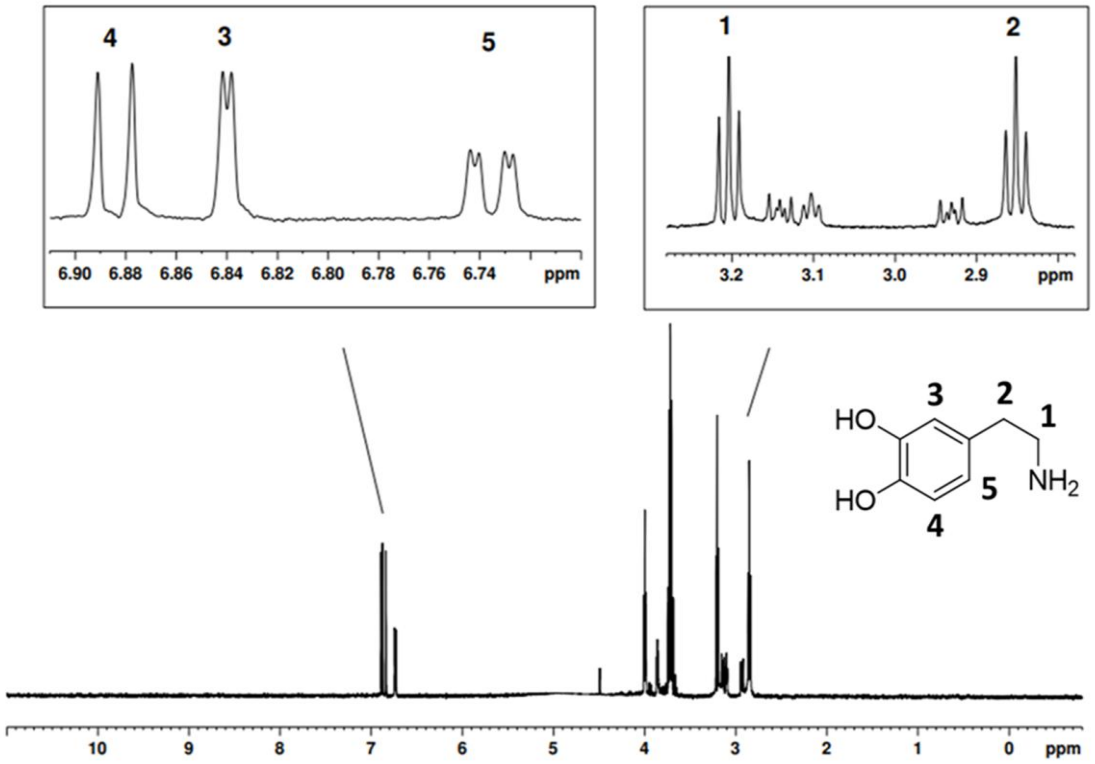

Figure A2. ^{1}H NMR spectrum (600 MHz, 298.1 K) of 2.5 mM dopamine in 1 M phosphate buffer (pH 7.0) containing 5 mM ascorbic acid and 10% D_2O (v/v). The spectrum was acquired on a Bruker Avance Neo spectrometer using the p3919gp pulse sequence with 128 scans, 4 dummy scans, and a 1.2 s recovery time. Key regions are expanded to show aromatic protons (H-3, H-4, H-5) and aliphatic protons (H-1, H-2).

Table A5: ^{1}H NMR Chemical Shifts and Coupling Constants of Dopamine in Phosphate Buffer (pH 7.0).

Hydrogen	Chemical shift (ppm)	Signal multiplicity	Integral	Coupling constant (Hz)
1	3.20	Triplet	1 H	7.4
2	2.85	Triplet	1 H	7.4

3	6.84	Duplet	1 H	2.0
4	6.88	Duplet	2 H	8.1
5	6.74	Double duplet	2 H	8.1; 2.0

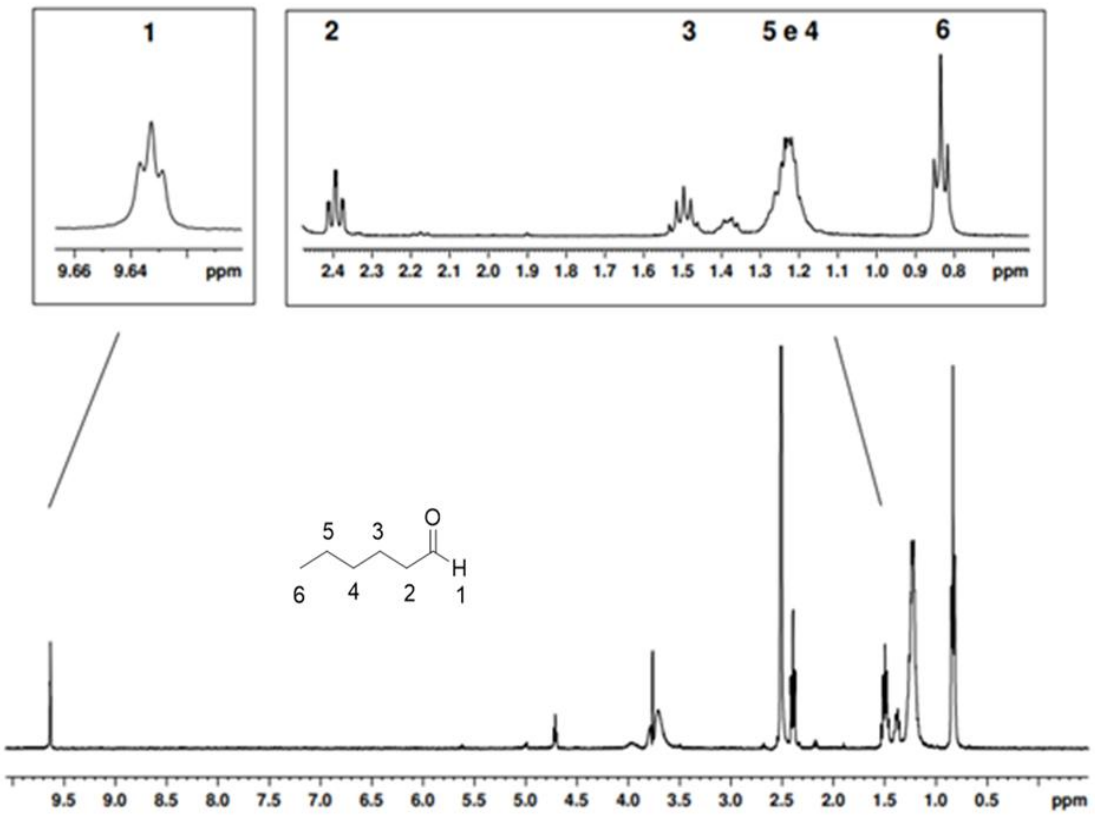

Figure A3. ^{1}H NMR spectrum (400 MHz, 298.1 K) of 2.5 mM hexanal in 90% DMSO/10% D_2O (v/v). Acquired on a Bruker NanoBay spectrometer using the p3919gp pulse sequence (128 scans, 4 dummy scans, 1.2 s recovery time).

Table A6. ^{1}H NMR Chemical Shifts and Coupling Constants of hexanal in Phosphate Buffer (pH 7.0).

Hydrogen	**Chemical shift (ppm)**	**Signal multiplicity**	**Integral**	**Coupling constant (Hz)**
1	9.63	Triplet	1 H	1.6
2	2.39	Triple duplet	2 H	7.2; 1.6

3	1.5	Quintuplet	2 H	7.2
4 and 5	1.23	Multiplet	4 H	-
6	0.83	Triplet	3 H	6.9

Solid support selection - ^{1}H NMR spectra

The spectra were acquired at 298.1 K on a Bruker NanoBay 400 MHz spectrometer using the p3919gp pulse sequence with the following parameters: 128 scans, 4 dummy scans, and a 1.2 s recovery time. Signal broadening was observed in the spectral regions corresponding to dopamine and hexanal. Samples were prepared by homogenizing dopamine, hexanal, and the solid support for 2 hours.

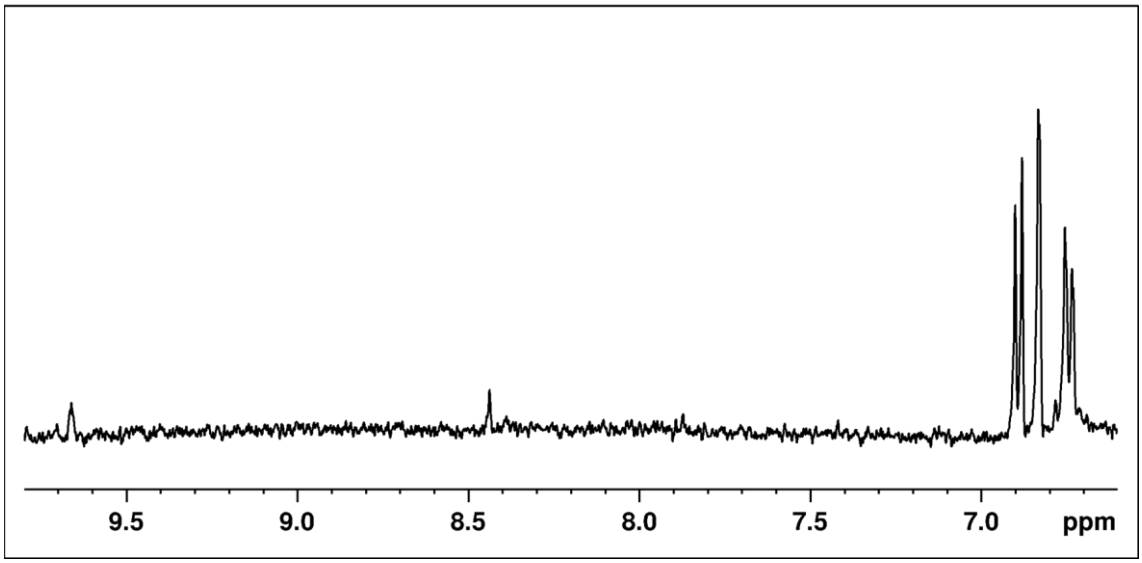

Figure A4. ^{1}H NMR spectrum (400 MHz, 298 K) of a sample containing 2.5 mM dopamine and 2.5 mM hexanal with silica gel (without Δ19*Tf*NCS) in 50 mM HEPES buffer (pH 7.0), 5 mM ascorbic acid, and 10% D_2O (v/v).

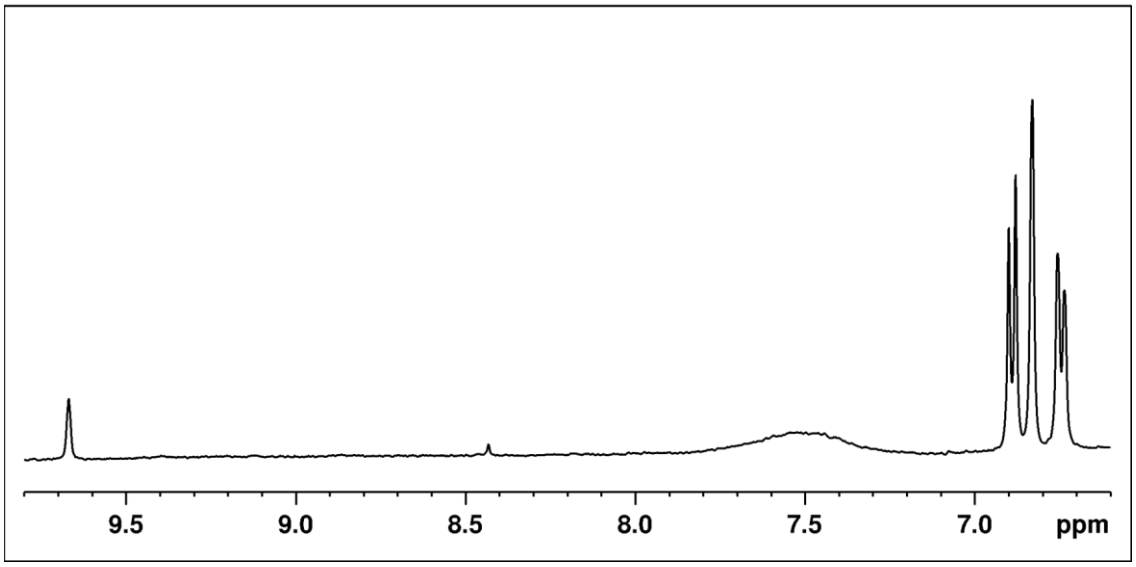

Figure A5. ^{1}H NMR spectrum (400 MHz, 298 K) of a sample containing 2.5 mM dopamine and 2.5 mM hexanal with Dowex 1X8 (without Δ19*Tf*NCS) in 50 mM HEPES buffer (pH 7.0), 5 mM ascorbic acid, and 10% D_2O (v/v).

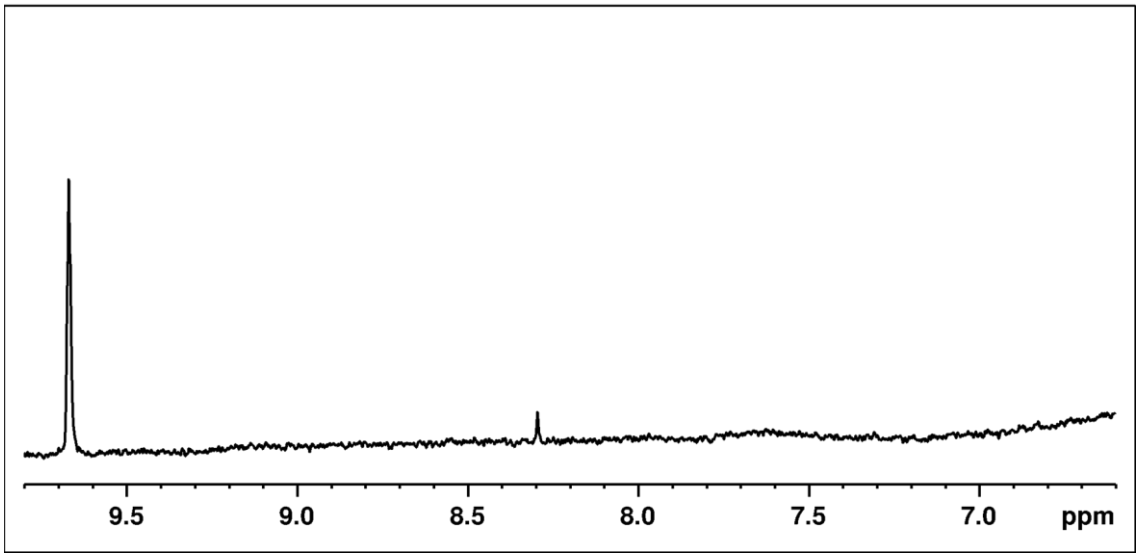

Figure A6. ^{1}H NMR spectrum (400 MHz, 298 K) of a sample containing 2.5 mM dopamine and 2.5 mM hexanal with Dowex 50WX8 (without Δ19*Tf*NCS) in 50 mM HEPES buffer (pH 7.0), 5 mM ascorbic acid, and 10% D_2O (v/v).

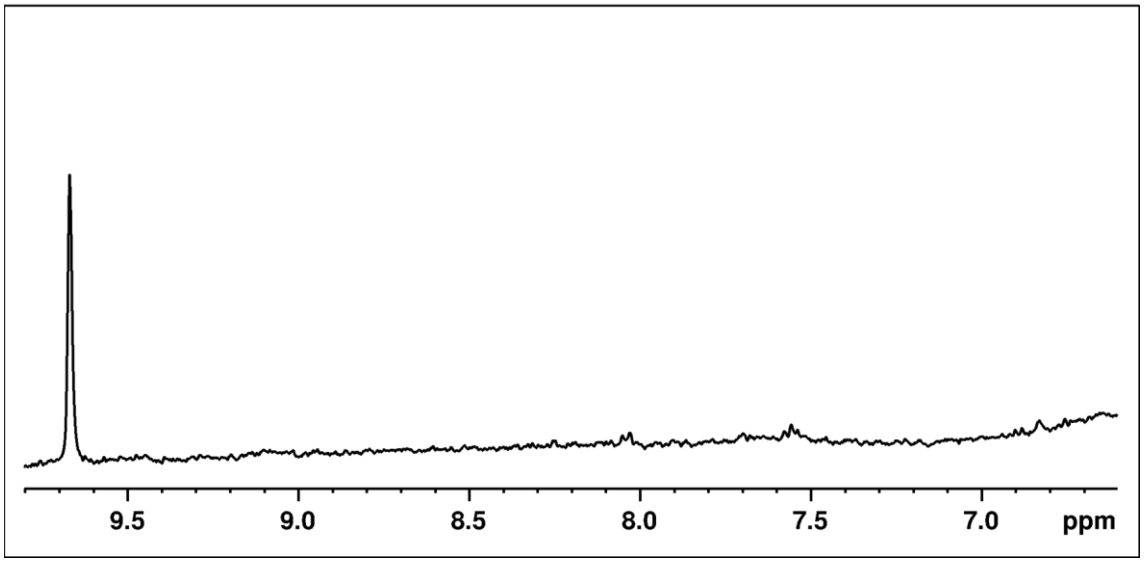

Figure A7. ^{1}H NMR spectrum (400 MHz, 298 K) of a sample containing 2.5 mM dopamine and 2.5 mM hexanal with Dowex 50WX4 (without Δ19*Tf*NCS) in 50 mM HEPES buffer (pH 7.0), 5 mM ascorbic acid, and 10% D_2O (v/v).

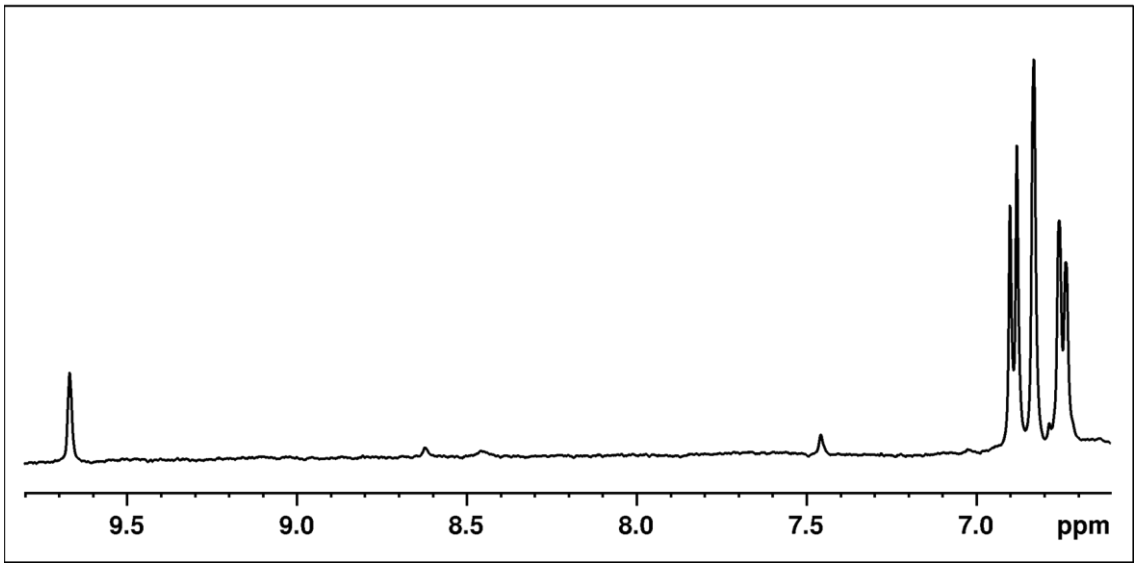

Figure A8. ^{1}H NMR spectrum (400 MHz, 298 K) of a sample containing 2.5 mM dopamine and 2.5 mM hexanal with kaolin (without Δ19TfNCS) in 50 mM HEPES buffer (pH 7.0), 5 mM ascorbic acid, and 10% D_2O (v/v).

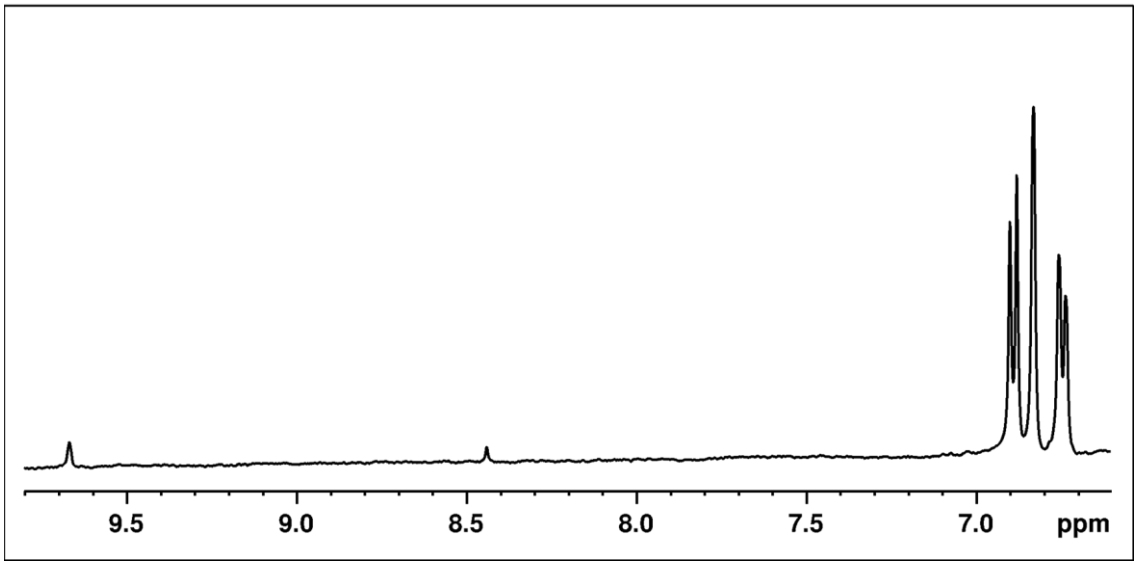

Figure A9 ^{1}H NMR spectrum (400 MHz, 298 K) of a sample containing 2.5 mM dopamine and 2.5 mM hexanal with Diaion HP-2MG (without Δ19*Tf*NCS) in 50 mM HEPES buffer (pH 7.0), 5 mM ascorbic acid, and 10% D_2O (v/v).

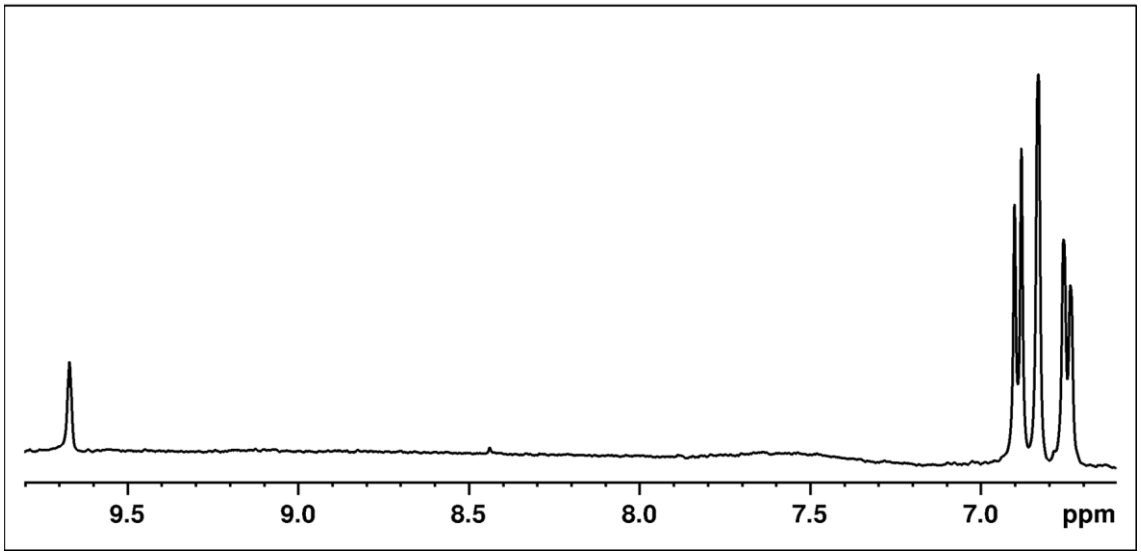

Figure A10. ^{1}H NMR spectrum (400 MHz, 298 K) of a sample containing 2.5 mM dopamine and 2.5 mM hexanal with Celite 545 (without Δ19*Tf*NCS) in 50 mM HEPES buffer (pH 7.0), 5 mM ascorbic acid, and 10% D_2O (v/v).

Reaction samples - ^{1}H NMR spectra

The spectra were acquired at 298.1 K on a Bruker Avance Neo 600 MHz spectrometer using the noesygppr1d pulse sequence with the following parameters: 64 scans, 8 dummy scans, and a 20 s recovery time. The figures show an expanded view of the aromatic region displaying: Protons H-3, H-4, and H-5 of dopamine and Protons H-3' and H-4' of the product 1-pentyl-1,2,3,4-tetrahydroisoquinoline-6,7-diol

First cycle (37°C)

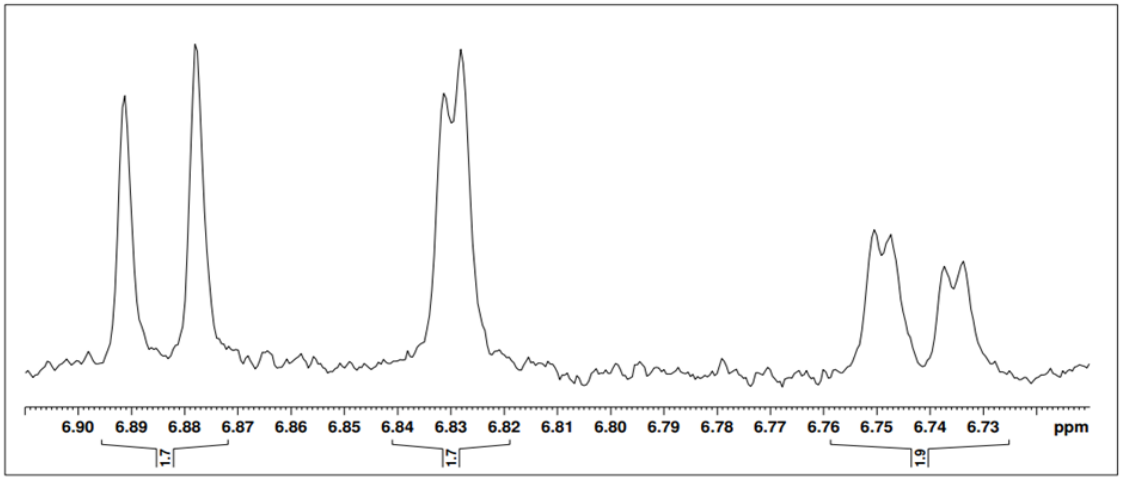

Figure A11. Spectrum of the control sample (control 1) at 37°C. ^{1}H NMR spectrum obtained from a sample containing 0.25 mM dopamine and 2.5 mM hexanal, in 50 mM HEPES buffer, pH 7.4 with 5 mM ascorbic acid, 10% DMSO, 10% v/v D_2O and dss 139 µM.

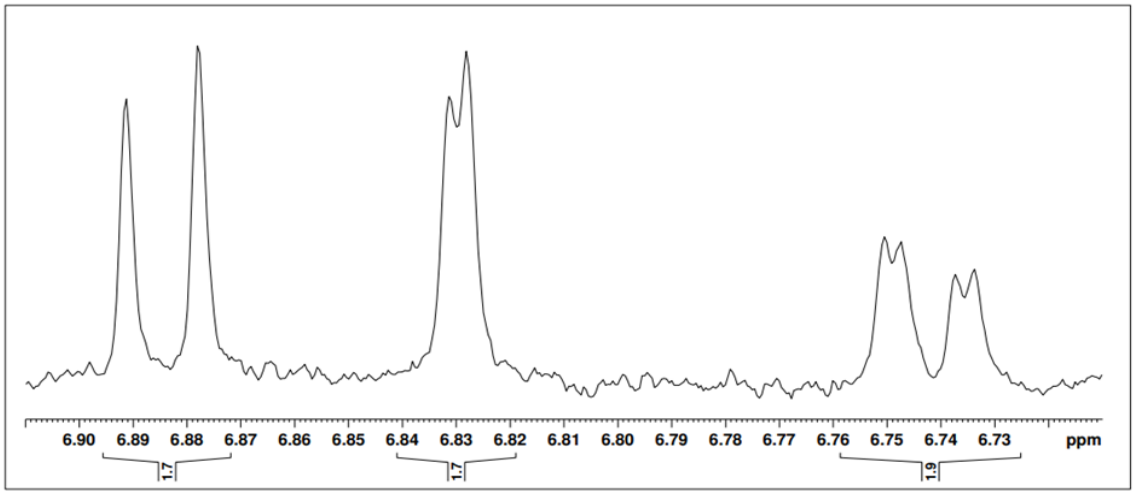

Figure A12. Spectrum of the control sample (control 2) at 37°C. ^{1}H NMR spectrum obtained from a sample containing 0.25 mM dopamine and 2.5 mM hexanal, in 50 mM HEPES buffer, pH 7.4 with 5 mM ascorbic acid, 10% DMSO, 10% v/v D_2O and dss 139 µM.

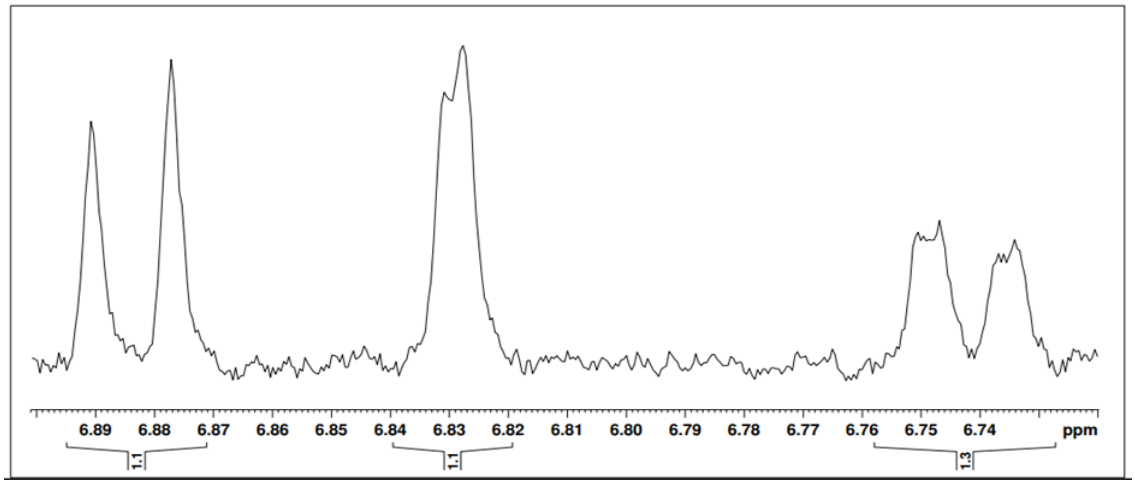

Figure A13. Spectrum of the control sample (control 3) at 37°C. ^{1}H NMR spectrum obtained from a sample containing 0.25 mM dopamine and 2.5 mM hexanal, in 50 mM HEPES buffer, pH 7.4 with 5 mM ascorbic acid, 10% DMSO, 10% v/v D_2O and dss 139 µM.

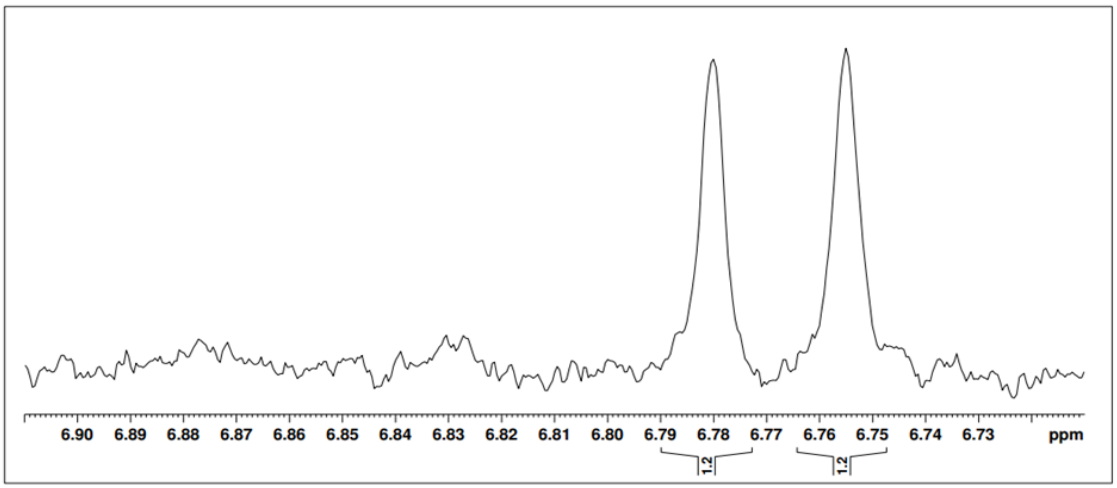

Figure A14. Spectrum of the non-immobilized Δ19*Tf*NCS-catalyzed reaction at 37°C. ^{1}H NMR spectrum obtained from a reaction sample between 0.25 mM dopamine and 2.5 mM hexanal catalyzed by non-immobilized Δ19*Tf*NCS, in 50 mM HEPES buffer, pH 7.4 with 5 mM ascorbic acid, 10% DMSO, 10% v/v D_2O and dss 139 µM.

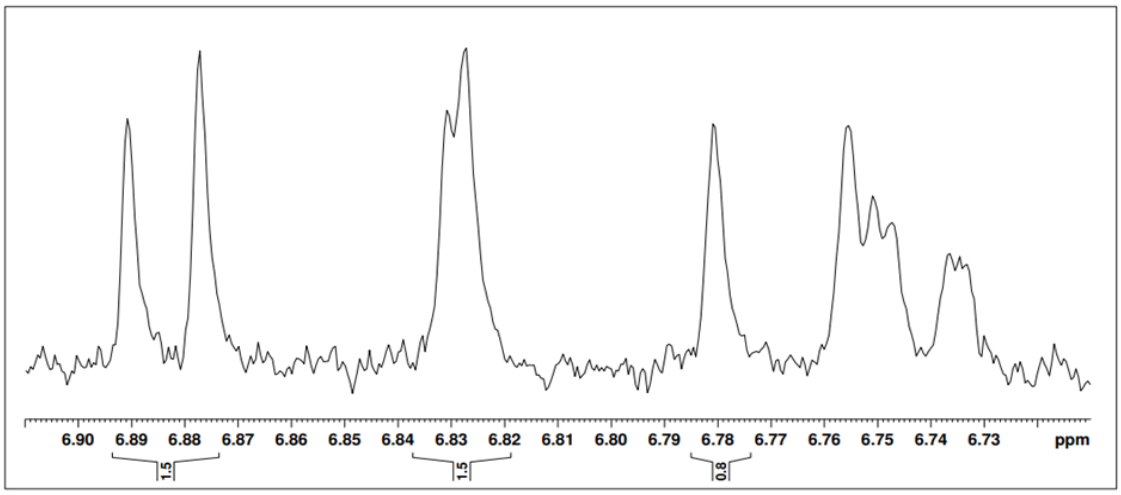

Figure A15. Spectrum of the Δ19*Tf*NCS immobilized in kaolin catalyzed reaction sample (Kaolin 1) at 37°C. ^{1}H NMR spectrum obtained from a reaction sample between 0.25 mM dopamine and 2.5 mM hexanal catalyzed by Δ19*Tf*NCS immobilized in Kaolin, in 50 mM HEPES buffer, pH 7.4 with 5 mM ascorbic acid, 10% DMSO, 10% v/v D_2O and dss 139 µM.

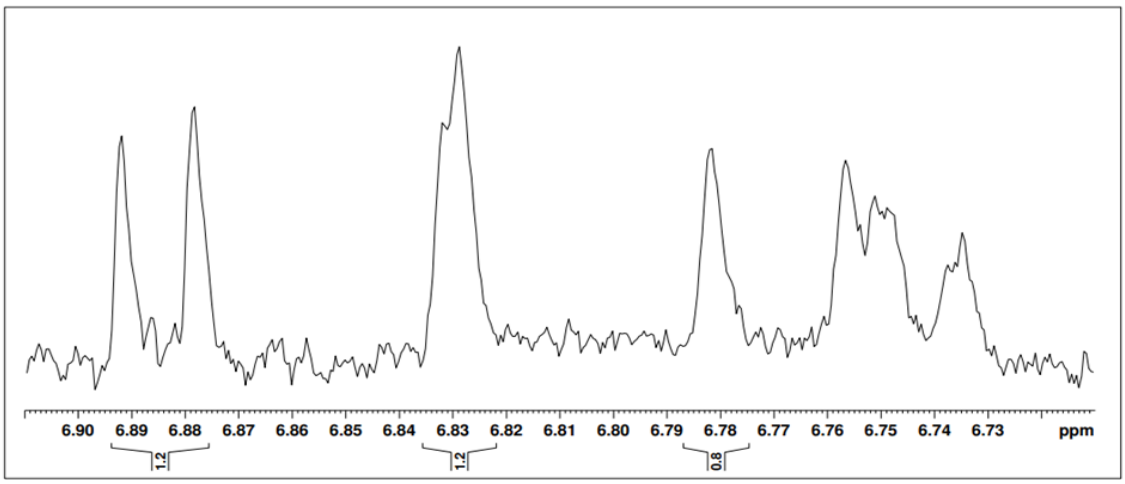

Figure A16. Spectrum of the Δ19*Tf*NCS immobilized in kaolin catalyzed reaction sample (Kaolin 2) at 37°C. ^{1}H NMR spectrum obtained from a reaction sample between 0.25 mM dopamine and 2.5 mM hexanal catalyzed by Δ19*Tf*NCS immobilized in Kaolin, in 50 mM HEPES buffer, pH 7.4 with 5 mM ascorbic acid, 10% DMSO, 10% v/v D_2O and dss 139 µM.

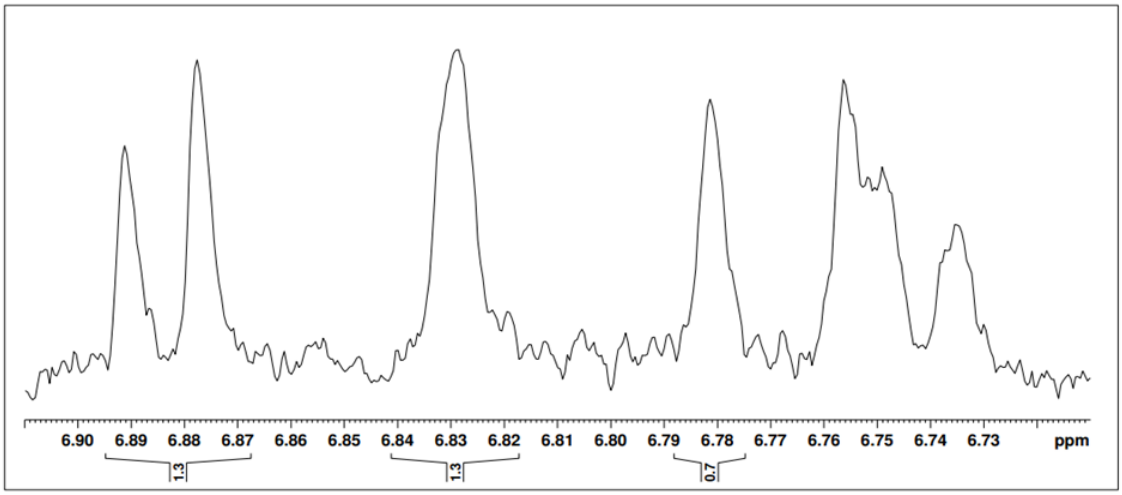

Figure A17. Spectrum of the Δ19*Tf*NCS immobilized in kaolin catalyzed reaction sample (Kaolin 3) at 37°C. ^{1}H NMR spectrum obtained from a reaction sample between 0.25 mM dopamine and 2.5 mM hexanal catalyzed by Δ19*Tf*NCS immobilized in Kaolin, in 50 mM HEPES buffer, pH 7.4 with 5 mM ascorbic acid, 10% DMSO, 10% v/v D_2O and dss 139 µM.

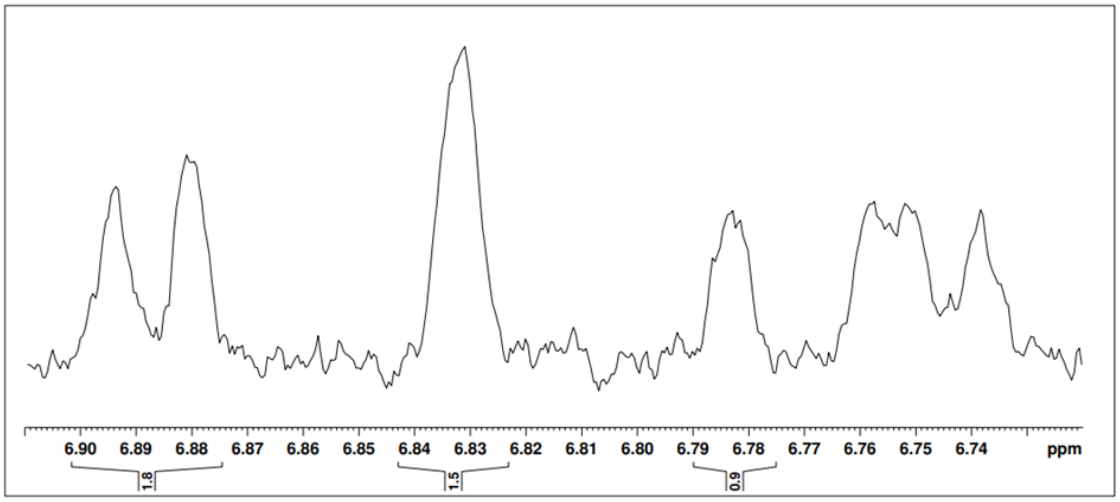

Figure A18. Spectrum of Δ19*Tf*NCS immobilized in celite 545 catalyzed reaction sample (Celite 1) at 37°C. ^{1}H NMR spectrum obtained from a reaction sample between 0.25 mM dopamine and 2.5 mM hexanal catalyzed by Δ19*Tf*NCS immobilized in celite 545, in 50 mM HEPES buffer, pH 7.4 with 5 mM ascorbic acid, 10% DMSO, 10% v/v D_2O and dss 139 µM.

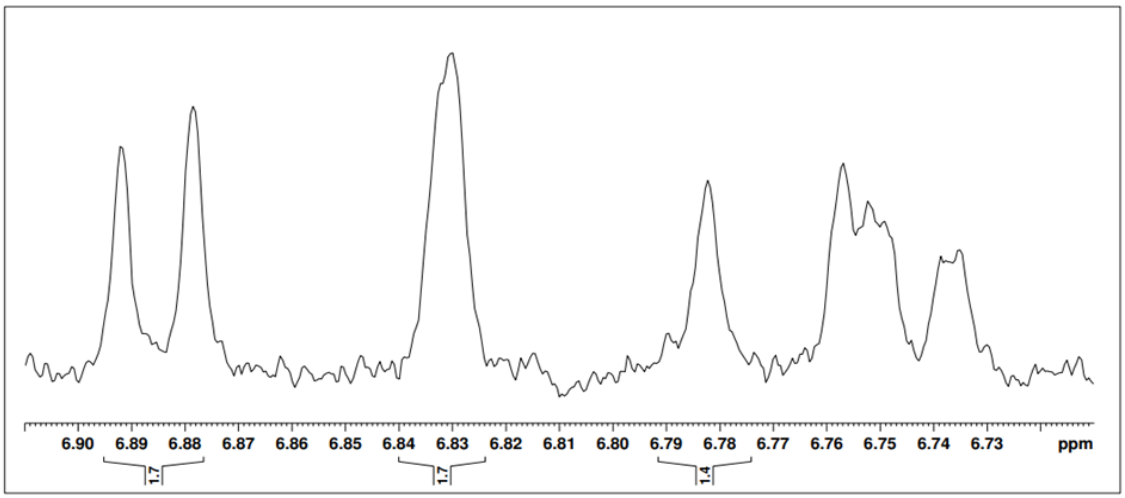

Figure A19. Spectrum of Δ19*Tf*NCS immobilized in celite 545 catalyzed reaction sample (Celite 2) at 37°C. ^{1}H NMR spectrum obtained from a reaction sample between 0.25 mM dopamine and 2.5 mM hexanal catalyzed by Δ19*Tf*NCS immobilized in celite 545, in 50 mM HEPES buffer, pH 7.4 with 5 mM ascorbic acid, 10% DMSO, 10% v/v D_2O and dss 139 µM.

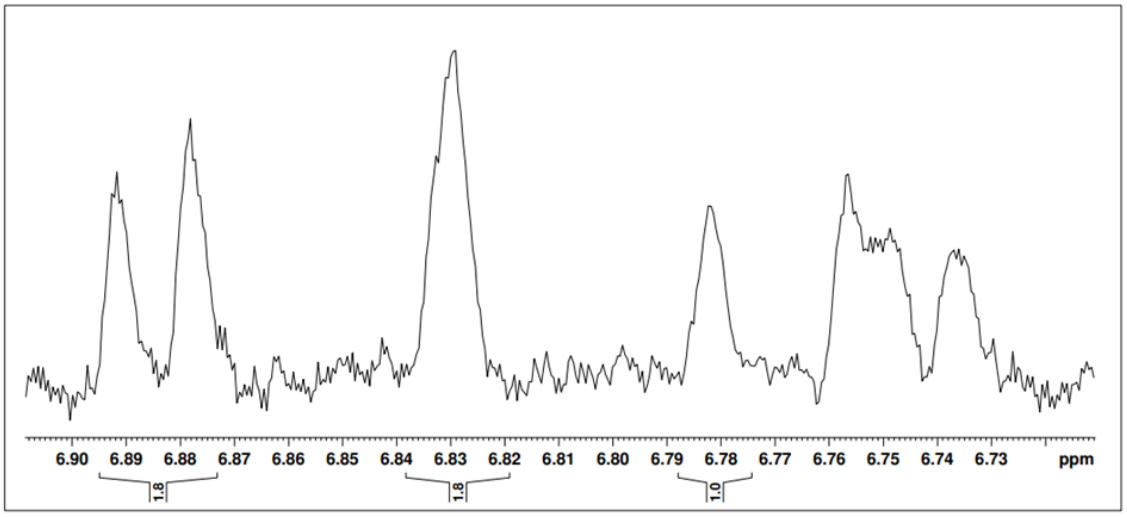

Figure A20. Spectrum of Δ19*Tf*NCS immobilized in celite 545 catalyzed reaction sample (Celite 3) at 37°C. ^{1}H NMR spectrum obtained from a reaction sample between 0.25 mM dopamine and 2.5 mM hexanal catalyzed by Δ19*Tf*NCS immobilized in celite 545, in 50 mM HEPES buffer, pH 7.4 with 5 mM ascorbic acid, 10% DMSO, 10% v/v D_2O and dss 139 µM.

Second cycle (37°C)

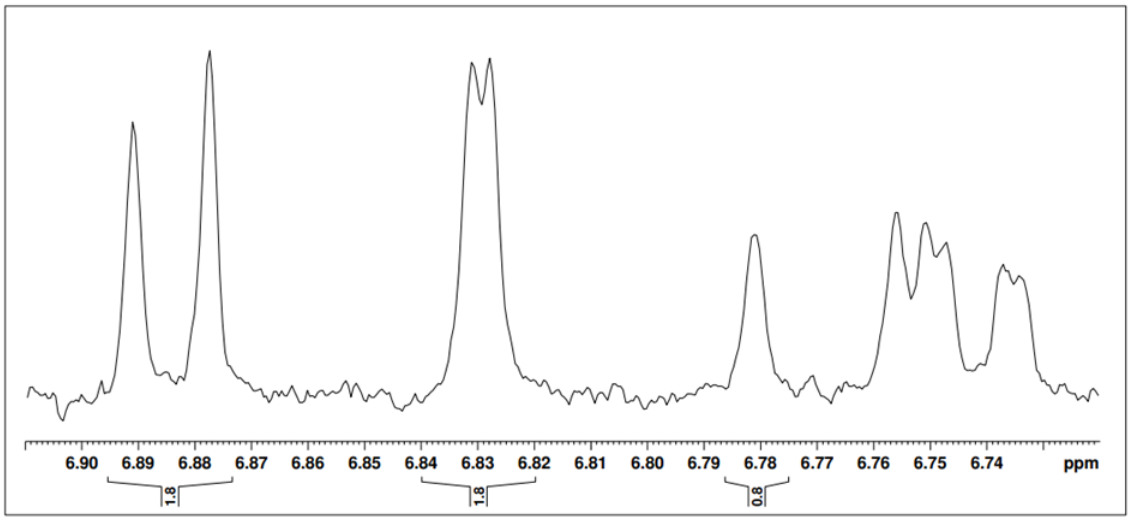

Figure A21. Spectrum of Δ19*Tf*NCS immobilized in kaolin catalyzed reaction sample (kaolin 1) second cycle at 37°C. ^{1}H NMR spectrum obtained from a reaction sample between 0.25 mM

dopamine and 2.5 mM hexanal catalyzed by Δ19*Tf*NCS immobilized in kaolin, in 50 mM HEPES buffer, pH 7.4 with 5 mM ascorbic acid, 10% DMSO, 10% v/v D_2O and dss 139 µM.

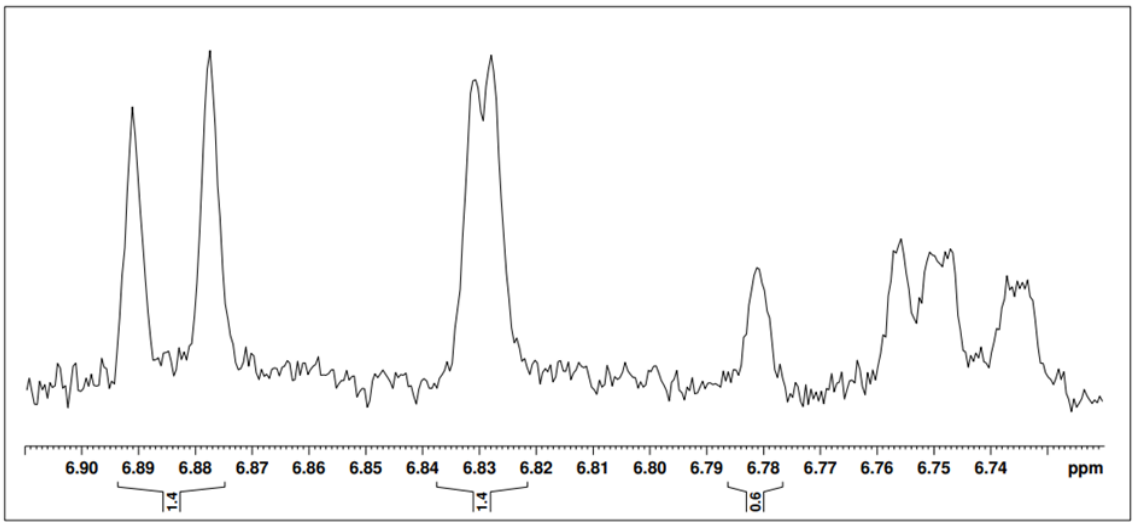

Figure A22. Spectrum of Δ19*Tf*NCS immobilized in kaolin catalyzed reaction sample (kaolin 2) second cycle at 37°C. ^{1}H NMR spectrum obtained from a reaction sample between 0.25 mM dopamine and 2.5 mM hexanal catalyzed by Δ19*Tf*NCS immobilized in kaolin, in 50 mM HEPES buffer, pH 7.4 with 5 mM ascorbic acid, 10% DMSO, 10% v/v D_2O and dss 139 µM.

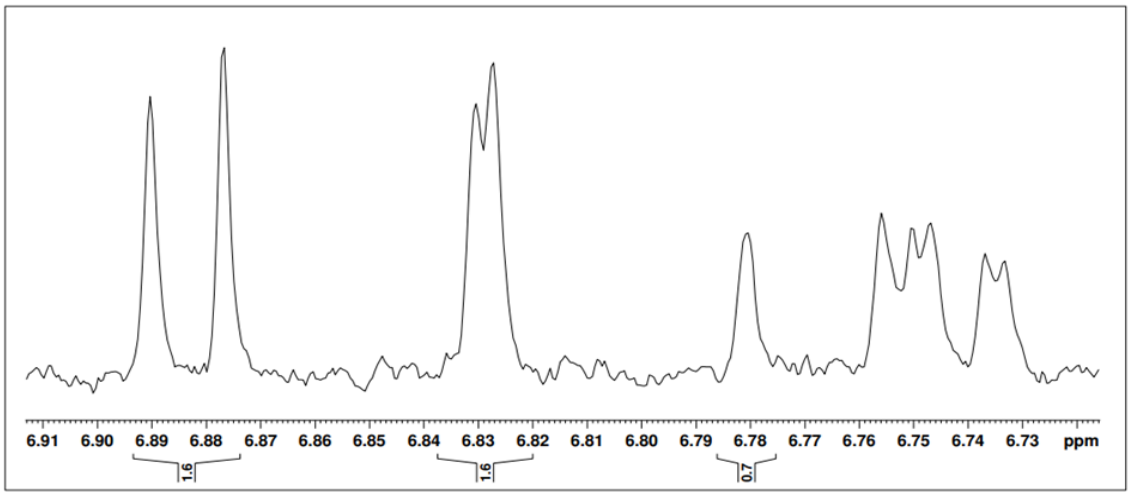

Figure A23. Spectrum of Δ19*Tf*NCS immobilized in kaolin catalyzed reaction sample (kaolin 3) second cycle at 37°C. ^{1}H NMR spectrum obtained from a reaction sample between 0.25 mM dopamine and 2.5 mM hexanal catalyzed by Δ19*Tf*NCS immobilized in kaolin, in 50 mM HEPES buffer, pH 7.4 with 5 mM ascorbic acid, 10% DMSO, 10% v/v D_2O and dss 139 µM.

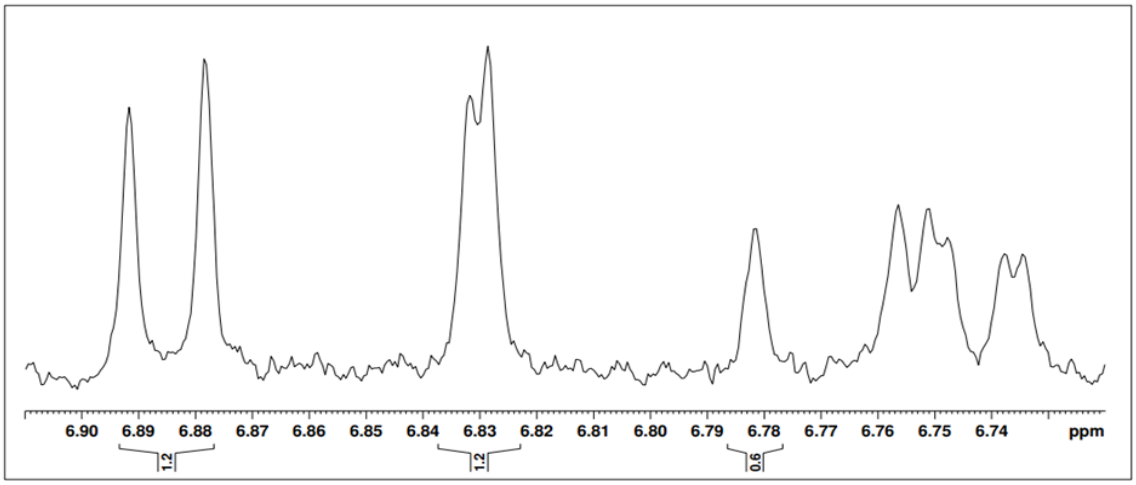

Figure A24. Spectrum of Δ19*Tf*NCS immobilized in celite 545 catalyzed reaction sample (Celite 1) second cycle at 37°C. ^{1}H NMR spectrum obtained from a reaction sample between 0.25 mM dopamine and 2.5 mM hexanal catalyzed by Δ19*Tf*NCS immobilized in celite 545, in 50 mM HEPES buffer, pH 7.4 with 5 mM ascorbic acid, 10% DMSO, 10% v/v D_2O and dss 139 μM.

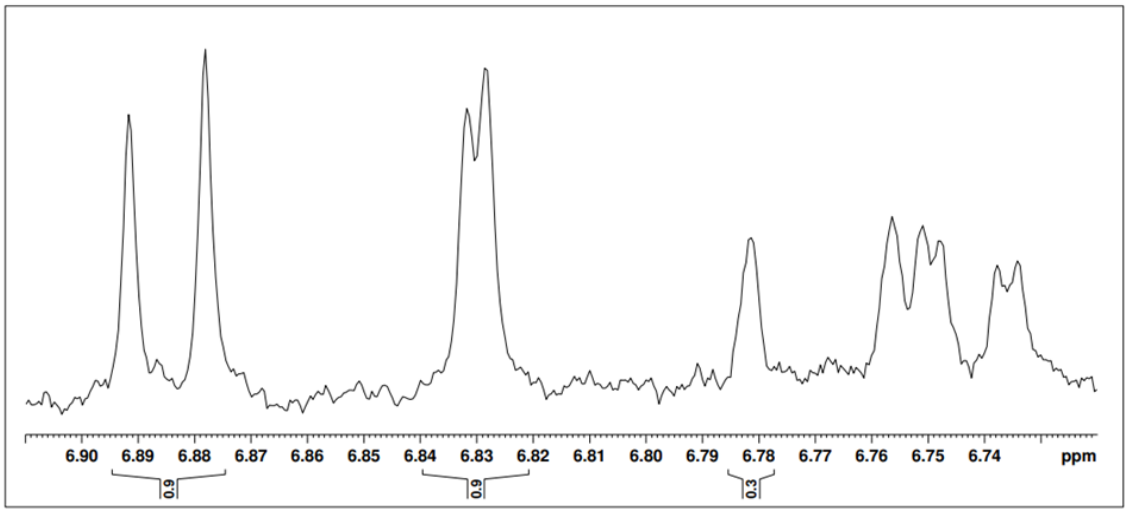

Figure A25. Spectrum of Δ19*Tf*NCS immobilized in celite 545 catalyzed reaction sample (Celite 2) second cycle at 37°C. ^{1}H NMR spectrum obtained from a reaction sample between 0.25 mM dopamine and 2.5 mM hexanal catalyzed by Δ19*Tf*NCS immobilized in celite 545, in 50 mM HEPES buffer, pH 7.4 with 5 mM ascorbic acid, 10% DMSO, 10% v/v D_2O and dss 139 μM.

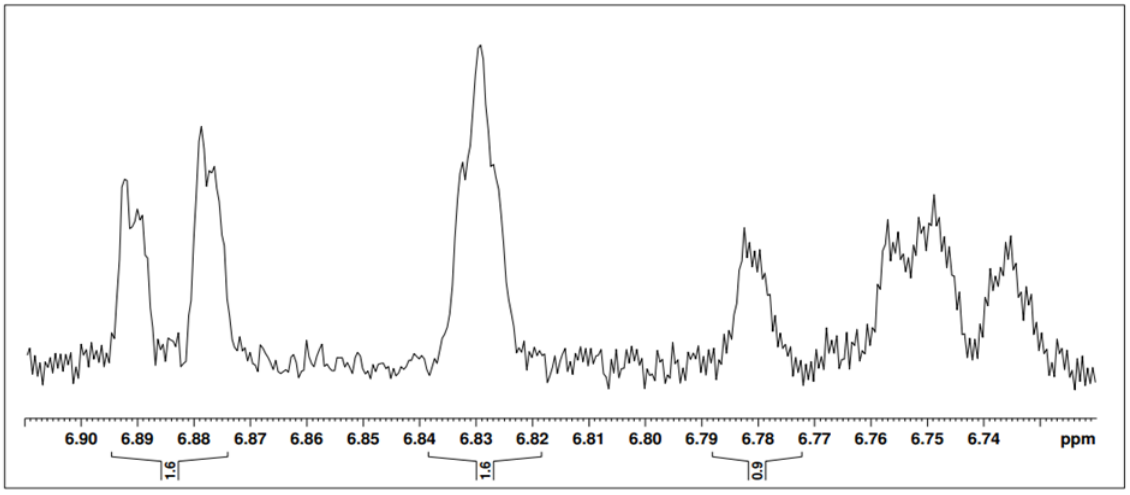

Figure A26. Spectrum of Δ19*Tf*NCS immobilized in celite 545 catalyzed reaction sample (Celite 3) second cycle at 37°C. ^{1}H NMR spectrum obtained from a reaction sample between 0.25 mM dopamine and 2.5 mM hexanal catalyzed by Δ19*Tf*NCS immobilized in celite 545, in 50 mM HEPES buffer, pH 7.4 with 5 mM ascorbic acid, 10% DMSO, 10% v/v D_2O and dss 139 μM.

Third cycle

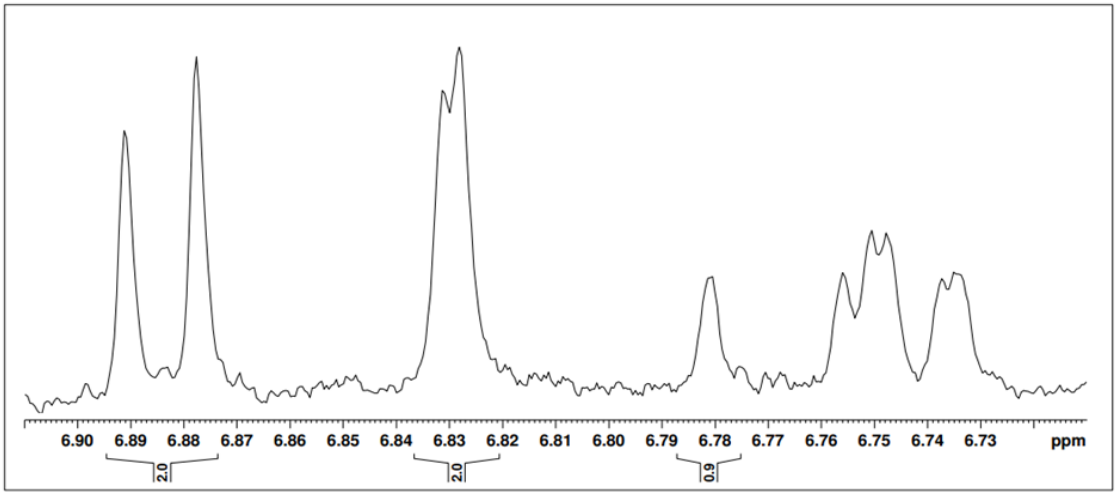

Figure A27. Spectrum of Δ19*Tf*NCS immobilized in kaolin catalyzed reaction sample (Kaolin 1) third cycle at 37°C. ^{1}H NMR spectrum obtained from a reaction sample between 0.25 mM

dopamine and 2.5 mM hexanal catalyzed by Δ19*Tf*NCS immobilized in kaolin, in 50 mM HEPES buffer, pH 7.4 with 5 mM ascorbic acid, 10% DMSO, 10% v/v D_2O and dss 139 µM.

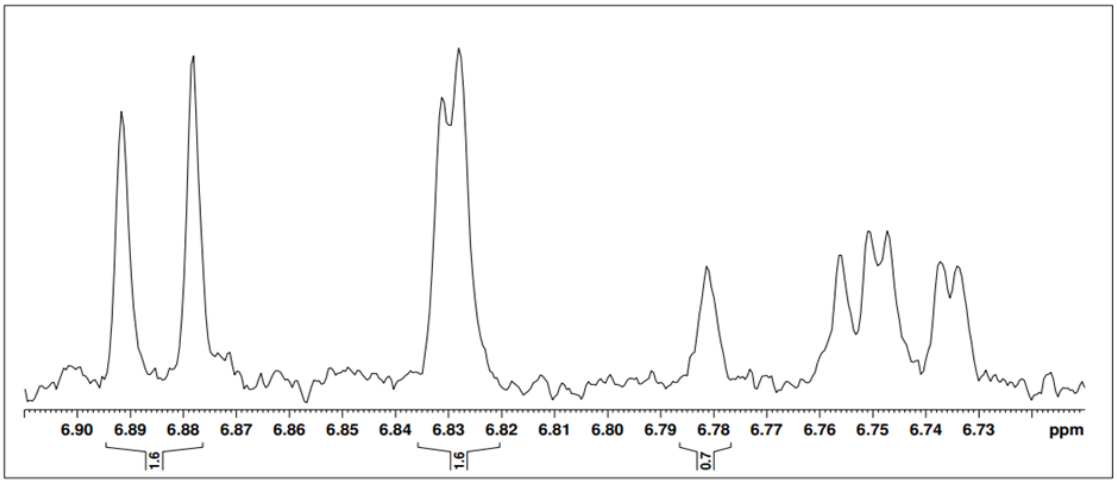

Figure A28. Spectrum of Δ19*Tf*NCS immobilized in kaolin catalyzed reaction sample (Kaolin 2) third cycle at 37°C. ^{1}H NMR spectrum obtained from a reaction sample between 0.25 mM dopamine and 2.5 mM hexanal catalyzed by Δ19*Tf*NCS immobilized in kaolin, in 50 mM HEPES buffer, pH 7.4 with 5 mM ascorbic acid, 10% DMSO, 10% v/v D_2O and dss 139 µM.

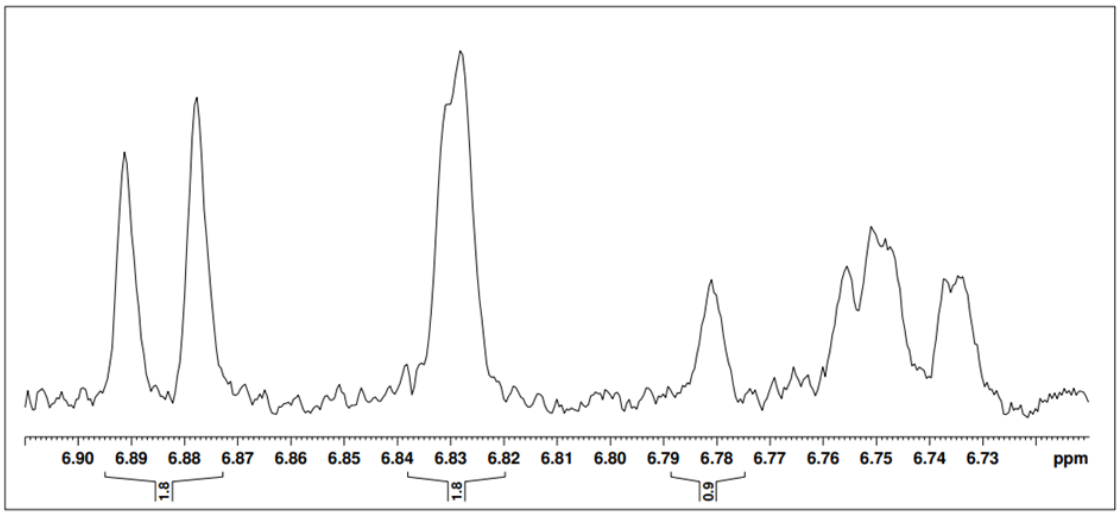

Figure A29. Spectrum of Δ19*Tf*NCS immobilized in kaolin catalyzed reaction sample (Kaolin 3) third cycle at 37°C. ^{1}H NMR spectrum obtained from a reaction sample between 0.25 mM dopamine and 2.5 mM hexanal catalyzed by Δ19*Tf*NCS immobilized in kaolin, in 50 mM HEPES buffer, pH 7.4 with 5 mM ascorbic acid, 10% DMSO, 10% v/v D_2O and dss 139 µM.

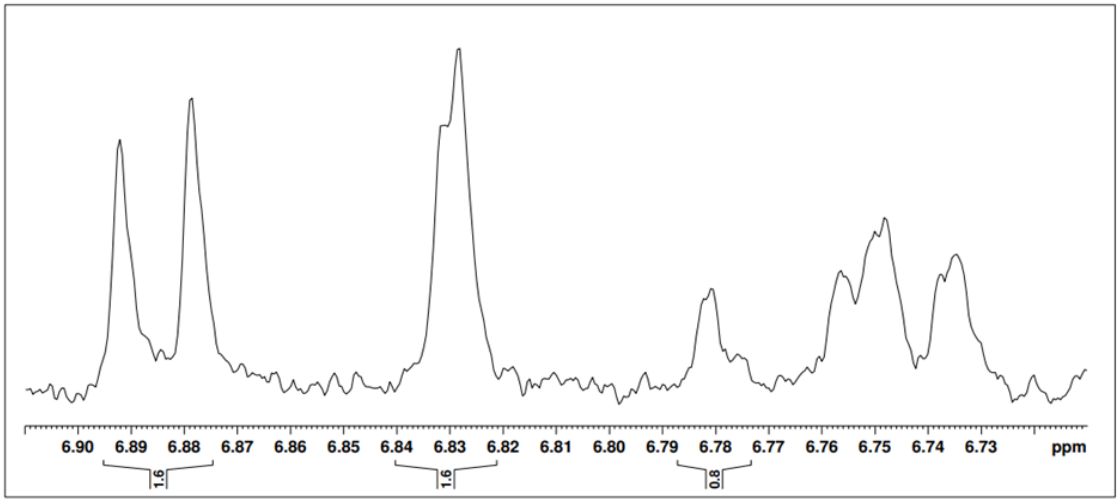

Figure A30. Spectrum of Δ19*Tf*NCS immobilized in celite 545 catalyzed reaction sample (Celite 1) third cycle at 37°C. ^{1}H NMR spectrum obtained from a reaction sample between 0.25 mM dopamine and 2.5 mM hexanal catalyzed by Δ19*Tf*NCS immobilized in celite 545, in 50 mM HEPES buffer, pH 7.4 with 5 mM ascorbic acid, 10% DMSO, 10% v/v D_2O and dss 139 μM.

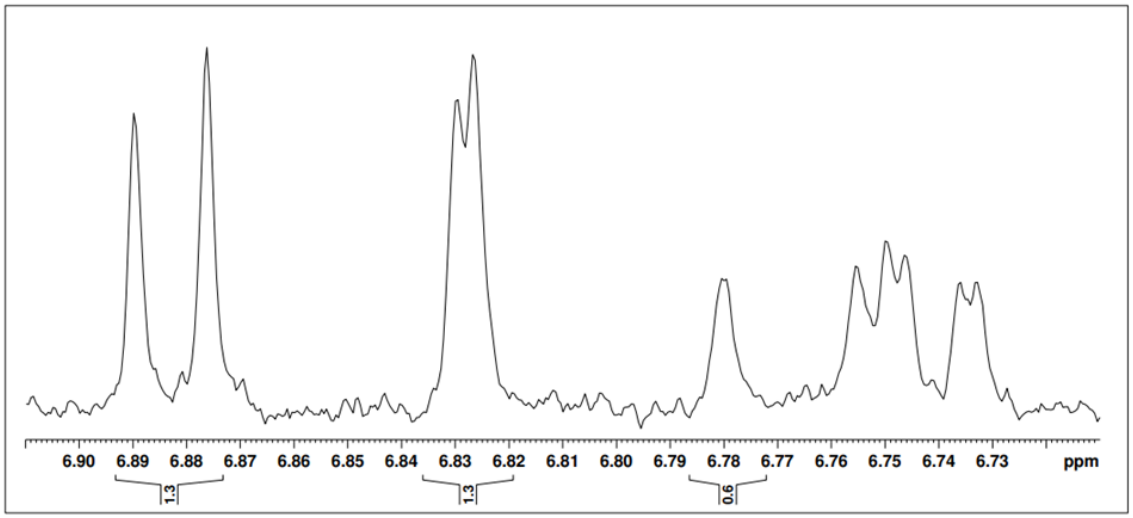

Figure A31. Spectrum of Δ19*Tf*NCS immobilized in celite 545 catalyzed reaction sample (Celite 2) third cycle at 37°C. ^{1}H NMR spectrum obtained from a reaction sample between 0.25 mM dopamine and 2.5 mM hexanal catalyzed by Δ19*Tf*NCS immobilized in celite 545, in 50 mM HEPES buffer, pH 7.4 with 5 mM ascorbic acid, 10% DMSO, 10% v/v D_2O and dss 139 μM.

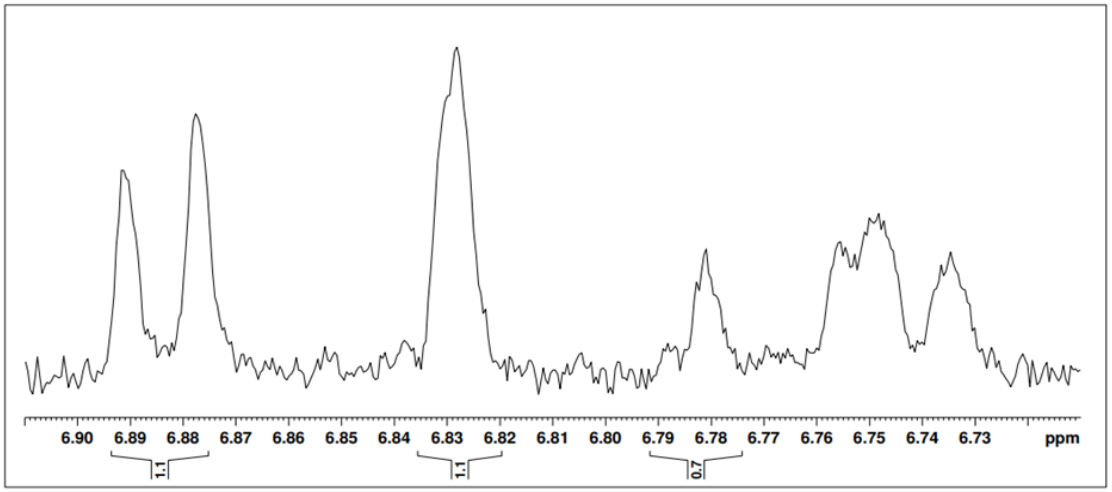

Figure A32. Spectrum of Δ19*Tf*NCS immobilized in celite 545 catalyzed reaction sample (Celite 3) third cycle at 37°C. ^{1}H NMR spectrum obtained from a reaction sample between 0.25 mM dopamine and 2.5 mM hexanal catalyzed by Δ19*Tf*NCS immobilized in celite 545, in 50 mM HEPES buffer, pH 7.4 with 5 mM ascorbic acid, 10% DMSO, 10% v/v D_2O and dss 139 μM.

Reactions at 47°C

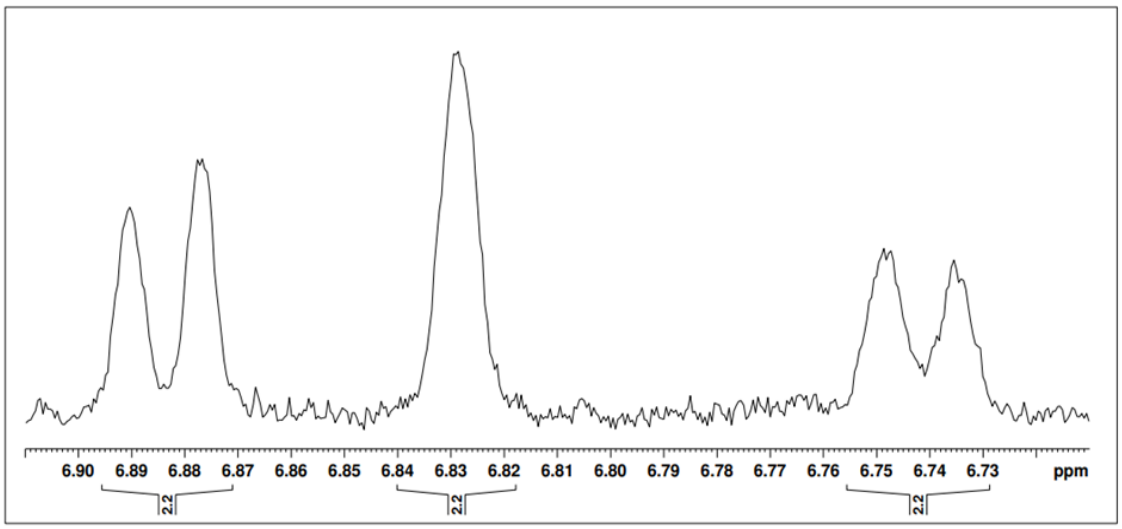

Figure A33. Spectrum of the control sample (control 1) at 47°C. ^{1}H NMR spectrum obtained from a sample containing 0.25 mM dopamine and 2.5 mM hexanal (homogenized at 47°C for

1 h), in 50 mM HEPES buffer, pH 7.4 with 5 mM ascorbic acid, 10% DMSO, 10% v/v D_2O and dss 139 µM.

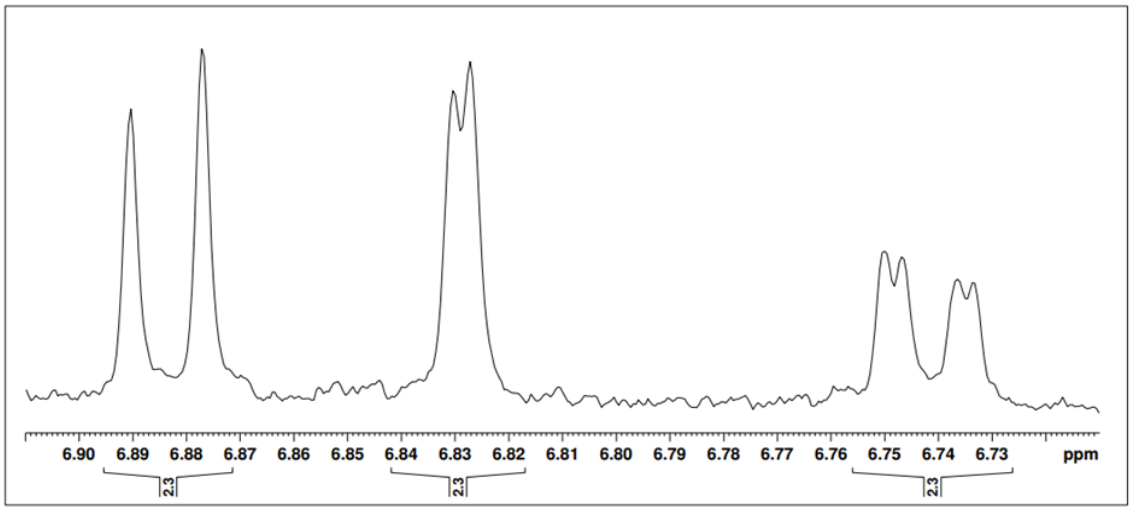

Figure A34. Spectrum of the control sample (control 2) at 47°C. ^1H NMR spectrum obtained from a sample containing 0.25 mM dopamine and 2.5 mM hexanal (homogenized at 47°C for 1 h), in 50 mM HEPES buffer, pH 7.4 with 5 mM ascorbic acid, 10% DMSO, 10% v/v D_2O and dss 139 µM.

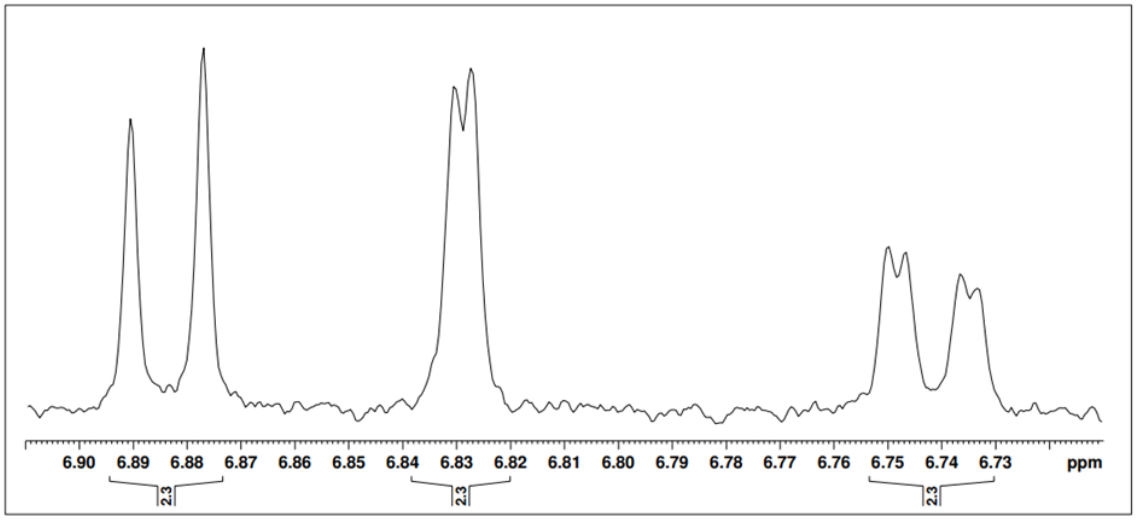

Figure A35. Spectrum of the control sample (control 3) at 47°C. ^1H NMR spectrum obtained from a sample containing 0.25 mM dopamine and 2.5 mM hexanal (homogenized at 47°C for 1 h), in 50 mM HEPES buffer, pH 7.4 with 5 mM ascorbic acid, 10% DMSO, 10% v/v D_2O and dss 139 µM.

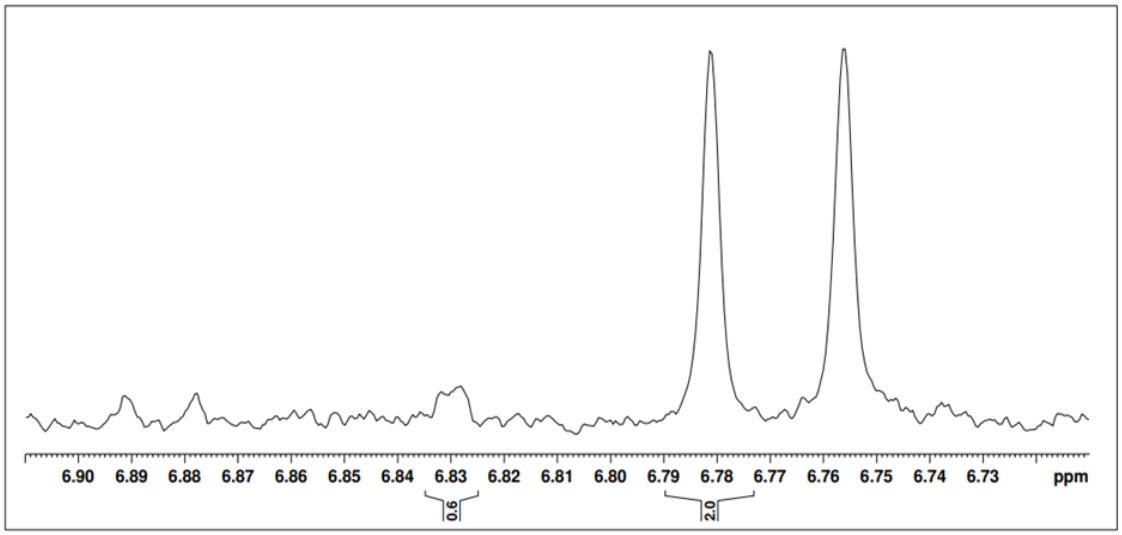

Figure A36. Spectrum of the non-immobilized Δ19*Tf*NCS catalyzed reaction (NCS 1) at 47°C. ^{1}H NMR spectrum obtained from a reaction sample between 0.25 mM dopamine and 2.5 mM hexanal catalyzed by non-immobilized Δ19*Tf*NCS at 47°C, in 50 mM HEPES buffer, pH 7.4 with 5 mM ascorbic acid, 10% DMSO, 10% v/v D_2O and dss 139 µM.

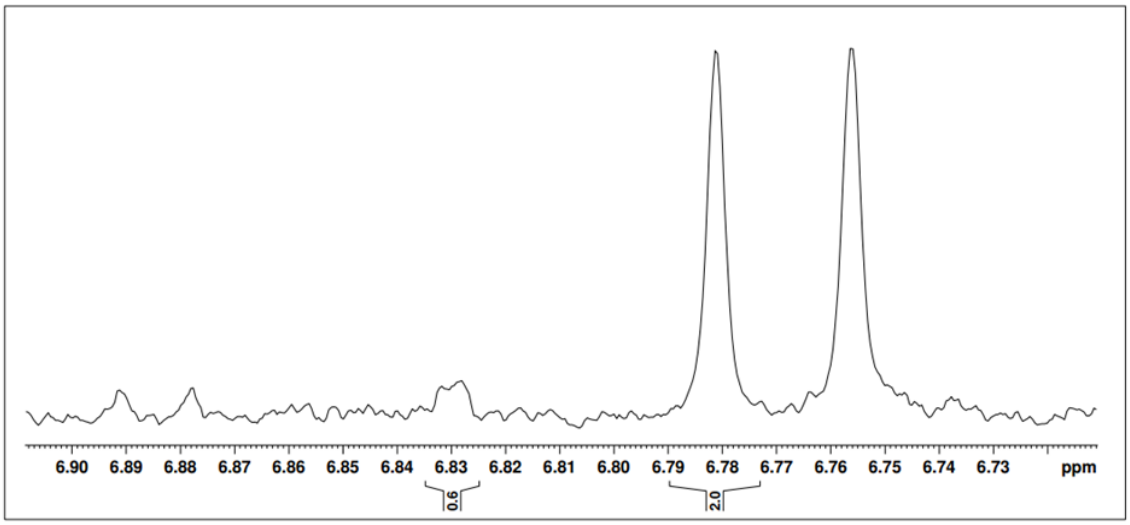

Figure A37. Spectrum of the non-immobilized Δ19*Tf*NCS catalyzed reaction (NCS 2) at 47°C. ^{1}H NMR spectrum obtained from a reaction sample between 0.25 mM dopamine and 2.5 mM hexanal catalyzed by non-immobilized Δ19*Tf*NCS at 47°C, in 50 mM HEPES buffer, pH 7.4 with 5 mM ascorbic acid, 10% DMSO, 10% v/v D_2O and dss 139 uM.

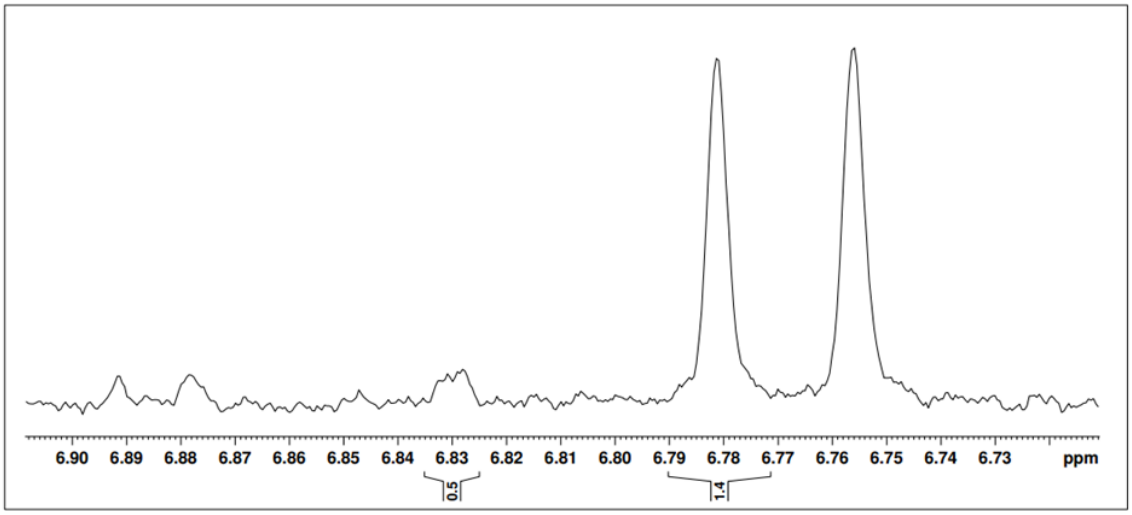

Figure A38. Spectrum of the non-immobilized Δ19*Tf*NCS catalyzed reaction (NCS 3) at 47°C. ^{1}H NMR spectrum obtained from a reaction sample between 0.25 mM dopamine and 2.5 mM hexanal catalyzed by non-immobilized Δ19*Tf*NCS at 47°C, in 50 mM HEPES buffer, pH 7.4 with 5 mM ascorbic acid, 10% DMSO, 10% v/v D_2O and dss 139 uM.

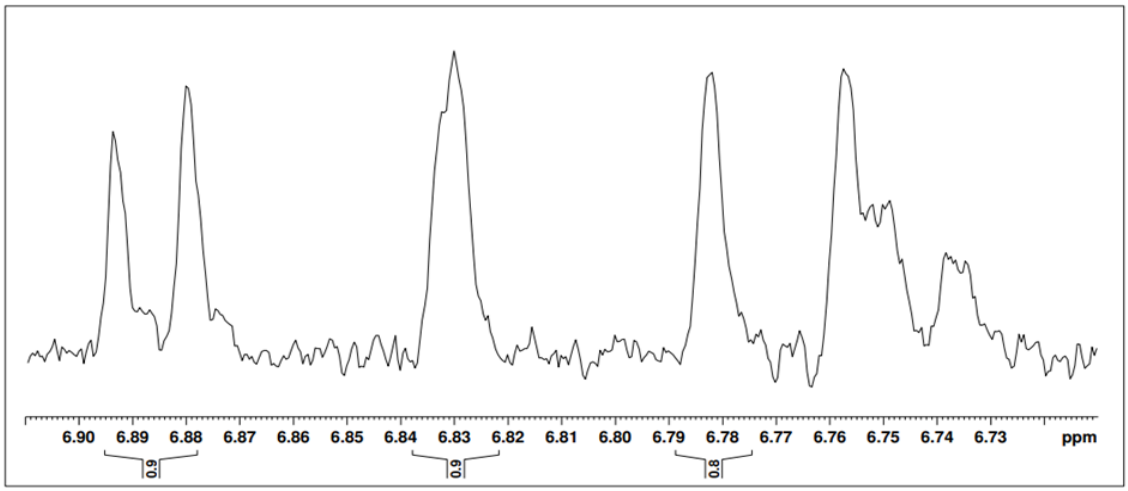

Figure A39. Spectrum of Δ19*Tf*NCS immobilized in kaolin catalyzed reaction sample (Kaolin 1) at 47°C. ^{1}H NMR spectrum obtained from a reaction sample between 0.25 mM dopamine and 2.5 mM hexanal catalyzed by Δ19*Tf*NCS immobilized in kaolin at 47°C, in 50 mM HEPES buffer, pH 7.4 with 5 mM ascorbic acid, 10% DMSO, 10% v/v D_2O and dss 139 uM.

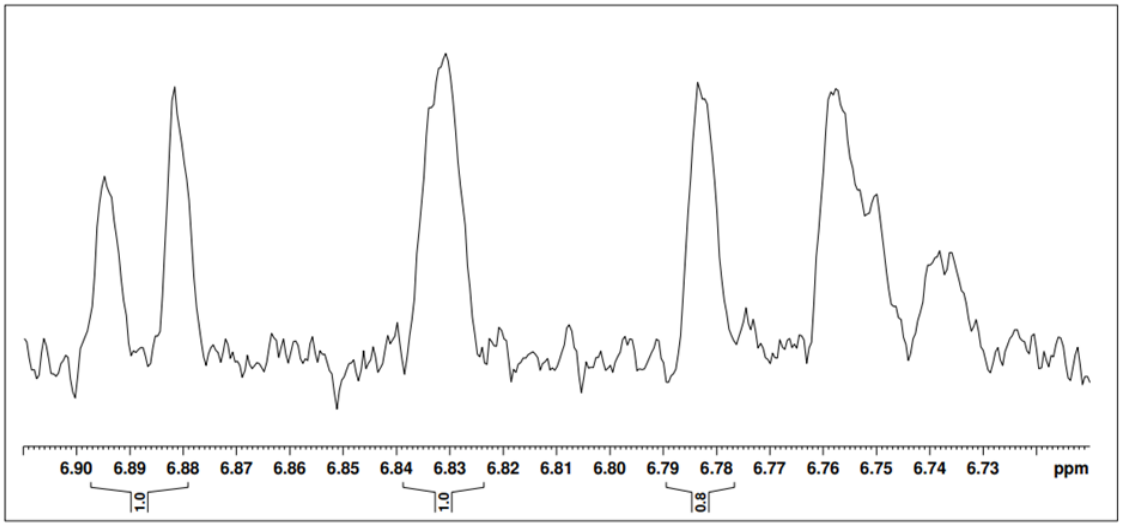

Figure A40. Spectrum of Δ19*Tf*NCS immobilized in kaolin catalyzed reaction sample (Kaolin 2) at 47°C. ^{1}H NMR spectrum obtained from a reaction sample between 0.25 mM dopamine and 2.5 mM hexanal catalyzed by Δ19*Tf*NCS immobilized in kaolin at 47°C, in 50 mM HEPES buffer, pH 7.4 with 5 mM ascorbic acid, 10% DMSO, 10% v/v D_2O and dss 139 uM.

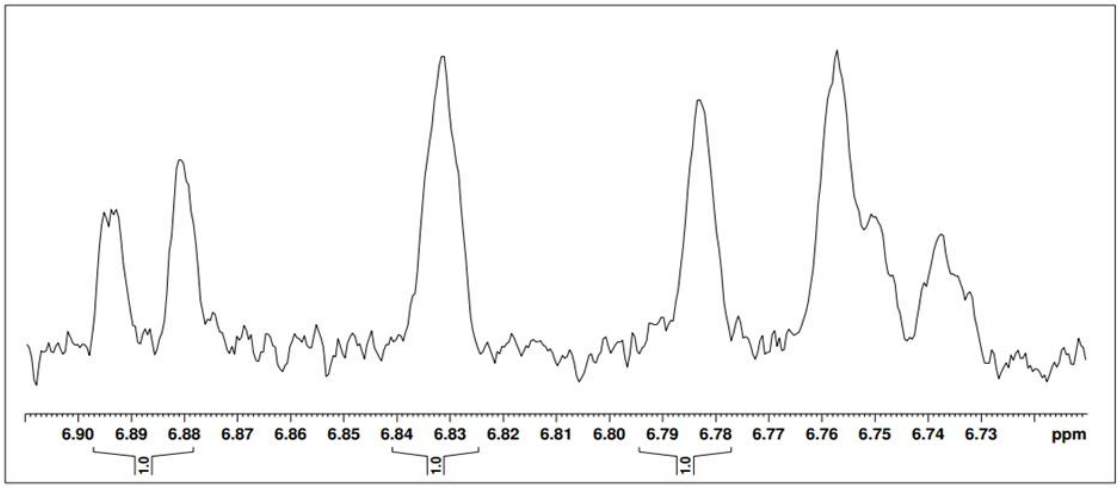

Figure A41. Spectrum of Δ19*Tf*NCS immobilized in kaolin catalyzed reaction sample (Kaolin 3) at 47°C. ^{1}H NMR spectrum obtained from a reaction sample between 0.25 mM dopamine and 2.5 mM hexanal catalyzed by Δ19*Tf*NCS immobilized in kaolin at 47°C, in 50 mM HEPES buffer, pH 7.4 with 5 mM ascorbic acid, 10% DMSO, 10% v/v D_2O and dss 139 uM.

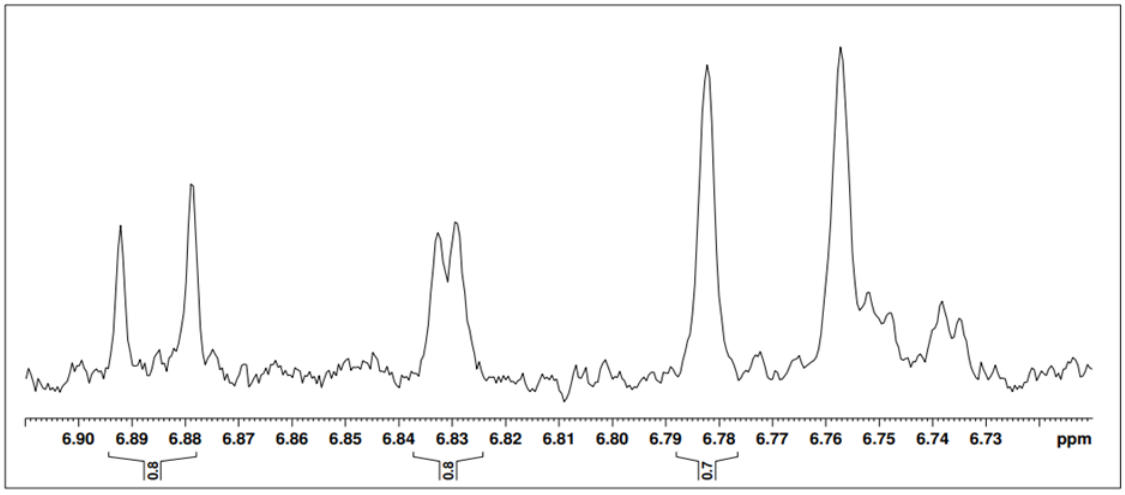

Figure A42. Spectrum of Δ19*Tf*NCS immobilized in celite 545 catalyzed reaction sample (Celite 1) at 47°C. ^{1}H NMR spectrum obtained from a reaction sample between 0.25 mM dopamine and 2.5 mM hexanal catalyzed by Δ19*Tf*NCS immobilized in celite 545 at 47°C, in 50 mM HEPES buffer, pH 7.4 with 5 mM ascorbic acid, 10% DMSO, 10% v/v D_2O and dss 139 uM.

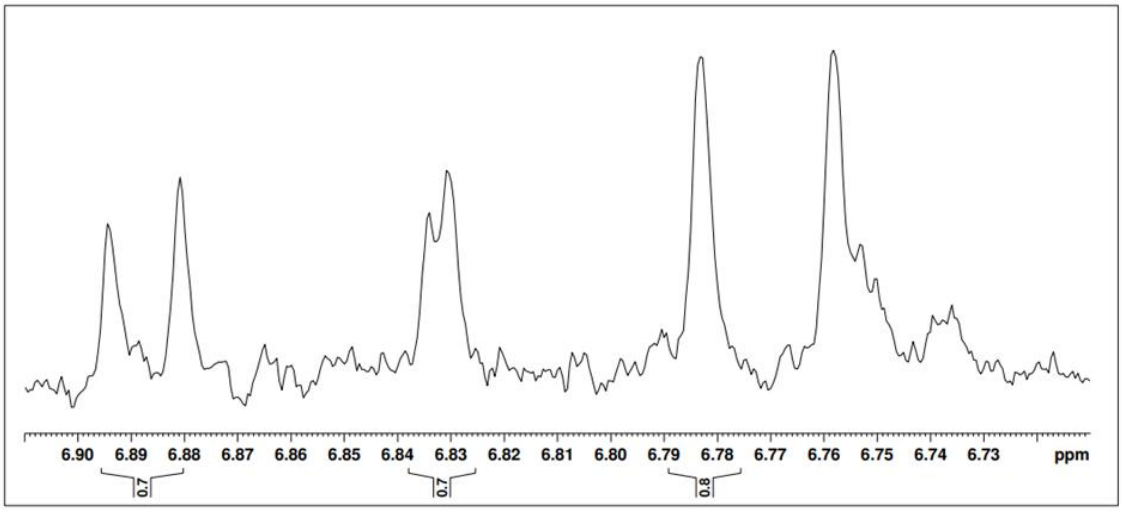

Figure A43. Spectrum of Δ19*Tf*NCS immobilized in celite 545 catalyzed reaction sample (Celite 2) at 47°C. ^{1}H NMR spectrum obtained from a reaction sample between 0.25 mM dopamine and 2.5 mM hexanal catalyzed by Δ19*Tf*NCS immobilized in celite 545 at 47°C, in 50 mM HEPES buffer, pH 7.4 with 5 mM ascorbic acid, 10% DMSO, 10% v/v D_2O and dss 139 uM.

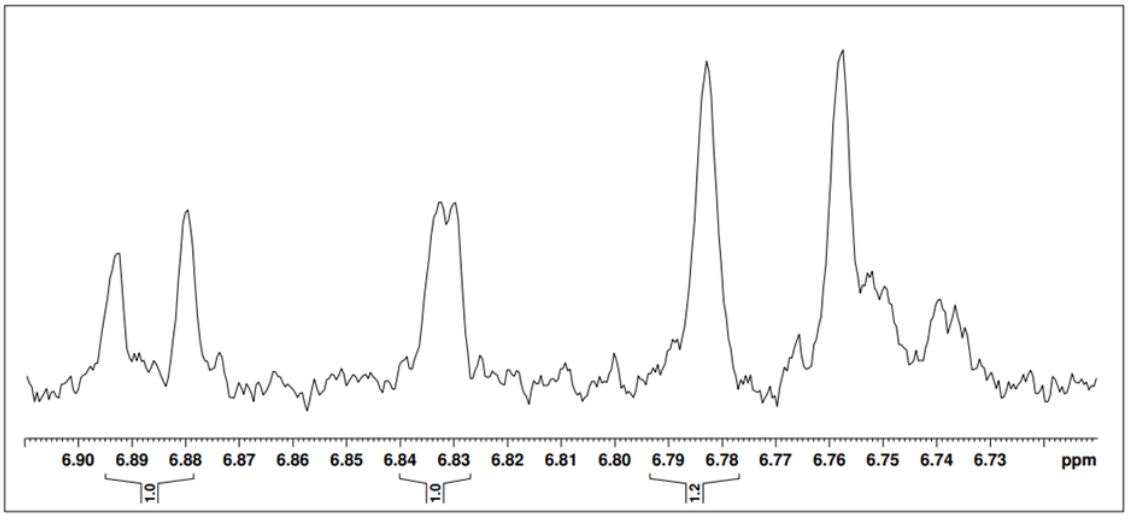

Figure A44. Spectrum of Δ19*Tf*NCS immobilized in celite 545 catalyzed reaction sample (Celite 3) at 47°C. ^{1}H NMR spectrum obtained from a reaction sample between 0.25 mM dopamine and 2.5 mM hexanal catalyzed by Δ19*Tf*NCS immobilized in celite 545 at 47°C, in 50 mM HEPES buffer, pH 7.4 with 5 mM ascorbic acid, 10% DMSO, 10% v/v D_2O and dss 139 uM.

Reactions at 57°C

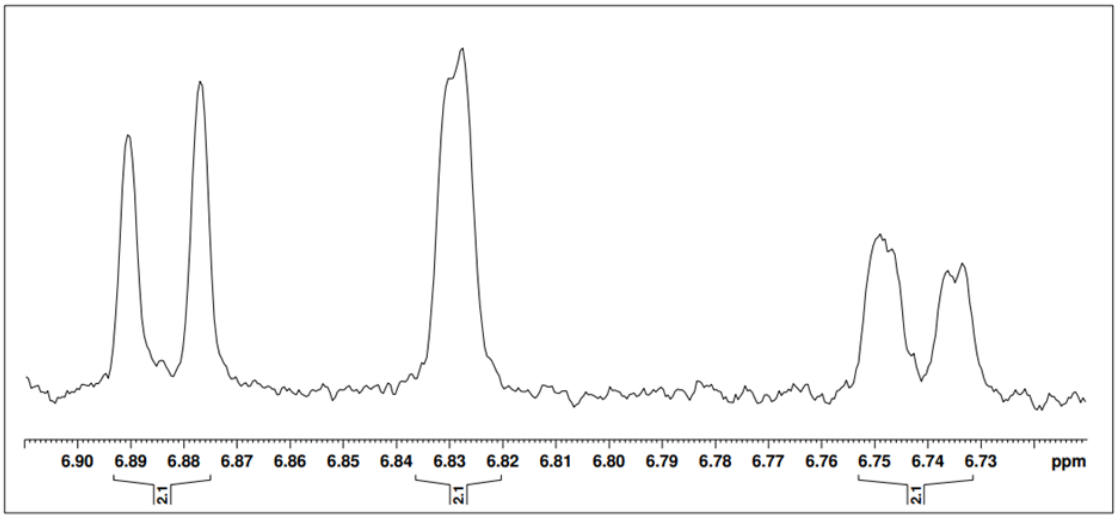

Figure A45. Spectrum of the control sample (control 1) at 57°C. ^{1}H NMR spectrum obtained from a sample containing 0.25 mM dopamine and 2.5 mM hexanal (homogenized at 57°C for

1 h), in 50 mM HEPES buffer, pH 7.4 with 5 mM ascorbic acid, 10% DMSO, 10% v/v D_2O and dss 139 uM. The spectrum was acquired at 298.1 K on a Bruker NanoBay 600 MHz spectrometer.

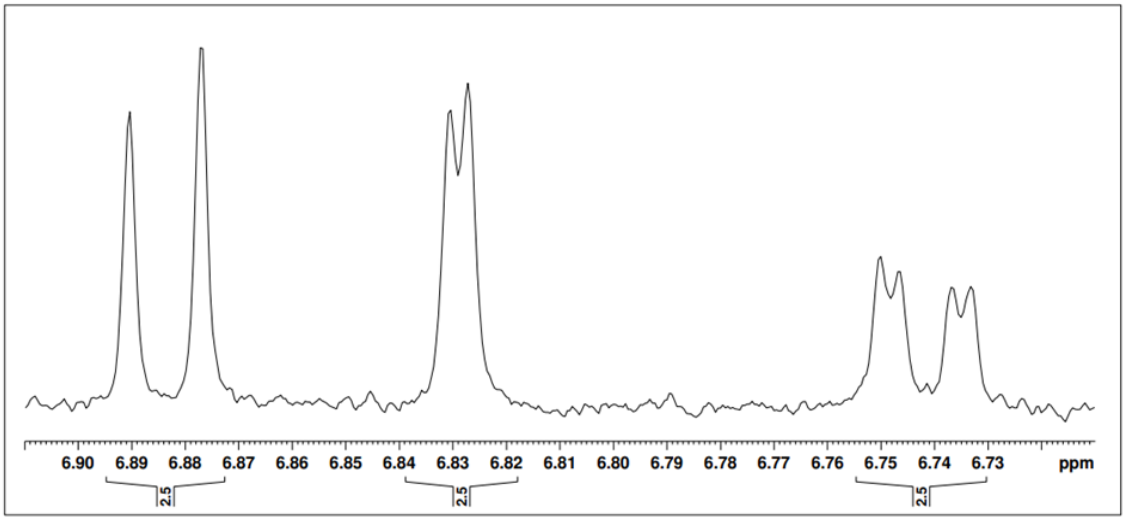

Figure A46. Spectrum of the control sample (control 2) at 57°C. ^1H NMR spectrum obtained from a sample containing 0.25 mM dopamine and 2.5 mM hexanal (homogenized at 57°C for 1 h), in 50 mM HEPES buffer, pH 7.4 with 5 mM ascorbic acid, 10% DMSO, 10% v/v D_2O and dss 139 uM.

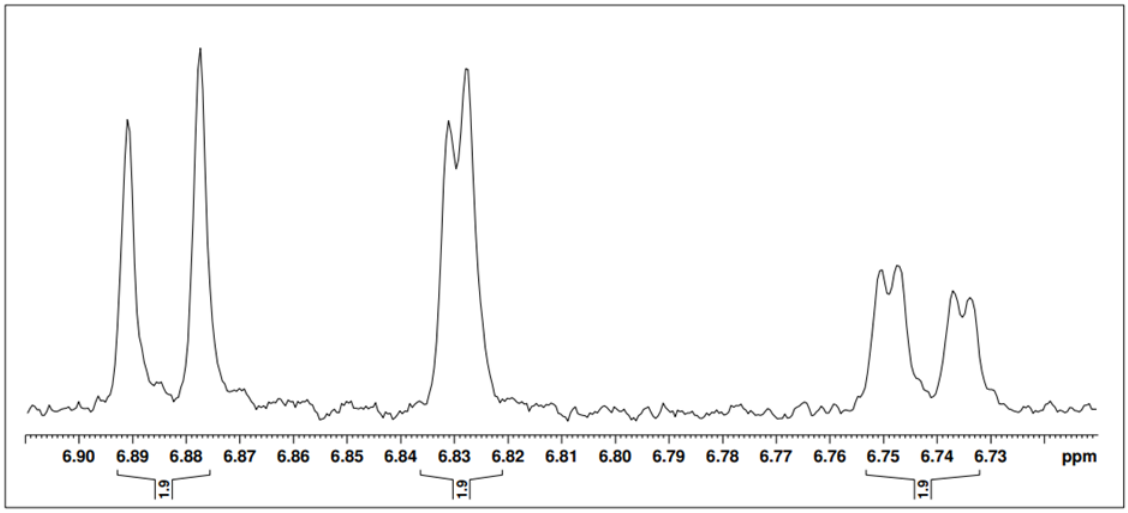

Figure A47. Spectrum of the control sample (control 3) at 57°C. ^1H NMR spectrum obtained from a sample containing 0.25 mM dopamine and 2.5 mM hexanal (homogenized at 57°C for 1 h), in 50 mM HEPES buffer, pH 7.4 with 5 mM ascorbic acid, 10% DMSO, 10% v/v D_2O and dss 139 uM.

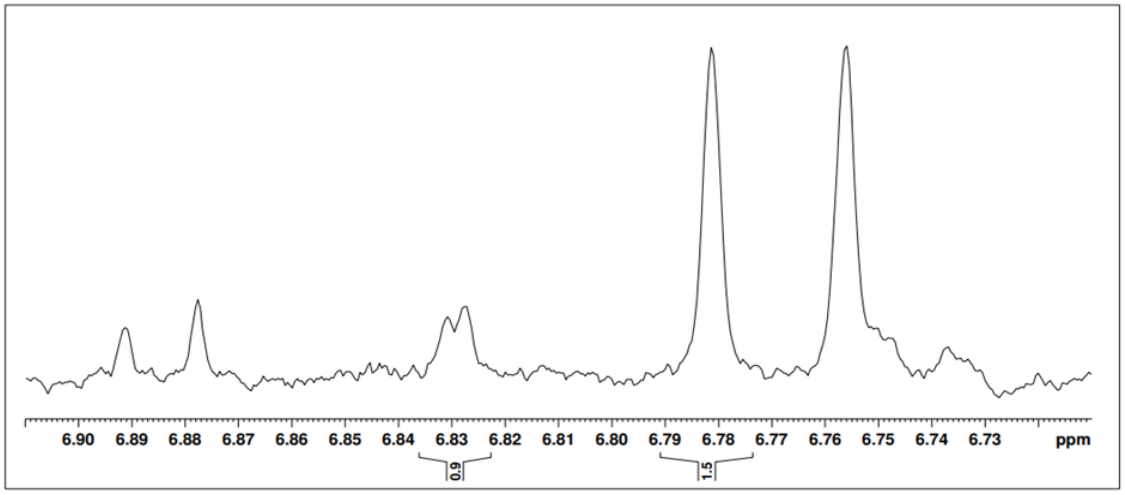

Figure A48. Spectrum of the non-immobilized Δ19*Tf*NCS catalyzed reaction (NCS 1) at 57°C. ^{1}H NMR spectrum obtained from a reaction sample between 0.25 mM dopamine and 2.5 mM hexanal catalyzed by non-immobilized Δ19*Tf*NCS at 57°C, in 50 mM HEPES buffer, pH 7.4 with 5 mM ascorbic acid, 10% DMSO, 10% v/v D_2O and dss 139 uM.

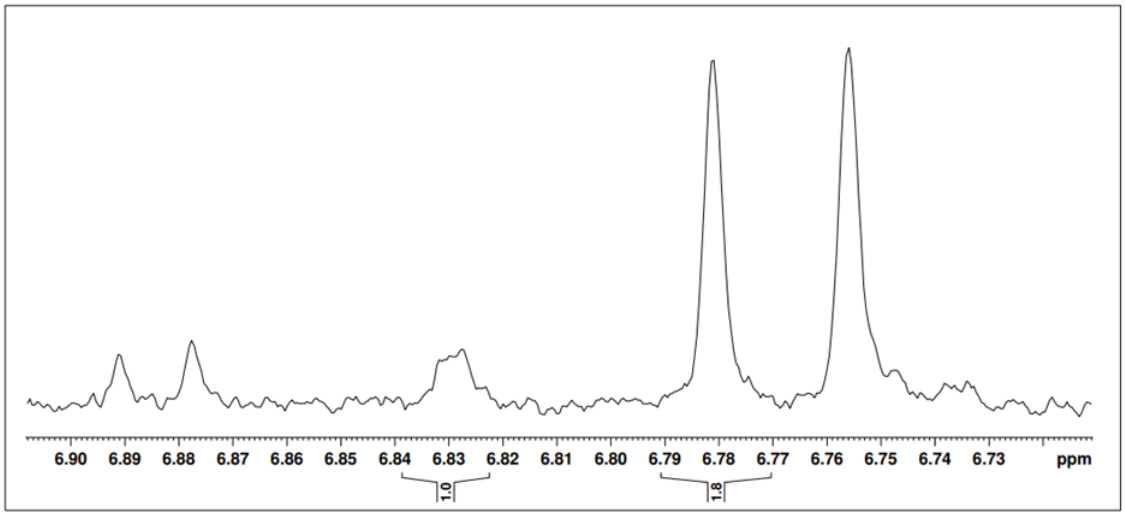

Figure A49. Spectrum of the non-immobilized Δ19*Tf*NCS catalyzed reaction (NCS 2) at 57°C. ^{1}H NMR spectrum obtained from a reaction sample between 0.25 mM dopamine and 2.5 mM hexanal catalyzed by non-immobilized Δ19*Tf*NCS at 57°C, in 50 mM HEPES buffer, pH 7.4 with 5 mM ascorbic acid, 10% DMSO, 10% v/v D_2O and dss 139 uM.

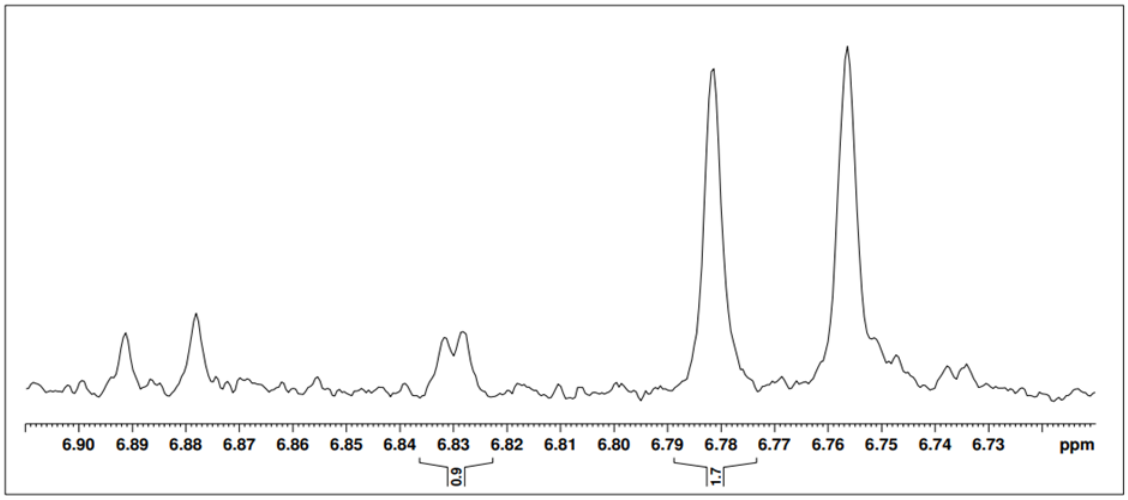

Figure A50. Spectrum of the non-immobilized Δ19*Tf*NCS catalyzed reaction (NCS 3) at 57°C. ^{1}H NMR spectrum obtained from a reaction sample between 0.25 mM dopamine and 2.5 mM hexanal catalyzed by non-immobilized Δ19*Tf*NCS at 57°C, in 50 mM HEPES buffer, pH 7.4 with 5 mM ascorbic acid, 10% DMSO, 10% v/v D_2O and dss 139 uM.

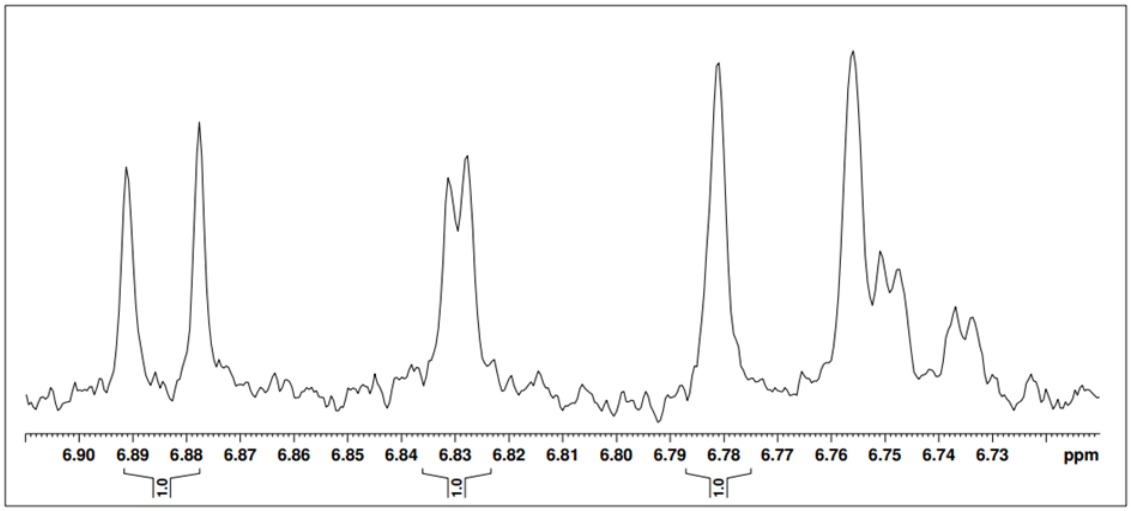

Figure A51. Spectrum of Δ19*Tf*NCS immobilized in kaolin catalyzed reaction sample (Kaolin 1) at 57°C. ^{1}H NMR spectrum obtained from a reaction sample between 0.25 mM dopamine and 2.5 mM hexanal catalyzed by Δ19*Tf*NCS immobilized in kaolin at 57°C, in 50 mM HEPES buffer, pH 7.4 with 5 mM ascorbic acid, 10% DMSO, 10% v/v D_2O and dss 139 uM.

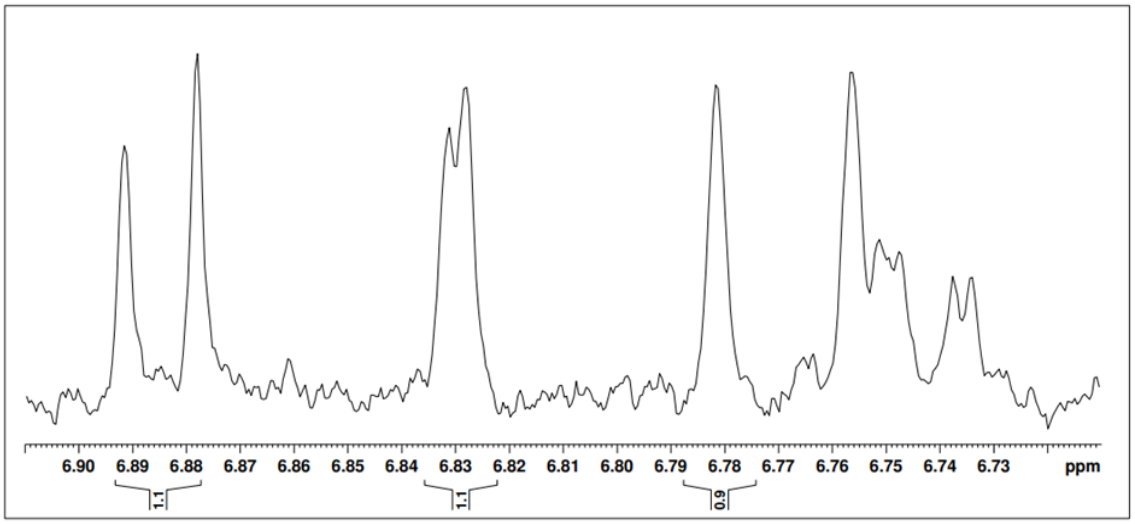

Figure A52. Spectrum of Δ19*Tf*NCS immobilized in kaolin catalyzed reaction sample (Kaolin 2) at 57°C. ^{1}H NMR spectrum obtained from a reaction sample between 0.25 mM dopamine and 2.5 mM hexanal catalyzed by Δ19*Tf*NCS immobilized in kaolin at 57°C, in 50 mM HEPES buffer, pH 7.4 with 5 mM ascorbic acid, 10% DMSO, 10% v/v D_2O and dss 139 uM.

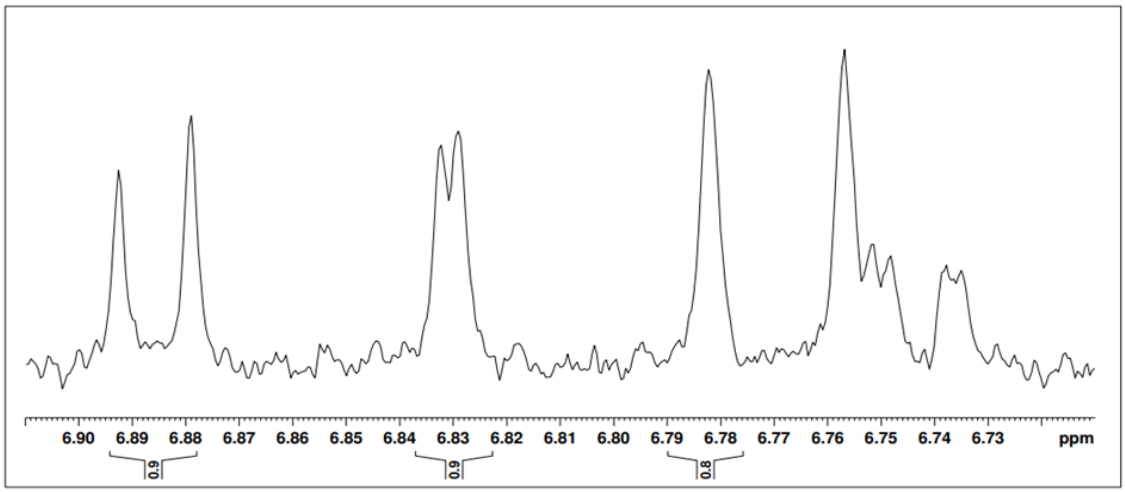

Figure A53. Spectrum of Δ19*Tf*NCS immobilized in kaolin catalyzed reaction sample (Kaolin 3) at 57°C. ^{1}H NMR spectrum obtained from a reaction sample between 0.25 mM dopamine and 2.5 mM hexanal catalyzed by Δ19*Tf*NCS immobilized in kaolin at 57°C, in 50 mM HEPES buffer, pH 7.4 with 5 mM ascorbic acid, 10% DMSO, 10% v/v D_2O and dss 139 uM.

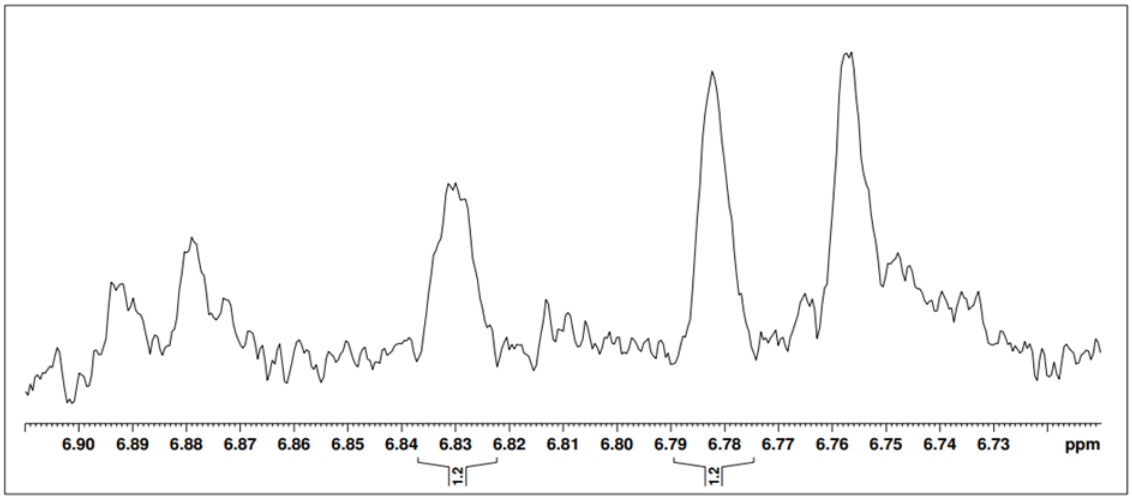

Figure A54. Spectrum of Δ19*Tf*NCS immobilized in celite 545 catalyzed reaction sample (Celite 1) at 57°C. ^{1}H NMR spectrum obtained from a reaction sample between 0.25 mM dopamine and 2.5 mM hexanal catalyzed by Δ19*Tf*NCS immobilized in celite 545 at 57°C, in 50 mM HEPES buffer, pH 7.4 with 5 mM ascorbic acid, 10% DMSO, 10% v/v D_2O and dss 139 uM.

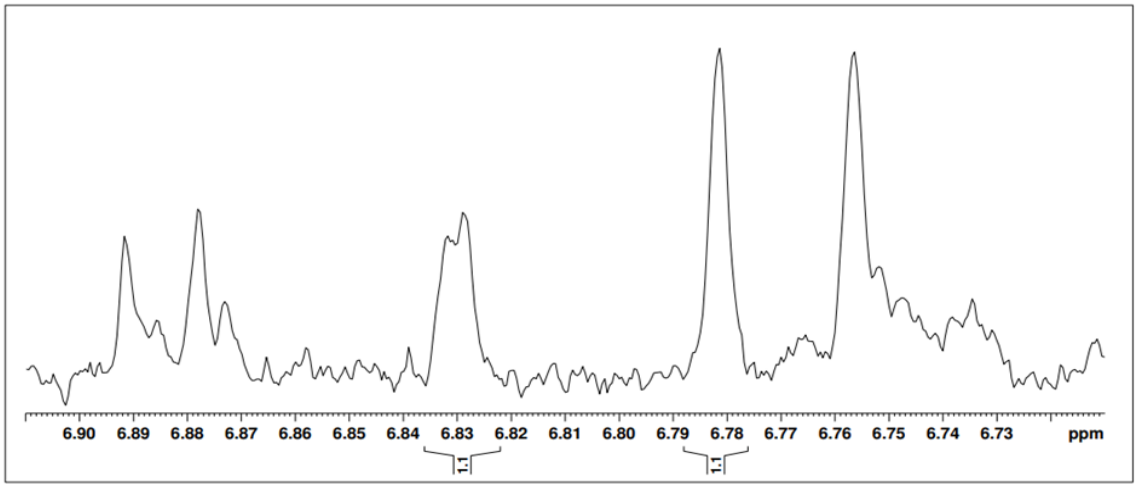

Figure A55. Spectrum of Δ19*Tf*NCS immobilized in celite 545 catalyzed reaction sample (Celite 2) at 57°C. ^{1}H NMR spectrum obtained from a reaction sample between 0.25 mM dopamine and 2.5 mM hexanal catalyzed by Δ19*Tf*NCS immobilized in celite 545 at 57°C, in 50 mM HEPES buffer, pH 7.4 with 5 mM ascorbic acid, 10% DMSO, 10% v/v D_2O and dss 139 uM.

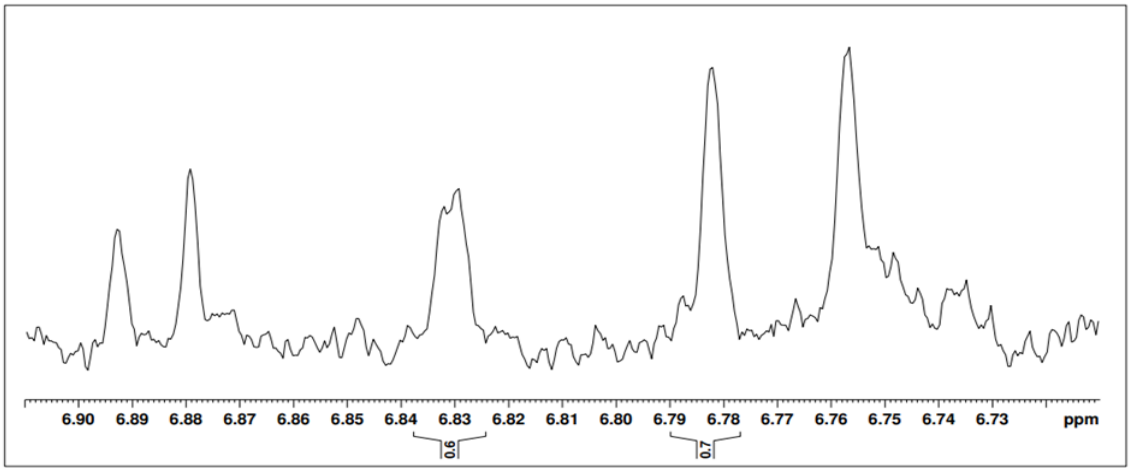

Figure A56. Spectrum of Δ19*Tf*NCS immobilized in celite 545 catalyzed reaction sample (Celite 3) at 57°C. ^{1}H NMR spectrum obtained from a reaction sample between 0.25 mM dopamine and 2.5 mM hexanal catalyzed by Δ19*Tf*NCS immobilized in celite 545 at 57°C, in 50 mM HEPES buffer, pH 7.4 with 5 mM ascorbic acid, 10% DMSO, 10% v/v D_2O and dss 139 uM.

Reactions at 20% v/v DMSO

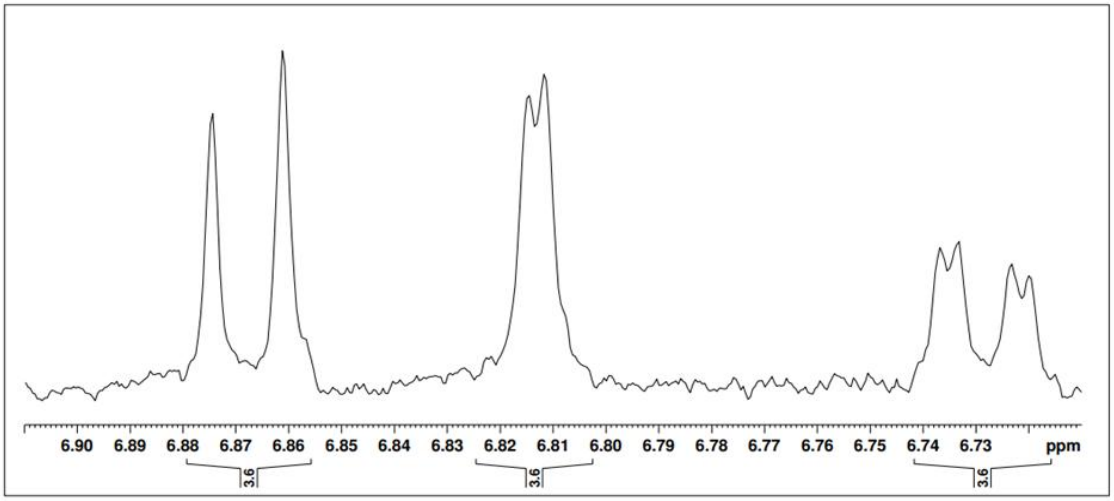

Figure A57. Spectrum of the control sample (control 1) at 20% v/v DMSO. ^{1}H NMR spectrum obtained from a sample containing 0.25 mM dopamine and 2.5 mM hexanal (homogenized at

37°C for 1 h), in 50 mM HEPES buffer, pH 7.4 with 5 mM ascorbic acid, 20% DMSO, 10% v/v D_2O and dss 139 uM.

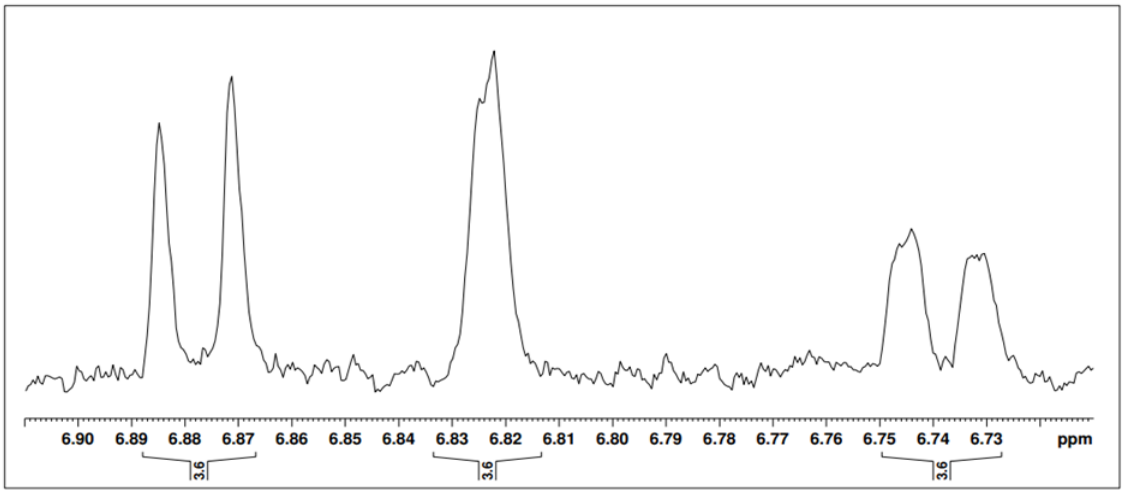

Figure A58. Spectrum of the control sample (control 2) at 20% v/v DMSO. ^1H NMR spectrum obtained from a sample containing 0.25 mM dopamine and 2.5 mM hexanal (homogenized at 37°C for 1 h), in 50 mM HEPES buffer, pH 7.4 with 5 mM ascorbic acid, 20% DMSO, 10% v/v D_2O and dss 139 uM.

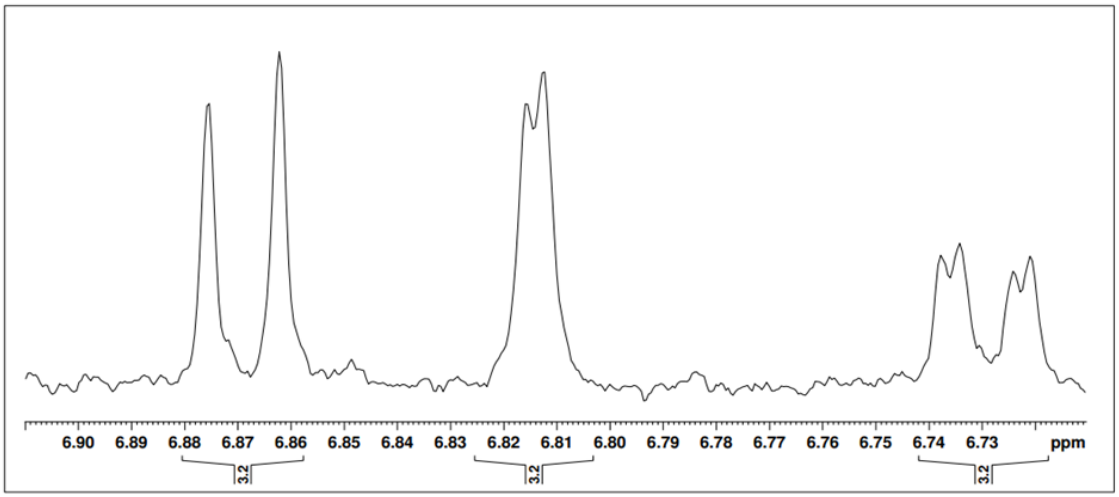

Figure A59. Spectrum of the control sample (control 3) at 20% v/v DMSO. ^1H NMR spectrum obtained from a sample containing 0.25 mM dopamine and 2.5 mM hexanal (homogenized at 37°C for 1 h), in 50 mM HEPES buffer, pH 7.4 with 5 mM ascorbic acid, 20% DMSO, 10% v/v D_2O and dss 139 uM.

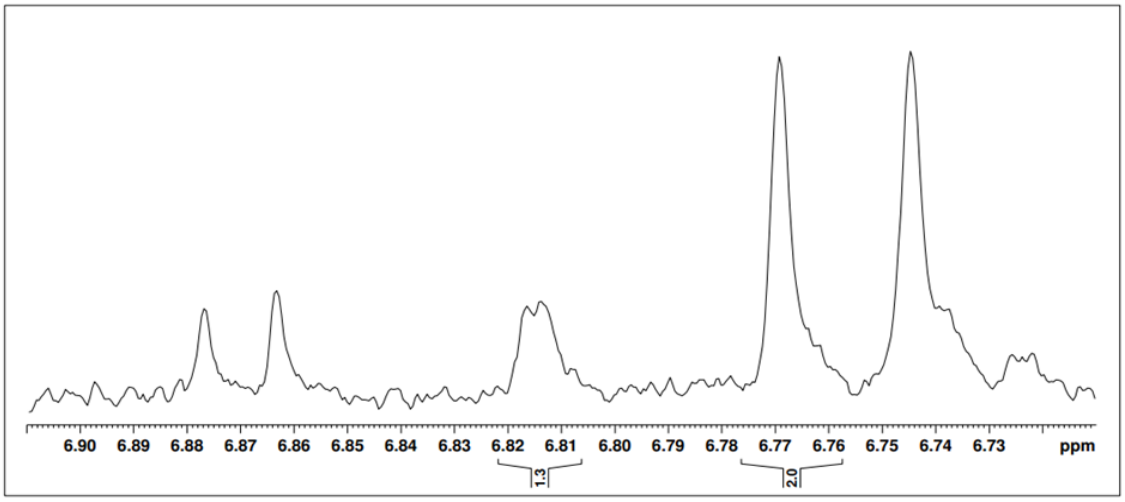

Figure A60. Spectrum of the non-immobilized Δ19*Tf*NCS catalyzed reaction (NCS 1) at 20% v/v DMSO. ^{1}H NMR spectrum obtained from a reaction sample between 0.25 mM dopamine and 2.5 mM hexanal catalyzed by non-immobilized Δ19*Tf*NCS at 37°C, in 50 mM HEPES buffer, pH 7.4 with 5 mM ascorbic acid, 20% DMSO, 10% v/v D_2O and dss 139 uM.

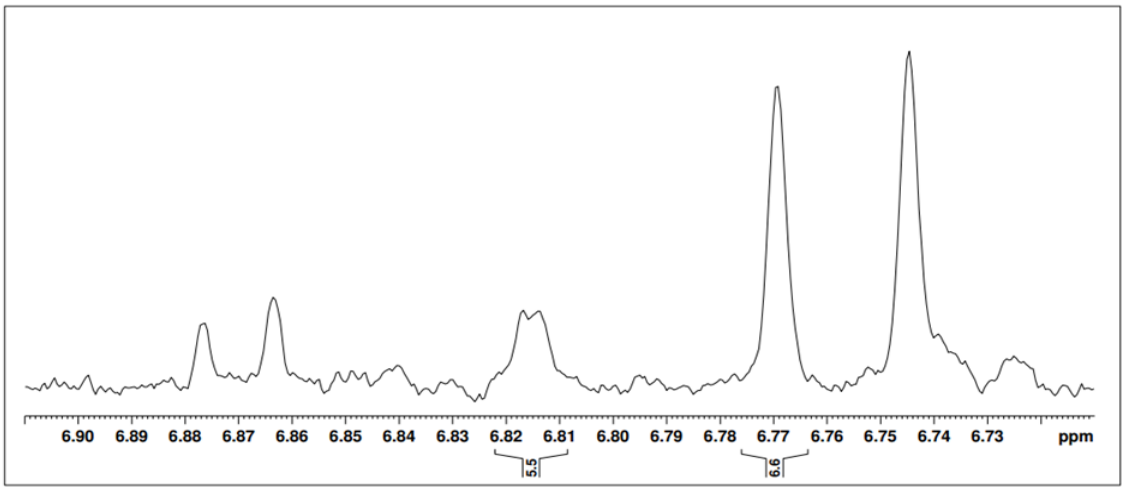

Figure A61. Spectrum of the non-immobilized Δ19*Tf*NCS catalyzed reaction (NCS 2) at 20% v/v DMSO. ^{1}H NMR spectrum obtained from a reaction sample between 0.25 mM dopamine and 2.5 mM hexanal catalyzed by non-immobilized Δ19*Tf*NCS at 37°C, in 50 mM HEPES buffer, pH 7.4 with 5 mM ascorbic acid, 20% DMSO, 10% v/v D_2O and dss 139 uM.

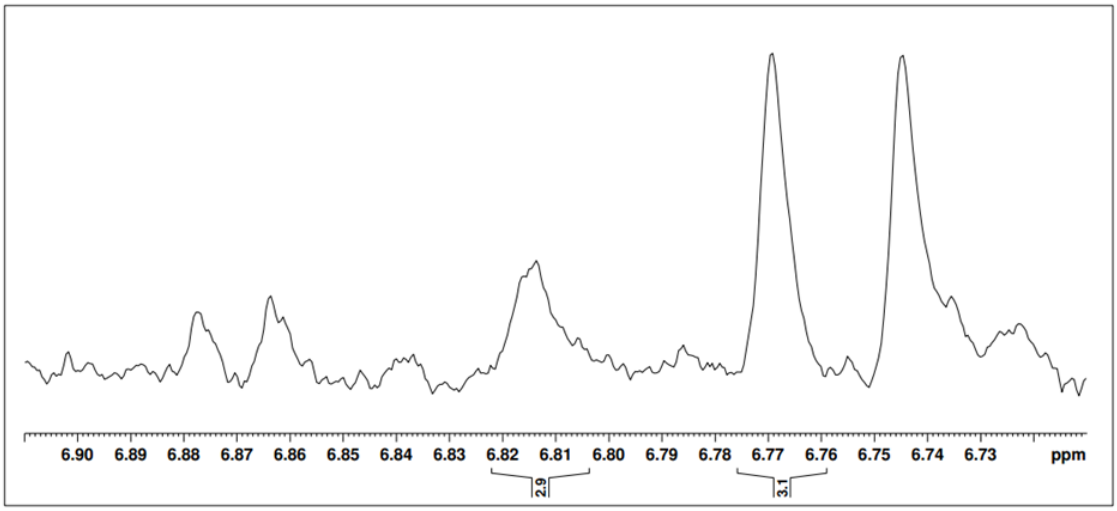

Figure A62. Spectrum of the non-immobilized Δ19*Tf*NCS catalyzed reaction (NCS 3) at 20% v/v DMSO. ^{1}H NMR spectrum obtained from a reaction sample between 0.25 mM dopamine and 2.5 mM hexanal catalyzed by non-immobilized Δ19*Tf*NCS at 37°C, in 50 mM HEPES buffer, pH 7.4 with 5 mM ascorbic acid, 20% DMSO, 10% v/v D_2O and dss 139 uM.

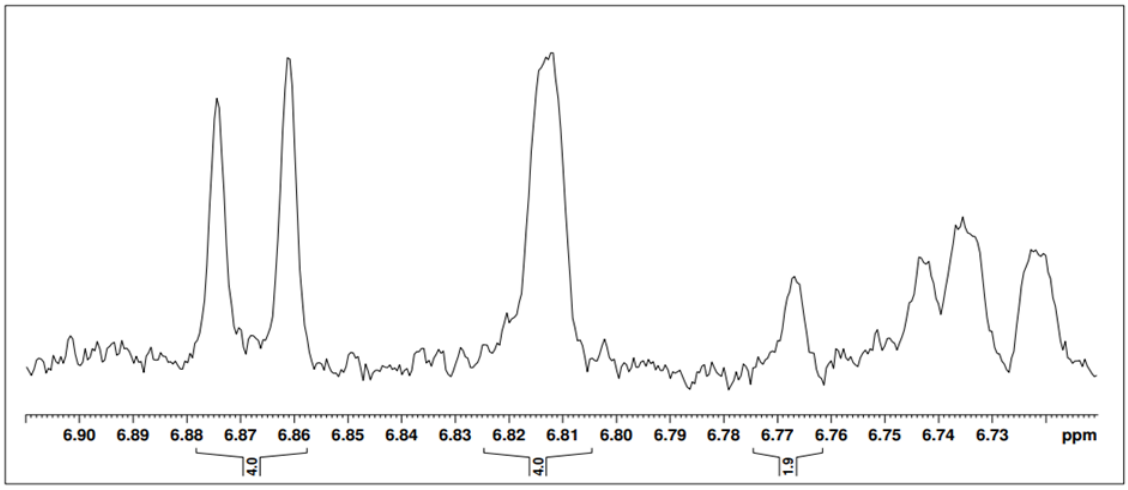

Figure A63. Spectrum of Δ19*Tf*NCS immobilized in kaolin catalyzed reaction sample (Kaolin 1) at 20% v/v DMSO. ^{1}H NMR spectrum obtained from a reaction sample between 0.25 mM dopamine and 2.5 mM hexanal catalyzed by Δ19*Tf*NCS immobilized in kaolin at 37°C, in 50 mM HEPES buffer, pH 7.4 with 5 mM ascorbic acid, 20% DMSO, 10% v/v D_2O and dss 139 uM.

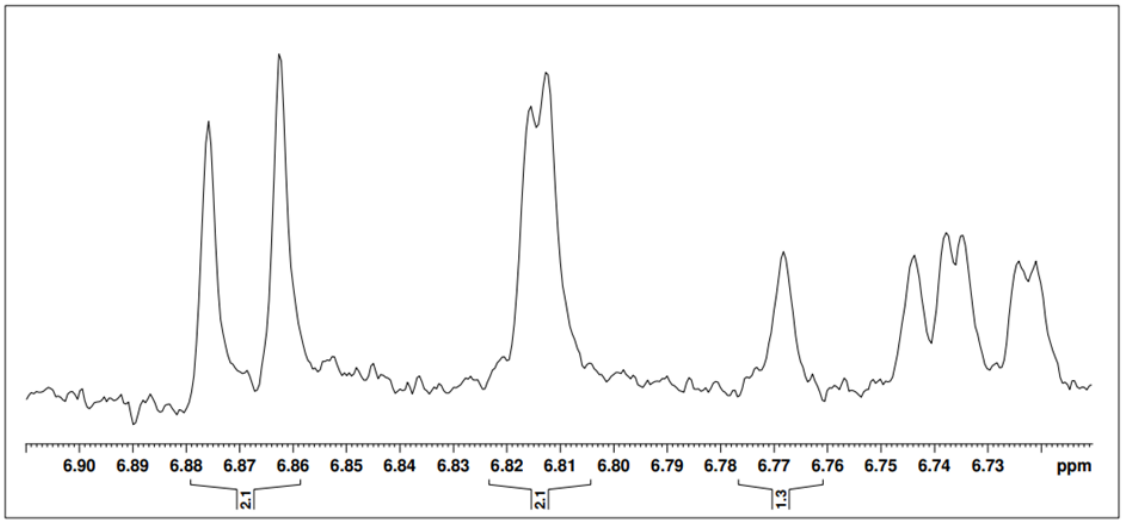

Figure A64. Spectrum of Δ19*Tf*NCS immobilized in kaolin catalyzed reaction sample (Kaolin 2) at 20% v/v DMSO. ^{1}H NMR spectrum obtained from a reaction sample between 0.25 mM dopamine and 2.5 mM hexanal catalyzed by Δ19*Tf*NCS immobilized in kaolin at 37°C, in 50 mM HEPES buffer, pH 7.4 with 5 mM ascorbic acid, 20% DMSO, 10% v/v D_2O and dss 139 uM.

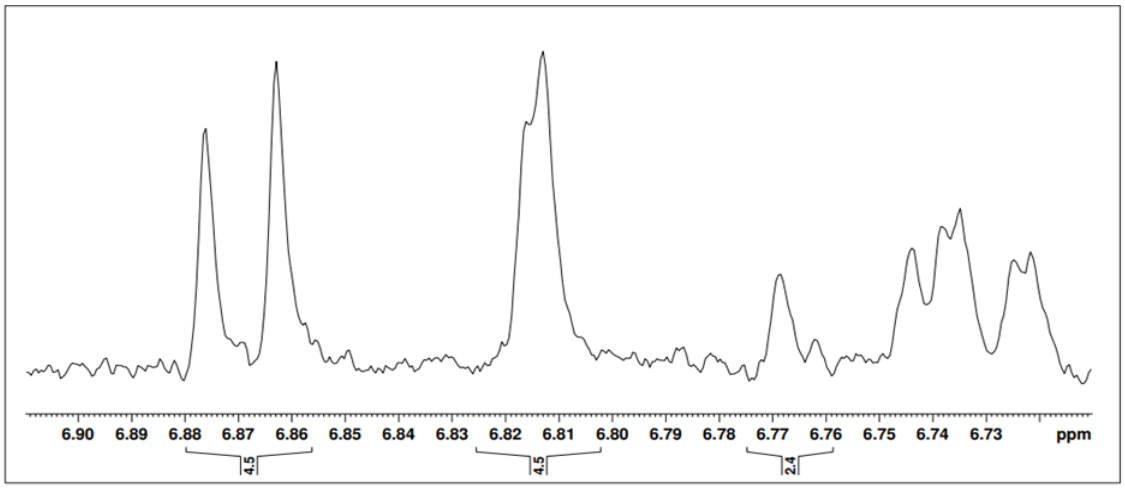

Figure A65. Spectrum of Δ19*Tf*NCS immobilized in kaolin catalyzed reaction sample (Kaolin 3) at 20% v/v DMSO. ^{1}H NMR spectrum obtained from a reaction sample between 0.25 mM dopamine and 2.5 mM hexanal catalyzed by Δ19*Tf*NCS immobilized in kaolin at 37°C, in 50 mM HEPES buffer, pH 7.4 with 5 mM ascorbic acid, 20% DMSO, 10% v/v D_2O and dss 139 uM.

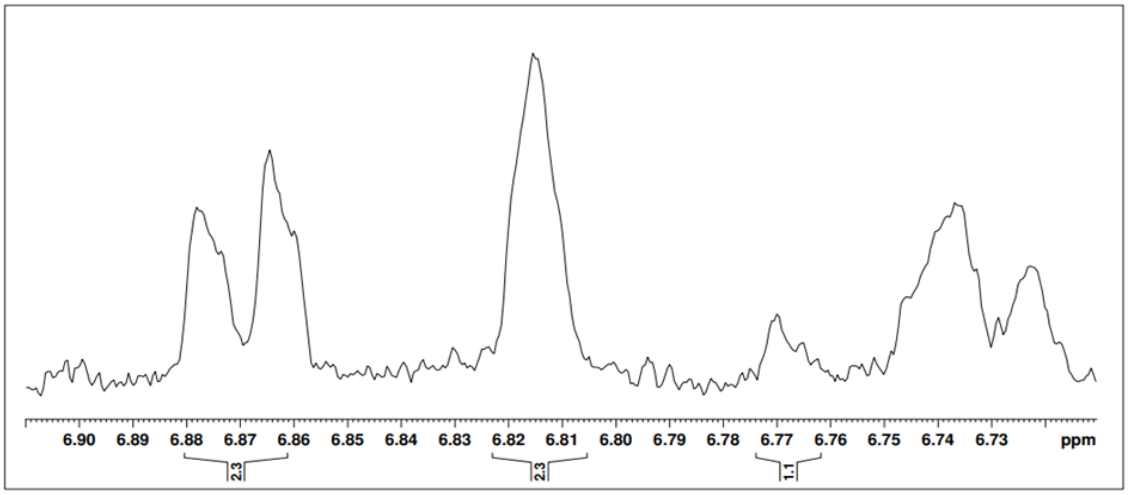

Figure A66. Spectrum of Δ19*Tf*NCS immobilized in celite 545 catalyzed reaction sample (Celite 1) at 20% v/v DMSO. ^{1}H NMR spectrum obtained from a reaction sample between 0.25 mM dopamine and 2.5 mM hexanal catalyzed by Δ19*Tf*NCS immobilized in celite 545 at 37°C, in 50 mM HEPES buffer, pH 7.4 with 5 mM ascorbic acid, 20% DMSO, 10% v/v D_2O and dss 139 uM.

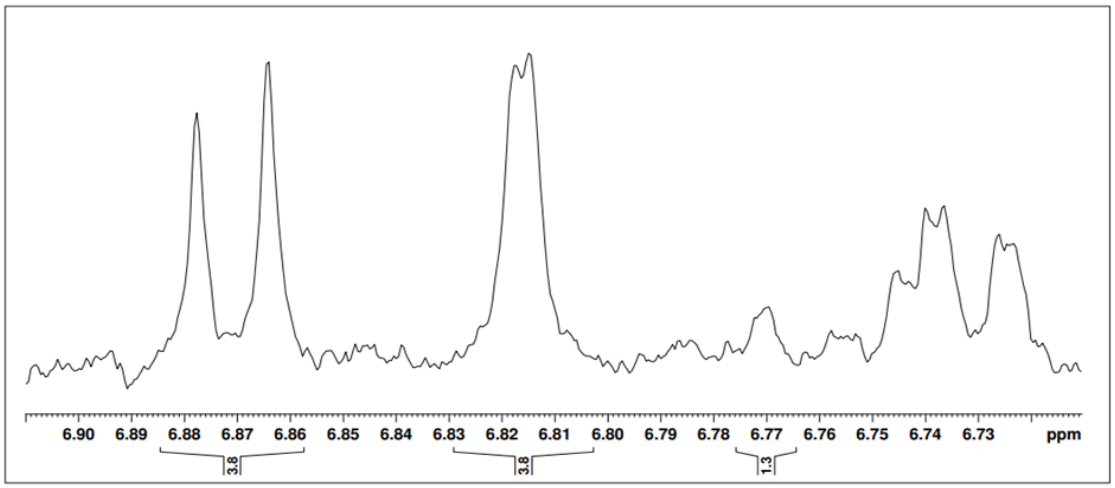

Figure A67. Spectrum of Δ19*Tf*NCS immobilized in celite 545 catalyzed reaction sample (Celite 2) at 20% v/v DMSO. ^{1}H NMR spectrum obtained from a reaction sample between 0.25 mM dopamine and 2.5 mM hexanal catalyzed by Δ19*Tf*NCS immobilized in celite 545 at 37°C, in 50 mM HEPES buffer, pH 7.4 with 5 mM ascorbic acid, 20% DMSO, 10% v/v D_2O and dss 139 uM.

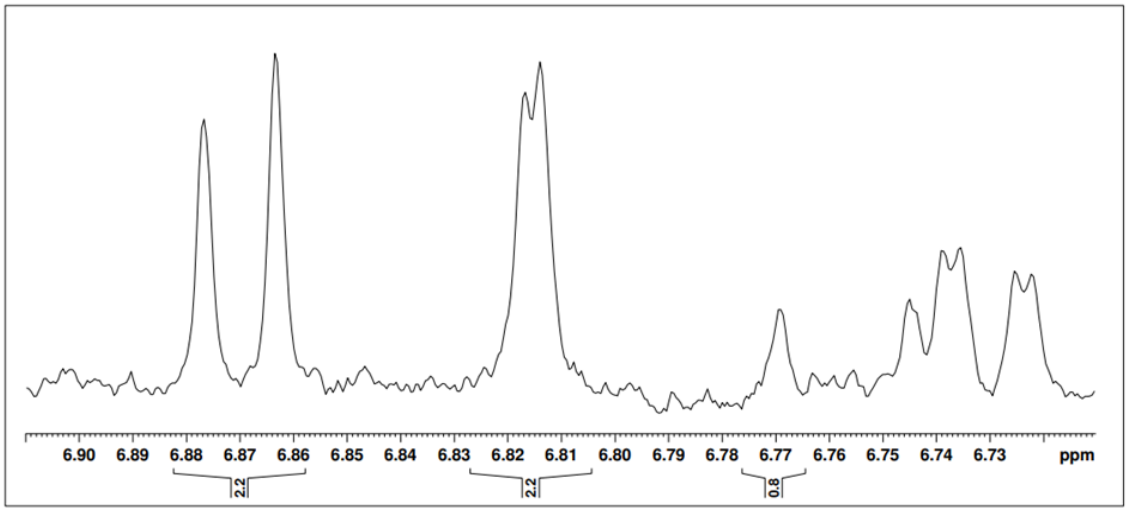

Figure A68. NMR Spectrum of Δ19*Tf*NCS immobilized in celite 545 catalyzed reaction sample (Celite 3) at 20% v/v DMSO. ^{1}H NMR spectrum obtained from a reaction sample between 0.25 mM dopamine and 2.5 mM hexanal catalyzed by Δ19*Tf*NCS immobilized in celite 545 at 37°C, in 50 mM HEPES buffer, pH 7.4 with 5 mM ascorbic acid, 20% DMSO, 10% v/v D_2O and dss 139 uM.

Reaction samples - Chiral HPLC chromatograms

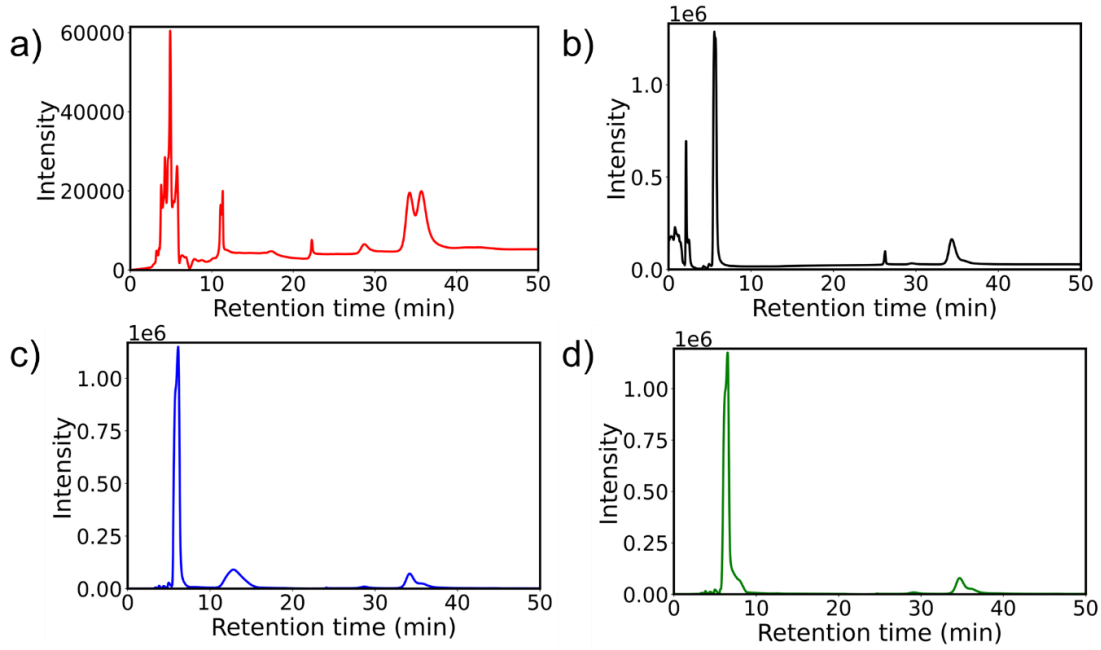

Figure A69. Full chiral HPLC chromatograms of Pictet-Spengler reaction products: (a) non-enzymatic control reaction; (b) reaction catalyzed by free Δ*19Tf*NCS; (c) reaction catalyzed by kaolin-immobilized Δ19TfNCS; (d) reaction catalyzed by Celite 545-immobilized Δ19*Tf*NCS.